Engineering quantum states and electronic landscapes through surface molecular nanoarchitectures

Ignacio Piquero-Zulaica*

Centro de Física de Materiales CSIC/UPV-EHU-Materials Physics Center, Manuel Lardizabal 5, E-20018 San Sebastián, Spain, Donostia International Physics Center, Paseo Manuel Lardizabal 4, E-20018 Donostia-San Sebastián, Spain, and Physics Department E20, Technical University of Munich, 85748 Garching, Germany

Jorge Lobo-Checa†

Instituto de Nanociencia y Materiales de Aragón (INMA), CSIC-Universidad de Zaragoza, Zaragoza 50009, Spain and Departamento de Física de la Materia Condensada, Universidad de Zaragoza, E-50009 Zaragoza, Spain

Zakaria M. Abd El-Fattah

Physics Department, Faculty of Science, Al-Azhar University, Nasr City, E-11884 Cairo, Egypt

J. Enrique Ortega

Centro de Física de Materiales, CSIC/UPV-EHU-Materials Physics Center, Manuel Lardizabal 5, E-20018 San Sebastián, Spain, Donostia International Physics Center, Paseo Manuel Lardizabal 4, E-20018 Donostia-San Sebastián, Spain, and Departamento de Física Aplicada I, Universidad del País Vasco (UPV/EHU), E-20018 Donostia–San Sebastián, Spain

Florian Klappenberger, Willi Auwärter, and Johannes V. Barth‡

Physics Department E20, Technical University of Munich, 85748 Garching, Germany

(published 22 December 2022)

Surfaces are at the frontier of every known solid. They provide versatile supports for functional nanostructures and mediate essential physicochemical processes. Intimately related to two-dimensional materials, interfaces and atomically thin films often feature distinct electronic states with respect to the bulk, which is key to many relevant properties, such as catalytic activity, interfacial charge-transfer, and crystal growth mechanisms. To induce novel quantum properties via lateral scattering and confinement, reducing the surface electrons' dimensionality and spread with atomic precision is of particular interest. Both atomic manipulation and supramolecular principles provide access to custom-designed molecular assemblies and superlattices, which tailor the surface electronic landscape and influence fundamental chemical and physical properties at the nanoscale. Here the confinement of surface-state electrons is reviewed, with a focus on their interaction with molecular scaffolds created by molecular manipulation and self-assembly protocols under ultrahigh vacuum conditions. Starting with the quasifree two-dimensional electron gas present at the (111)-oriented surface planes of noble metals, the intriguing molecule-based structural complexity and versatility is illustrated. Surveyed are low-dimensional confining structures in the form of artificial lattices, molecular nanogratings, or quantum dot arrays, which are constructed upon an appropriate choice of their building constituents. Whenever the realized (metal-)organic networks exhibit long-range order, modified surface band structures with characteristic features emerge, inducing noteworthy physical phenomena such as discretization, quantum coupling or energy, and effective mass renormalization. Such collective electronic states can be additionally modified by positioning guest species at the voids of open nanoarchitectures. The designed scattering potential landscapes can be described with semiempirical models, bringing thus the prospect of total control over surface electron confinement and novel quantum states within reach.

DOI: 10.1103/RevModPhys.94.045008

*ipiquerozulaica@gmail.com
†jorge.lobo@csic.es
‡jvb@tum.de

CONTENTS

I. INTRODUCTION

Reaching atomistic control and understanding of matter has been a long-standing goal of humankind, receiving widespread attention once the foundations of atomic and molecular sciences were established. Enormous effort has been dedicated to developing fabrication, characterization, and manipulation procedures, providing access to novel expressions of materials, useful electronic, photonic, or magnetic properties, as well as collective atomic states with ever-increasing precision and complexity (Klitzing, Dorda, and Pepper, 1980; Shechtman *et al.*, 1984; Amano *et al.*, 1986; Heeger *et al.*, 1988; Binasch *et al.*, 1989; Davis *et al.*, 1995; Kane and Mele, 2005; Bloch, Dalibard, and Zwerger, 2008; Mühlbauer *et al.*, 2009). Multiple instrumental developments were crucial to providing direct insight into the nature and behavior of atomic and molecular species at the angstrom scale, whereby the imaging capabilities by electron microscopy, field-ion microscopy (FIM), scanning tunneling microscopy (STM), and noncontact atomic force microscopy (NCAFM) techniques proved to be of significant value. Prominent direct visualization of crystal surface atomic lattices and adsorbed species were first achieved by FIM and subsequently with the more versatile STM, generating revolutionary scientific insights (Müller, 1965; Binnig and Rohrer, 1987). Using cryogenic STM, addressing and positioning individual atoms became a reality (Eigler and Schweizer, 1990; Stroscio and Eigler, 1991) and was immediately recognized as an iconic achievement in nanoscale science. Likewise, insights into the essential electronic structure of materials were provided by means of local scanning tunneling spectroscopy (STS) (Feenstra, 1994) and space-averaging high-resolution spectroscopies, notably including angle-resolved photoemission (ARPES) (Damascelli, Hussain, and Shen, 2003). The combination of these powerful tools, ideally complemented with theoretical modeling, is an asset to fully characterize electronic properties and their implications (Gambardella *et al.*, 2003; Lobo-Checa *et al.*, 2009; Klappenberger, 2014; Galeotti *et al.*, 2020; Yin, Pan, and Zahid Hasan, 2021).

Bottom-up construction procedures were developed to design a wide variety of nanosystems amenable to scanning probe and space-averaging scrutiny. In particular, since the turn of this century, supramolecular chemistry principles have been increasingly employed to create low-dimensional functional nanostructures at well-defined interfaces (Barth *et al.*, 2000; Yokoyama *et al.*, 2001; Theobald *et al.*, 2003; Stepanow *et al.*, 2004). These are readily achieved by selecting appropriate molecular species with defined end groups favoring self-assembly into purely organic or metal-organic nanoarchitectures (Barth, Costantini, and Kern, 2005; Kudernac *et al.*, 2009; Kühnle, 2009; Dong, Gao, and Lin, 2016; Goronzy *et al.*, 2018; Xing *et al.*, 2019). In this context, supramolecular nanoporous networks were utilized as host lattices for the preferential trapping of guest species or as confining arrays for molecular motion (Theobald *et al.*, 2003; Stöhr *et al.*, 2007; Kühne *et al.*, 2010; Pivetta *et al.*, 2013; Nowakowska *et al.*, 2015; Zhang *et al.*, 2015; Nowakowska *et al.*, 2016; Teyssandier, Feyter, and Mali, 2016). Moreover, they provide significant potential for the incorporation of molecular switches in nanoelectronic circuits (Kocić *et al.*, 2019) or to host ligands suitable for gas sensing applications (Gutzler *et al.*, 2015; Čechal *et al.*, 2016; Écija *et al.*, 2018). In addition, metal-organic networks are attractive for exploring novel magnetic properties (Umbach *et al.*, 2012; Abdurakhmanova *et al.*, 2013; Gao *et al.*, 2020), catalytic effects (Gutzler *et al.*, 2015; Čechal *et al.*, 2016; Hötger *et al.*, 2019), mixed valency (Li *et al.*, 2012), and exotic tessellation patterns (such as quasicrystals and Archimedean tilings) (Urgel, Écija *et al.*, 2016; Yan *et al.*, 2017; Zhang *et al.*, 2018), with the added prospect of realizing exotic quantum phases including topological and quantum anomalous Hall insulators (Wang, Liu, and Liu, 2013; Dong *et al.*, 2016; Zhang, Wang *et al.*, 2016; Kumar *et al.*, 2018; Sun *et al.*, 2018; Gao *et al.*, 2019; Hernández-López *et al.*, 2021; Jiang, Ni, and Liu, 2021; Kumar *et al.*, 2021).

The extensive activities devoted to the exploration of quantum confinement and quasiparticle scattering at nanostructures on metal surfaces promoted the advancement of condensed matter research. This progress is revisited here, with the surface states of coinage metals taken as an exemplary playground. Hereby the design of appropriate nanoarchitectures customizes the electronic structure and topology of the outermost layers. We discuss the generally relevant aspects underpinning the scattering and confinement phenomena of two-dimensional electron gases (2DEGs)

existing at appropriate surfaces, listing prominent cases where firm control over such 2DEGs is exerted. We cover the groundbreaking quantum corral and resonator structures built by atomic manipulation and tackle more complex molecule-based arrangements and supramolecular self-assemblies. The latter enable an upscaling of the quantum properties due to the mesoscopic templating, which allows their exploration using space-averaging methods. In particular, we investigate the electronic structure of these systems mainly by two complementary experimental techniques: STM and STS at the atomic level and ARPES whenever large and homogeneous domains exist. Semiempirical methods are repeatedly used to simulate the molecular scattering potential landscape responsible for such 2DEG modification.

Moreover, we discuss electronic structure changes by artificial lattices affording exotic properties such as Dirac cones or flat bands (Gomes *et al.*, 2012; Slot *et al.*, 2017), topological edge states (Kempkes, Slot, van den Broeke *et al.*, 2019; Freeney, van den Broeke *et al.*, 2020), fractal behavior (Kempkes, Slot, Freeney *et al.*, 2019), and Penrose tiling quasicrystals (Collins *et al.*, 2017), some of which mirror the interesting physics of Bose-Einstein condensates (Greiner *et al.*, 2002; Ketterle, 2002; Park and Louie, 2009; Polini *et al.*, 2013; Zapf, Jaime, and Batista, 2014; Leykam, Andreanov, and Flach, 2018). In this respect, related emerging properties often exist after the modification of natural two-dimensional (2D) materials such as graphene, underpinning prospective fields such as twistronics (Cao *et al.*, 2018; Cao, Fatemi *et al.*, 2018). Similar attributes can also be induced and often systematically tuned exploiting the featureless dispersion of surface-state 2DEGs at metals by proper nanostructuring using adsorbed molecular species and sophisticated fabrication protocols (Yan *et al.*, 2019; Telychko *et al.*, 2021; Trainer *et al.*, 2022).

II. HARNESSING SURFACE STATES TO EXPLORE QUANTUM MECHANICAL PHENOMENA

Well-defined surfaces offer many interesting properties and have been studied extensively for over a century. With the development of ultrahigh vacuum technology, systematic investigations of the surface atomic arrangement and electronic structure became possible (Duke, 2003). In later years, atomistically clean metal surfaces served as versatile platforms for the construction of precisely defined nanoscale architectures, the dimensions of which fall below the wavelength of Fermi electrons whence the quantum regime is entered. Electron scattering with confining attributes on surfaces is encountered at natural defects or reconstructions, as well as nanostructures realized by STM tip manipulation (Chen *et al.*, 1998; Gross *et al.*, 2004; Pennec *et al.*, 2007; Klappenberger *et al.*, 2009; Lobo-Checa *et al.*, 2009; Cheng *et al.*, 2010; Wang *et al.*, 2013; Müller, Enache, and Stöhr, 2016; Martín-Jiménez *et al.*, 2019).

As illustrated in Fig. 1, reducing the spatial dimensions has a striking effect on the density of states (DOS) of a free-electron gas system (Ashcroft and Mermin, 1976). The smooth three-dimensional (3D) DOS distribution ($E^{1/2}$) evolves into a series of plateaus in two dimensions and reaches fully discretized "delta function" [$\delta(E-E_i)$] line

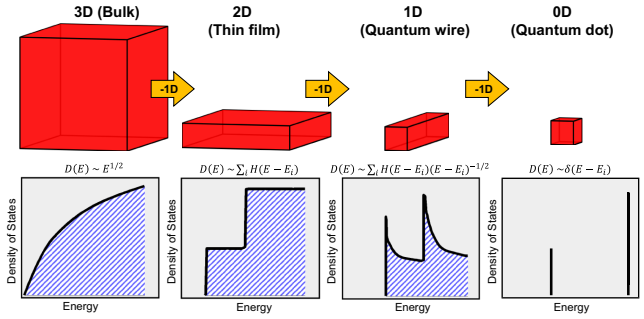

FIG. 1. Modification of the DOS distribution in a free-electron gas upon dimensionality reduction. The 3D smooth relation becomes progressively quantized as the system dimensions are decreased.

shapes in zero-dimensional (0D) systems, while in one-dimensional (1D) structures a convolution of the previous distributions is found.

The relevance of DOS modification by imposing spatial confinement in electronic systems can be gauged from its extensive application in the semiconductor industry, relying on ultrathin, quasi-2D electron systems for building electronic and computational devices (van Wees *et al.*, 1988; Brennan, 1999; Kanisawa *et al.*, 2001; Yoffe, 2001; Zwanenburg *et al.*, 2013). Even future quantum computation hardware is conceivable using tailored low-dimensional superconducting structures (Nayak *et al.*, 2008; Sato and Ando, 2017; Choi *et al.*, 2019). Because high-technology developments were stimulated by the fabrication of quantum wire (QW) and quantum dot (QD) architectures, understanding the wide range of fundamental properties of low-dimensional systems is important when exploring new applications (Wharam *et al.*, 1988; Tarucha *et al.*, 1996; Ohnishi, Kondo, and Takayanagi, 1998; van der Wiel *et al.*, 2002; Barth, Costantini, and Kern, 2005; Harrison, 2005; Hanson *et al.*, 2007; Pekola *et al.*, 2013). In particular, material engineering, molecular electronics, and quantum computation require the construction and exploration of artificial coupled or hybrid quantum materials (Kagan and Murray, 2015; Kagan *et al.*, 2016; Keimer and Moore, 2017; Tokura, Kawasaki, and Nagaosa, 2017; Broome *et al.*, 2018; Leon *et al.*, 2020; Walkup *et al.*, 2020). Possible candidates may emerge from 2D materials that exhibit long-range magnetic order (Gong *et al.*, 2017; Huang *et al.*, 2017), flat bands, or low-temperature superconductivity (Cao *et al.*, 2018; Cao, Fatemi *et al.*, 2018; Andrei and MacDonald, 2020; Kezilebieke *et al.*, 2020; Li *et al.*, 2021), providing a good platform to obtain distinct quantum states of matter.

A. Surface states providing canonical 2DEGs

Most model systems selected in this review to address the scattering and confinement properties of diverse artificial or self-assembled nanostructures exploit the well-known Shockley states present at the (111)-terminated coinage metal surfaces (i.e., Cu, Ag, and Au) (Shockley, 1939). These 2D surface states exist in the Γ-L projected bulk band gap (Kevan and Gaylord, 1987; Paniago *et al.*, 1995a). The pertinent electrons, which prevail exclusively at the

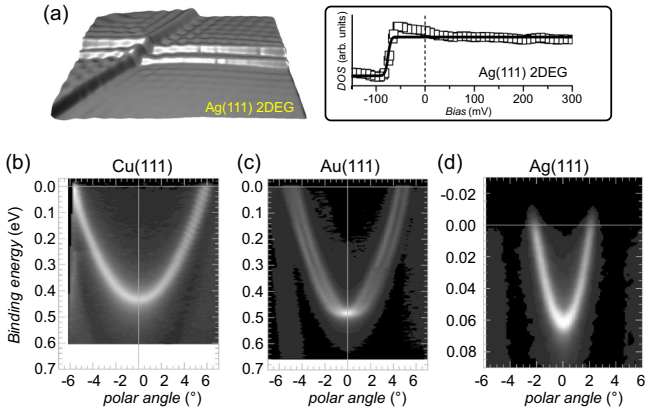

FIG. 2. DOS and band dispersions from 2DEGs on (111)-terminated noble metal surfaces. (a) Left panel: differential conductance (dI/dV) map overlaid with a topography image of a local region of Ag(111) hosting a few monatomic steps. The electron scattering at the step edges produces quasiparticle interference standing wave patterns. Right panel: the conductance spectrum of the Ag surface state reveals the typical steplike DOS distribution of a 2DEG. Adapted from Pennec *et al.*, 2007. (b)–(d) Parabolic dispersion relations of copper, silver, and gold fcc(111) Shockley states that are characteristic of 2D free-electron gases. The data for Au(111) show the spin-orbit splitting. Adapted from Reinert *et al.*, 2001.

outermost surface layers, behave as a quasifree 2DEG, unrestrictedly propagating parallel to the regular and pristine surface plane (Reinert *et al.*, 2001; Reinert and Hüfner, 2005; Malterre *et al.*, 2007; Tamai *et al.*, 2013; Oka *et al.*, 2014); see Fig. 2(a). Their quasifree character is mirrored in the parabolic dispersion [see Figs. 2(b)–2(d)] (Paniago *et al.*, 1995b; Reinert *et al.*, 2001) that follows the relation $E(k_\parallel) = E_0 + \hbar^2 k_\parallel^2/2m^*$, where E_0 is the fundamental binding energy of the surface state (i.e., the band minimum), m^* is the electron's effective mass, and $k_\parallel$ is the wave vector parallel to the surface; see Table I. The energy and wave vector can be directly probed using ARPES, which can currently access the spin-orbit splitting, encountered for Au(111) (LaShell, McDougall, and Jensen, 1996; Tamai *et al.*, 2013), and even the suggested topological properties in combination with two-photon photoemission (2PPE) (Yan *et al.*, 2015).

TABLE I. Parameters from the parabolic fits of the fcc(111) Shockley state dispersions shown in Fig. 2. E_0 corresponds to the fundamental binding energy (energy minimum), m^* refers to the effective mass, k_F represents the Fermi momentum, and λ_F corresponds to the Fermi wavelength. The component of the electron wave vector parallel to the surface ($k_\parallel$) is directly linked to the kinetic energy of the photoelectron (E_{kin}) and the polar angle (θ) through $k_\parallel[\text{Å}^{-1}] \approx 0.512\sqrt{E_{\mathrm{kin}}[\mathrm{eV}]}\sin(\theta)$. Values were taken from Reinert *et al.* (2001).

	E_0 (meV)	m^*/m_e	k_F (Å^{-1})	λ_F (Å)
Ag(111)	63 ± 1	0.397	0.080	78.5
Au(111)	487 ± 1	0.255	0.167/0.192	32.7/37.6
Cu(111)	435 ± 1	0.412	0.215	29.2

The isotropic dispersion of these Shockley states results in steplike DOS distributions that are characteristic of 2D systems (Fig. 1). The related electronic characteristics can be directly accessed at the atomic (local) scale by STS using differential conductance spectra (dI/dV) (Tersoff and Hamann, 1985); see Fig. 2(a). The observed local density of states (LDOS) correlates with the spatially integrated ARPES signals since the STS onset of the Shockley states closely matches the band bottom (fundamental) energies of these low-dimensional systems; see Figs. 2(a) and 2(d). Such technical complementarity is reliable whenever the electronic states of interest present their dispersion close to the $\bar{\Gamma}$ point (small $k_\parallel$) and are energetically located near the Fermi level. Note that small energy shifts (up to several tens of meV) may interfere due to tip-induced Stark effects in STS (Limot *et al.*, 2003) and different measurement temperatures (Paniago *et al.*, 1995b; Piquero-Zulaica, Nowakowska *et al.*, 2017).

Metal surface 2DEGs reside at the outermost atomic planes and are therefore sensitive to impurities in the form of adsorbed atoms or molecules (Bertel and Memmel, 1996; Kulawik *et al.*, 2005), structural defects such as atomic steps and vacancy islands (Crommie, Lutz, and Eigler, 1993b; Hasegawa and Avouris, 1993; Avouris and Lyo, 1994; Bürgi *et al.*, 1998; Li *et al.*, 1999; Rodary *et al.*, 2007), as well as thin overlayers comprising rare gases, alkali metals, etc. (Forster, Hüfner, and Reinert, 2004). In STM topographic data these effects become manifest and can be directly resolved when small bias voltages are applied at low temperatures, whereby Fermi level electrons dominate the tunneling current [Figs. 3(a) and 3(b)]. The pertinent electron density oscillations exhibit a standing wave character and are related to Friedel oscillations generated by pointlike charge impurities in bulk systems (Friedel, 1958), which can be rather

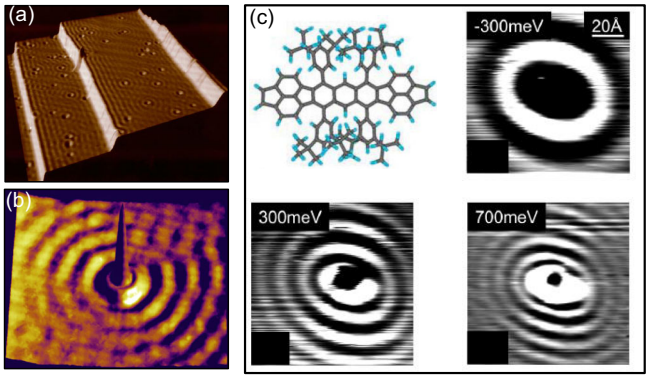

FIG. 3. 2DEG scattering by atomic and molecular adsorbates. (a) Three monatomic steps and about 50 point defects are visible on the Cu(111) surface. Spatial quasiparticle interference (QPI) patterns from the 2DEG scattering are visible (STM topographic image 50×50 nm^2). Adapted from Crommie, Lutz, and Eigler, 1993b. (b) Single Fe adatom on Cu(111). The concentric rings surrounding the Fe site correspond to a standing wave pattern due to the scattering of surface-state electrons (STM topographic image with 13×13 nm^2). Adapted from Crommie, Lutz, and Eigler, 1993a. (c) Molecules can efficiently scatter the surface electrons, as evidenced by the interference patterns of a so-called Lander molecule recorded at different energies. Adapted from Gross *et al.*, 2004.

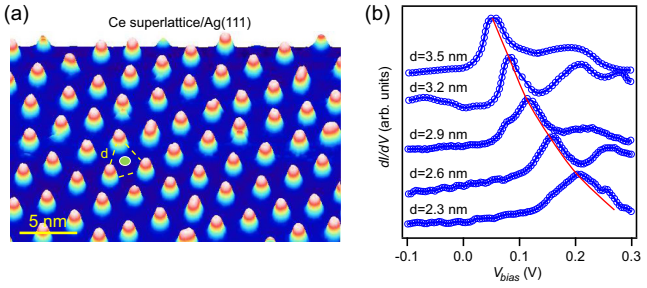

FIG. 4. Formation of surface-state-mediated superlattices: a self-organized Ce adatom array on Ag(111). (a) Constant-current STM image of 0.01 ML Ce on Ag(111) displaying an average distance $d = 3.2$ nm, obtained at $T = 3.9$ K. (b) Set of spectra taken in the center of a triangle formed by three Ce adatoms with a next-neighbor distance d. The adatom-adatom distance decreases with increasing Ce coverage, whereby a quadratic energy up-shift of the first resonance level is observed with shrinking QD size. Adapted from Ternes *et al.*, 2010.

pronounced depending on the material characteristics (Sprunger *et al.*, 1997). Such standing wave oscillations are recognized as quasiparticle interference (QPI) patterns originating from the constructive interference of electron waves after scattering at surface obstacles. Such bias-dependent dI/dV conversions can often provide access to the electronic band dispersion (in energy and momentum space) (Grothe *et al.*, 2013; Oka *et al.*, 2014).

Like single atoms, molecular adsorbates scatter surface 2DEGs and produce QPI patterns. In large molecular species a repulsive potential is typically generated by the charge distribution through the molecular backbone. As shown for isolated species, not all molecular moieties necessarily scatter in the same way (Gross *et al.*, 2004); see Fig. 3(c).

In addition, it should be noted that surface-state-mediated interactions exist, which can influence the spatial distribution of adsorbates at surfaces (Repp *et al.*, 2000; Knorr *et al.*, 2002; Ternes *et al.*, 2010). Under suitable conditions these adatoms are placed at positions reflecting an oscillatory interaction, arising due to the surface-state electrons, with $\lambda_F/2$ periodicity and $1/r^2$ decay, whereby r is the distance between neighboring adatoms (Repp *et al.*, 2000; Knorr *et al.*, 2002; Silly *et al.*, 2004; Ding *et al.*, 2007; Han and Weiss, 2012). These indirect interactions are also the driving force for the creation of superlattices of individual adsorbed atoms when the adatom concentration, the sample temperature, and the adatom diffusion barrier are in a subtle balance [Fig. 4(a)].

B. Principles of surface-state confinement and their modeling

To systematically engineer and confine freely propagating surface electrons, it is necessary to reduce the system's dimensionality to one or zero dimensions by building QW or QD structures. Since adatoms and vacancies (Crommie, Lutz, and Eigler, 1993b; Crommie *et al.*, 1995a; Li *et al.*, 1998, 1999; Kliewer, Berndt, and Crampin, 2001; Jensen *et al.*, 2005), molecules (Gross *et al.*, 2004; Shchyrba, Martens *et al.*, 2014), and step edges (Hasegawa and Avouris, 1993; Avouris and Lyo, 1994; Bürgi *et al.*, 1998) efficiently scatter the surface electrons, three distinct approaches were established to produce well-defined 2DEG confining nanostructures: (a) step arrays and nanogratings, (b) discrete artificial nanostructures via atomic or molecular manipulation, and (c) self-assembled atomic superlattices and molecular nanoporous networks; see Fig. 5 for a schematic representation. One-dimensional QWs in the form of step arrays and nanogratings confine the surface electrons to the X direction using periodically spaced scattering barriers, whereas, except for an energy shift, a free-electron behavior is kept perpendicular to it (in the Y direction); see Fig. 5(a). More restrictive are QDs that confine the electrons in all directions. In particular, QD superlattices emerge whenever the confinement occurs on the surface from pointlike (0D) scattering units periodically distributed in the nanoscale regime [Fig. 5(b)]. These scattering superlattices are often artificially realized via atomic or molecular manipulation, but also by self-assembly. A promising engineering approach to obtain coupled QDs exploits the spontaneous self-assembly of simple organic building blocks on surfaces. Thus, molecular nanoporous networks can be fabricated being purely organic or comprising metal-organic coordination motifs [Fig. 5(c)]. Note that the embedded metal centers and the molecules may scatter surface electrons differently, whence an interesting heterogeneous scattering potential landscape for the 2DEG

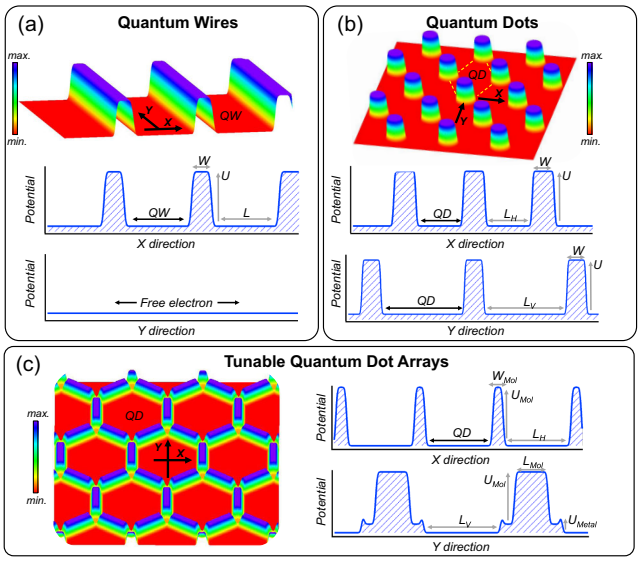

FIG. 5. Freely propagating surface-state electrons engineered via scattering superlattices. (a) One-dimensional electron grating made of scattering barriers [i.e., potential (U) times width (W)] separated by a distance L producing QWs. While surface electrons are confined in the X direction, they freely propagate in the Y direction. (b) Building an array of QDs via the precise positioning of 2DEG scattering pointlike (0D) barriers. This hexagonal superlattice produces an array of QDs where surface electrons are scattered mainly along the indicated directions while being less restricted in other orientations. As a result, an efficient coupling to adjacent QDs is obtained. (c) Well-encapsulated QD array. Shown is a situation with anisotropic barriers (compare the two profiles) affecting both 2DEG confinement and QD intercoupling, as later discussed for metal-organic nanoporous networks.

confinement and QD intercoupling emerges, the consequences of which are explained in Sec. V.

The surface-state confinement based on dispersive Shockley states is now generally well mastered. The fact that their Fermi wavelength falls into the nanoscale regime (see Table I), i.e., an order of magnitude larger than typical atomic spacing, greatly simplifies the calculations. Indeed, given the atomic nature of the scatterers and substrate, they can be approximated by distinct potential regions, as shown in Fig. 5. The problem is thus reduced to freely propagating electrons within homogeneous terraces interacting with potential barriers solely defined by the position of the scatterers (adatoms, array of atoms or molecules). This allows the utilization of well established calculation methods such as those widely used in the field of optics and photonics and/or simple analytical expressions derived from textbook quantum mechanics and solid-state physics. For example, electron confinement within a single metallic terrace defined by abrupt atomic steps (or chains of atoms) has been successfully modeled using the quantum mechanical 1D particle-in-a-box problem, assuming a fixed smooth (noncorrugated) potential at the terrace combined with symmetric-infinite (hard-wall) (Oka *et al.*, 2014), asymmetric infinite-finite (Avouris and Lyo, 1994), or symmetric-penetrable barriers at the step positions. Alternatively, this 1D confining system has been modeled by assuming the steps as semitransparent mirrors analogous to the optical Fabry-Perot interferometer (Bürgi *et al.*, 1998).

While neglecting sharp atomistic properties, the models capture the essential electronic features and resonance lifetimes when leaky barriers are considered. Likewise, electron scattering by a periodic array of steps at vicinal surfaces has been fully understood using the analytical solution of the canonical 1D Kronig-Penney model (Ortega *et al.*, 2011). Simple 2D confining structures such as quantum corrals have also been described using analytical expressions derived from the elastic scattering theory approach for the electron transmission and reflection at barriers (Harbury and Porod, 1996; Rahachou and Zozoulenko, 2004). Alternatively, they have been modeled as 2D particles in a box with either finite or infinite barriers (Crommie, Lutz, and Eigler, 1993a; Kumagai and Tamura, 2008).

The complexity of nanoarchitectures and 2D superlattices requires the use of numerical methods for their understanding. These can be adopted from models widely employed for photonic crystals, including plane-wave expansion (PWE), the finite element method, and the boundary element method (BEM) (Ram-Mohan, 2002). Using PWE has proven to be successful for the calculation of band structures of photonic crystals made of alternating materials with dielectric contrast. However, the method can be equally applied to surface electrons confined within homogeneous surface regions by periodic potential landscapes, i.e., nanoscale electronic superlattices that are 100-fold smaller than photonic crystals. Therefore, for electron PWE (EPWE) the scattering potential geometry is often constructed as a region of fixed potential defining the scatterers within a homogeneous substrate with abrupt changes at the boundary, i.e., a so-called muffin-tin potential. The potential Fourier coefficients are obtained for this predefined potential landscape and are fed into the Fourier space Schrödinger equation, frequently called the central or master equation, which is solved for the energies and wave functions using a simple eigenvalue problem (Abd El-Fattah *et al.*, 2019). Experimental quantities such as the LDOS and angle-resolved photoemission intensity provided by STS and ARPES measurements are then simulated using simple expressions involving the calculated eigenvalues and eigenvectors.

Although EPWE is applicable to nonperiodic and finite confining structures following the supercell scheme at the expense of computational cost, alternative methods were implemented. The electron BEM (EBEM), adapted from routines used in optics, was successfully used to model the confinement and/or propagation of surface electrons within finite nanostructures and at lateral interfaces (Knipp and Reinecke, 1996; García de Abajo *et al.*, 2010; Abd El-Fattah *et al.*, 2017; Kher-Elden *et al.*, 2017). Within the EBEM approach, the boundaries defining the muffin-tin potential are finely discretized, and electron sources placed at these boundaries are propagated through each potential region using the 2D Green's function of the Helmholtz equation (Klappenberger *et al.*, 2011; Kher-Elden *et al.*, 2017). The EPWE and EBEM approaches successfully describe the electronic properties of diverse confining structures. The general guidelines for the simulation procedures affording physically meaningful solutions are described in Sec. V.D.

Whereas methods based on the utilization of the atomic basis sets are not widely used for highly dispersive metallic systems, the tight-binding (TB) method was recently applied to describe a superlattice analogy to graphene, namely, molecular graphene (Gomes *et al.*, 2012), as well as other emerging artificial structures such as Lieb (Slot *et al.*, 2017), fractal (Kempkes, Slot, Freeney *et al.*, 2019), and kagome-honeycomb lattices (Telychko *et al.*, 2021). The method requires two fitting parameters (notably the on-site and hopping energies for the defined lattice) and yields a reasonable agreement with the experimental data. However, caution must be taken since nearest-neighbor TB disregards crosstalks with higher-order neighbors, as it is ubiquituous for plane-wave-like metallic systems. Thus, going beyond a qualitative comparison with experimental data bears risks for misinterpretations or, if higher-order hopping parameters are included, they can render the fitting process rather arbitrary and complex. For instance, nearest-neighbor TB predicts a perfectly flat band for CO molecule–based Lieb lattices close to the Fermi energy, which contrasts with the dispersing band obtained from muffin-tin-based calculations and the experiment (Slot *et al.*, 2017).

Finally, *ab initio* methods such as density functional theory (DFT) can provide the electronic structure of these finite and periodic confining nanostructures with great accuracy (Olsson *et al.*, 2004; Stepanyuk *et al.*, 2005; Díaz-Tendero *et al.*, 2008). However, such calculations come at the expense of large computational cost and complexity. Thus, considering the high level of success offered by the previously discussed modeling techniques, these extended atomistic calculations were only scarcely applied. Note that throughout this review comments will be provided regarding the modeling methods used for the particular systems considered.

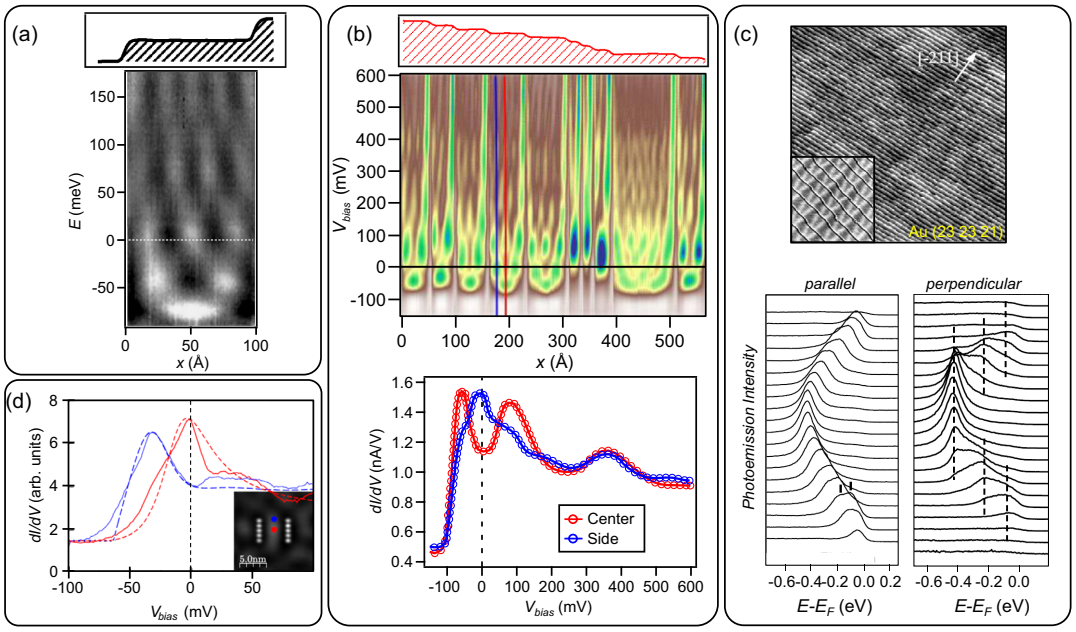

FIG. 6. One-dimensional confinement of 2DEGs via step arrays and atomic linear resonators. (a) Constant-current linescan over a 104 Å wide asymmetric resonator formed by two parallel steps. Adapted from Bürgi *et al.*, 1998. Lower panel: the pertinent LDOS across a terrace, which is characterized by a series of QWS resonances as a function of the energy resulting from the 1D electronic confinement. (b) dI/dV line spectra across an inhomogeneous step array formed by a five ML Ag film grown on a curved Au(111) substrate. The topographic profile is shown at the top of the panel. Lower panel: two selected tunneling spectra exhibiting different quantum well resonances at the center and the border of the same terrace, respectively. Adapted from Ortega *et al.*, 2018. (c) STM topography (250×250 nm^2) of a regularly stepped Au(23 23 21) vicinal surface (inset size 40×40 nm^2). Lower panels: ARPES EDCs show the dispersion parallel (left panel) and perpendicular to the step direction (right panel). A free-electron-like behavior (parabolic dispersion) appears parallel to the steps, whereas quasi-1D, weakly dispersing peaks (indicated by dashed lines) emerge perpendicularly to the steps. Adapted from Mugarza and Ortega, 2003. (d) Two strings of Co adatoms generated by tip manipulation on Ag(111) provide a resonator element. Shown are the experimental tunneling spectroscopy (solid line) and the calculated LDOS signature at the center [red (light gray) lines] and the end of the resonator [blue (dark gray) lines]. Adapted from Fernández *et al.*, 2016.

C. 2DEG confinement by inorganic atomic steps, corrals, and superlattices

In the following, different QW and QD systems constructed from inorganic materials as the scattering or confining entities are described. These will set the conceptual foundations for the subsequent molecular nanoarchitectures of interest.

One-dimensional electronic states spontaneously evolve on noble metal surfaces whenever parallel steps define single terraces [Fig. 6(a)]. Alternatively, they can be created artificially by arranging adspecies into parallel atomic wires [Fig. 6(d)]. The atomic steps efficiently backscatter the surface electrons [see Fig. 2(a)], producing confined states, commonly referred to as lateral quantum well states (QWSs), when the average terrace width falls below the surface-state electron coherence length (Bürgi *et al.*, 1998; Oka *et al.*, 2014); see Fig. 6(a). These QWSs can be modeled using infinite confining potential barriers at steps (Bürgi *et al.*, 1998; Ortega *et al.*, 2013), whence electron motion becomes restricted within the terrace with freedom to travel parallel to the steps (Ortega *et al.*, 2018). As observed in Fig. 6(b), the energy of such QWSs can be tuned by altering the terrace width or the atomic-row spacing (Negulyaev *et al.*, 2008; Fernández *et al.*, 2016).

This scenario becomes even more interesting whenever a periodic regular step array is created on the surface, going beyond two parallel steps or a set of terraces with different widths. Such regular vicinal crystals (Baumberger *et al.*, 2002, 2004; Shiraki *et al.*, 2004; Mugarza *et al.*, 2006) provide step superlattices giving rise to extended quasi-1D band structures that can be probed by nonlocal techniques such as ARPES. The electron confinement within the terraces leads to gapped and anisotropic dispersions accomplished by upward shifts of the 2DEG onset energy correlating inversely with the terrace size. Some electronic coupling between adjacent terraces emerges, which translates into finite step potential barriers that have to be taken into account (Mugarza *et al.*, 2006; Mitsuoka and Tamura, 2011; Ortega *et al.*, 2013). The physical nature of the modulated electronic bands can be captured with the 1D Kronig-Penney model (Mugarza *et al.*, 2006). There the steps are considered repulsive, in the form of square-shaped finite potential barriers of a magnitude $U_0 \times b$, where U_0 corresponds to the height of the barrier and b corresponds to its width (Ortega *et al.*, 2011). A good example of the resulting quasi-1D band structure is shown in Fig. 6(c) for the case of Au(23 23 21) featuring a miscut angle of $\alpha = 2.4°$ from the (111) plane (Mugarza and Ortega, 2003). By analyzing the energy distribution curves (EDCs), weakly dispersive peaks separated by energy gaps are observed in the direction perpendicular to the steps, whereas the parallel direction exhibits the expected unconfined parabolic

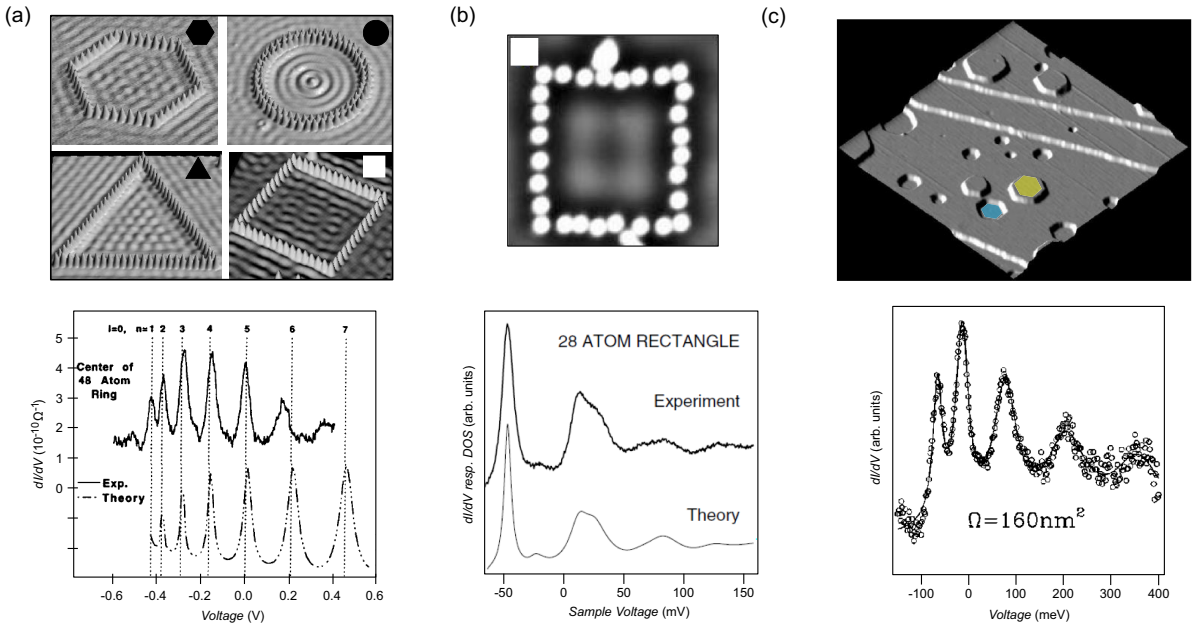

FIG. 7. 2DEG confinement via artificial quantum corrals and spontaneously formed nanoislands. (a) Hexagonal, circular, triangular, and square quantum corrals constructed using tip manipulation of Fe atoms on a Cu(111) surface. The hexagonal, triangular, and square sides correspond to approximately 8, 24, and 15 nm, respectively, while the inner diameter of the circular corral amounts to 14.3 nm. Adapted from Crommie, Lutz, and Eigler, 1993a. A characteristic STS spectrum at the center of one of these structures (48 Fe atom ring) is shown beneath. Adapted from Crommie *et al.*, 1995b. (b) Rectangular structure (9×10 nm^2) made up of 28 Mn atoms on Ag(111) and its corresponding STS spectrum and calculated LDOS at the corral center. Adapted from Kliewer, Berndt, and Crampin, 2001. (c) Upper panel: STM constant-current topographic image (160×160 nm^2) of quasihexagonal Ag adatom protrusions and vacancy islands on Ag(111). Adapted from Li *et al.*, 1999. Lower panel: typical STS acquired at a hexagonal island center. Adapted from Li *et al.*, 1998. In all cases, STS data indicate a broadened 0D LDOS distribution; cf. Fig. 1.

dispersion (Mugarza and Ortega, 2003). Overviews on vicinal surfaces were given by Mugarza and Ortega (2003) and Ortega *et al.* (2020).

Nanostructures enclosing specific surfaces provide notable electron confining properties (Fig. 7). Atomic arrangements constructed by tip manipulation methods were introduced as "quantum corrals" (Crommie, Lutz, and Eigler, 1993a; Heller *et al.*, 1994; Crommie *et al.*, 1995a, 1995b; Kliewer, Berndt, and Crampin, 2001) that exhibit distinct standing wave patterns, i.e., QPI phenomena revealing the 2DEG response to the confining geometries (such as hexagons, circles, squares, and triangles) (Kliewer, Berndt, and Crampin, 2001; Braun and Rieder, 2002; Lagoute, Liu, and Fölsch, 2005; Kumagai and Tamura, 2008). For some cases, the confining properties are almost element independent, whence different adatom species (such as Fe and Mn) result in similar STS signatures [Figs. 7(a) and 7(b)] (Crampin and Bryant, 1996). Moreover, at the corral center the DOS may feature a multipeak line shape stemming from confined resonances drifting apart as the enclosed area is reduced. The adatoms defining the quantum corrals were initially modeled as an impenetrable boundary, i.e., a hard-wall barrier, and thus the eigenstates and eigenenergies could be determined using a particle in a 2D box model of the corresponding geometry (Crommie, Lutz, and Eigler, 1993a; Kumagai and Tamura, 2008). However, a marked peak broadening (becoming more evident as the energy separates from the 2DEG onset) was experimentally detected, at variance with the signature anticipated for perfectly reflective quantum boxes. Thus, the nanostructure walls must be associated with finite-height, leaky barriers that reflect only a fraction of the incident amplitude (Heller *et al.*, 1994; Crommie *et al.*, 1995b; Harbury and Porod, 1996; Kliewer, Berndt, and Crampin, 2001; Fiete and Heller, 2003; Rahachou and Zozoulenko, 2004; Kumagai and Tamura, 2009; Tatsumi, Mitsuoka, and Tamura, 2018). The existence of inelastic absorptive channels has been ascribed to the coupling of surface electrons with bulk states (Crommie *et al.*, 1995a; Kliewer, Berndt, and Crampin, 2001; Fiete and Heller, 2003). To avoid specific assumptions or empirical input data, *ab initio* calculations based on DFT and a multiple scattering approach employing the Korringa-Kohn-Rostocker Green's function method were used to successfully describe the electronic structure of quantum corrals (Niebergall *et al.*, 2006). Alternatively, the elastic scattering theory approach (finite-height potential barriers) turned out to be a simpler model capable of reliably reproducing the experimental findings (Harbury and Porod, 1996; Rahachou and Zozoulenko, 2004). Furthermore, LDOS distributions similar to those encountered for quantum corrals were found in nanovacancies or islands created by gentle sputtering on Ag(111), i.e., without involving direct atom manipulation (Li *et al.*, 1998, 1999; Crampin *et al.*, 2005; Jensen *et al.*, 2005); see Fig. 7(c).

In addition, surface-state-mediated self-assembled arrays exhibit 0D partial confinement of the 2DEG. An example is the case of Ce adatoms on Ag(111), where the atoms

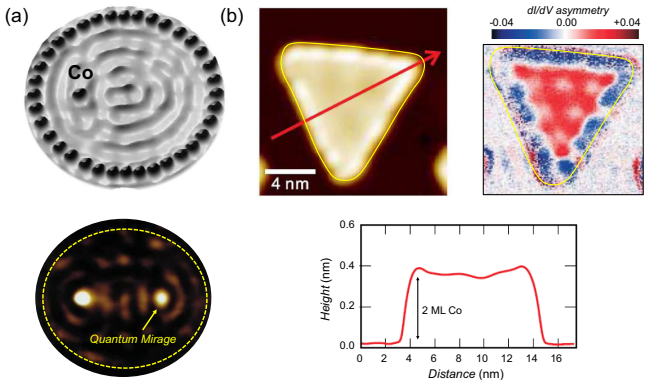

FIG. 8. Magnetism effects induced in quantum corrals and thin films. (a) Elliptical electron resonator with a Co atom at the left focus (STM image size is approximately 15×13.2 nm^2). The associated dI/dV map shows the Kondo effect projected to the empty right focus. Adapted from Manoharan, Lutz, and Eigler, 2000. (b) Constant-current STM image of a two ML Co triangular island on Cu(111). Its line profile along the arrow crossing the island provides evidence of the two atomic layer height. The experimental dI/dV asymmetry map measured near the Fermi level at $V = 0.03$ V and $B = -1.1$ T shows a magnetic contrast between the center and edge of the island. Adapted from Oka *et al.*, 2010, 2014.

arrange in perfectly ordered triangular QD units, the size of which can be altered with careful coverage control (Silly *et al.*, 2004; Ternes *et al.*, 2004, 2010); see Fig. 4(a). With increasing Ce concentration, the position of the first confined state shifts quadratically to higher energies with decreasing average interatomic distance d, as shown in Fig. 4(b). Note that the Ag surface state becomes depopulated in these cases and appears in the unoccupied regime ($E > E_F$), where resonances in the form of LDOS peaks appear. Moreover, not only ordered superlattices but also disordered ones can confine the 2DEG. In this regard, Jäck *et al.* (2021) succeeded in generating and probing the multifractal wave functions of a disordered 2DEG, using the mixed surface alloy BiPb/Ag(111).

The quantum corrals can also be regarded as artificial atoms in view of their discrete electronic levels. In recent work their out-of-plane bonding properties were explored using NCAFM with a CO-functionalized tip as probe. The measured interactions are weak, whereby covalent attraction to metallic and repulsions for CO-terminated tips could be discriminated (Stilp *et al.*, 2021).

It is possible to go beyond purely electronic effects by constructing specially configured quantum corrals enclosing magnetic impurities. For instance, the so-called quantum mirage gives rise to notable nanomagnetic phenomena upon positioning a single Co adatom at one focus of an ellipsoidal quantum corral (Manoharan, Lutz, and Eigler, 2000; Stepanyuk *et al.*, 2005); see Fig. 8(a). The Co adatom Kondo signature becomes replicated (with reduced intensity) at the second, pristine (Co-free) focal point. Therefore, the 2D confined Cu surface-state electrons form the medium through which the magnetic moment of the Co adatom is projected to the opposite focus (Stepanyuk *et al.*, 2005; Rossi and Morr, 2006; Figgins *et al.*, 2019). Recently the purely electronic mirage effect was also demonstrated using Fe and Ag adatoms (Li *et al.*, 2020). By placing a dehydrogenated H_2Pc molecule in one focal point of an elliptical quantum corral and the STM tip in the other, it was possible to coherently focus electrons onto the molecule, leading to an almost tripled switching probability (Kügel *et al.*, 2017).

Overall, the quantum size effects in corrals or nanoislands promote important effects, such as the observation of quantum-guided diffusion and adatom self-assembly, the control of statistical fluctuations, the tunability of the Kondo temperatures, and the buildup of atomic logic gates (Li, Cao, and Ding, 2020). For further information on quantum corrals see Fiete and Heller (2003) and Oka *et al.* (2014).

Furthermore, adsorbed magnetic clusters provide additional magnetic effects triggered by confinement. For example, triangular two monolayer (ML) thick Co islands on Cu(111) display not only efficient confinement of the Cu 2DEG but also spin-dependent quantum interference effects [Fig. 8(b)]. Differential tunneling conductance (dI/dV) asymmetry maps show strong position-dependent signals within the Co islands. A rim state localized at the edges originates from minority d states, while the modulation pattern at the inner part shows the opposite (majority) spin character, which is ascribed to the electron quantum confinement of the free-electron-like sp surface state (i.e., the Cu 2DEG) (Pietzsch *et al.*, 2006; Oka *et al.*, 2010, 2014). A similar spin-confinement interplay effect has been demonstrated by the analysis of QPI phenomena on Bi(110), where spin-orbit interactions entail a marked surface-state splitting, emphasizing that their spin character cannot be neglected (Pascual *et al.*, 2004).

While this review focuses mainly on nanostructures fabricated on noble metals, note that genuine interest in other material platforms with complementary quantum electronic properties exists. Indeed, in recent years 2DEG scattering and confinement have been examined for a series of prototypical topological insulator materials that present an insulating bulk and topologically protected spin-split surface states (C. Zhang *et al.*, 2020; Sobota, He, and Shen, 2021). Owing to their interesting quantum nature, in stark contrast to the previously described scenarios, noteworthy effects occur in these materials, including the enhanced transmission through steps (Seo *et al.*, 2010). Moreover, an analysis of confinement patterns for the scattering of topological states from Ag impurities and step edges on the $Bi_2Te_3(111)$ surface indicated a complete suppression of electron backscattering due to the manifestation of time-reversal symmetry (Zhang *et al.*, 2009). However, more recent studies on such substrates decorated by triangular Bi quantum corrals displayed quasibound states indicative of topological surface-state confinement effects (Chen *et al.*, 2019). Based on these findings, selection rules were suggested, governed by the shape and spin texture of the surface-state constant energy contour upon the strong hexagonal warping in the substrate (C. Zhang *et al.*, 2020; Sobota, He, and Shen, 2021). In more recent work, the dual (weak-crystalline) topological material Bi_2TeI was spectroscopically investigated and displayed distinct 2D Dirac surface states behaving differently in the vicinity of atomic steps and susceptible to mirror symmetry breaking (Avraham *et al.*, 2020). Related to these findings is the demonstration of spin-polarized midgap states at odd atomic step edges of

stoichiometrically controlled PbSnSe alloys featuring topological crystalline insulator surfaces (Sessi *et al.*, 2016). In addition, the Shockley states of Au(111) and other noble metals can be interpreted as topologically derived surface states of a topological insulator (Yan *et al.*, 2015).

A noteworthy effect of noble metal surface states is that they can be made superconductive through the proximity effect (Potter and Lee, 2012; Wei *et al.*, 2019). Using a hybrid material platform consisting of a thin Au(111) film on a superconducting vanadium substrate and patterned EuS to additionally magnetize the surface-state electrons via exchange coupling, the signatures of so-called Majorana zero modes could be accessed (Manna *et al.*, 2020).

In the following, we focus on the electronic confinement and scattering properties induced by molecular nanoarchitectures fabricated on (111)-terminated metals featuring Shockley-type 2DEGs. Prominent examples from the last two decades that demonstrate control over the surface-state confinement using molecular arrays are discussed in detail, including finite confining structures obtained by tip manipulation protocols affording CO artificial lattices (such as hexagonal, Lieb, and fractal ones) and vacancy arrangements in close-packed molecular layers. We also discuss extended molecular structures obtained by supramolecular and metallo-supramolecular self-assembly protocols. They manifest as nanogratings, regular networks (such as kagome, rectangular, and rhombic lattices), triangular and fractal structures, and tunable nanoporous honeycomb arrays. Finally, the placement of guest species into open supramolecular grid structures is revisited, which leads to a distinct route for self-assembly and for altering surface electronic features.

III. DEFINING QUANTUM STATES USING MOLECULAR MANIPULATION

Molecular adsorbates, apart from scattering surface 2DEGs similar to single atoms, may bestow increased complexity and tunability upon the generated nanoarchitectures, which can be advantageous for confinement control. Note that CO positioning on Cu(111) was used extensively to manipulate electron waves in closed geometries (Moon *et al.*, 2008, 2009). This construction scheme is interesting since prescient theoretical considerations suggested that, under an appropriate external periodic potential of hexagonal symmetry, massless Dirac fermions emanate from 2DEGs near the corners of the supercell Brillouin zones (Park and Louie, 2009). The latter was validated at the mesoscopic scale using a superimposed nanofabricated quantum well lattice on gallium arsenide (Singha *et al.*, 2011), and at the nanometer scale by creating an artificial honeycomb "molecular graphene" sheet utilizing CO molecules on the Cu(111) surface (Gomes *et al.*, 2012). The results showed that atomically precise DOS engineering provides access to new physics, and many further noteworthy results have since been obtained (Khajetoorians *et al.*, 2019; Yan and Liljeroth, 2019; Yan *et al.*, 2019).

Currently two manipulation protocols exist for the design of scattering barriers and geometries to modify the surface 2DEG: (i) the unit by unit construction of artificial lattices over pristine surface regions, and (ii) the removal of adspecies from an extended and periodic molecular layer to generate vacancies that expose well-defined patches of the substrate. Fully automated assembly protocols have been demonstrated in this context (Celotta *et al.*, 2014).

A. Artificial 2D lattices

A pioneering study demonstrating quantum state control employed a triangular lattice designated as molecular graphene constructed by tip manipulation of CO molecules on a Cu(111) surface (Gomes *et al.*, 2012). Indeed, the resulting band structure features Dirac cones analogous to graphene, which is derived from the modified 2DEG; see Fig. 9(a). Each CO unit acts as a repulsive barrier to the surface electrons that get confined within the honeycomb grooves left between the molecules and create a strong depletion of states (conductance dip in STS), characteristic of Dirac-like band structures. The Dirac dispersion is located at the $\bar{K}$ point of the superstructure Brillouin zone [close to the Cu(111) $\bar{\Gamma}$ point] instead of the $\bar{K}$ point for freestanding graphene. By tuning the unit cell size (i.e., CO separation), it was possible to control the level of doping in the system. Connecting adjacent artificial graphene lattices with different periodicity permitted the creation of atomically sharp *p*-*n*-*p* junctions. In addition, the effect of triaxial strain on the electronic structure of artificial graphene was studied, with pseudomagnetic fields simulated up to 60 T (Gomes *et al.*, 2012). Closely related artificial graphene layers at the mesoscale were recently reported by growing regular C_{60} monolayer superlattices on Cu(111) (Yue *et al.*, 2020). Moreover, by arranging coronene molecules on Cu(111), artificial electronic kagome-honeycomb lattices (Telychko *et al.*, 2021), hexagonal boron nitride (*h*-BN) (Yan *et al.*, 2019), and zigzag graphene nanoribbons (GNRs) (Wang *et al.*, 2014) were fabricated. The armchair GNR counterpart was achieved by CO manipulation, whereby a careful tuning of arrangements facilitated the observation of topological states (Trainer *et al.*, 2022).

Using the established CO manipulation strategy, series of lattice configurations were systematically explored, among them Lieb lattices (Slot *et al.*, 2017), Sierpiński triangle fractals (Kempkes, Slot, Freeney *et al.*, 2019), Penrose tiling quasicrystals (Collins *et al.*, 2017), and topological state hosting nanostructures (Kempkes, Slot, van den Broeke *et al.*, 2019; Freeney, van den Broeke *et al.*, 2020). The case of a Lieb lattice was addressed by adding extra CO molecules at the center of alternating voids of a CO square lattice [displayed as X's in Fig. 9(b)]. The repulsive CO potentials deplete the surface electrons in their surroundings and yield a band structure composed of Dirac cones at the Brillouin zone edges and an extended flat band at the Dirac energy. This electronic structure is reflected in the position-dependent STS: at the corner sites the two peaks exist (lowest and highest energies of the dispersive bands) with a strong attenuation in between marking the Dirac point, which converts into a maximum in the spectra at the edge sites, evidencing the existence of the flat band. Although flat bands principally give rise to an extremely narrow feature in the LDOS, the peak at −0.07 V observed above the edge sites is fairly broad. This behavior was attributed to the influence of next-nearest-neighbor hopping, as well as to the limited lifetime of

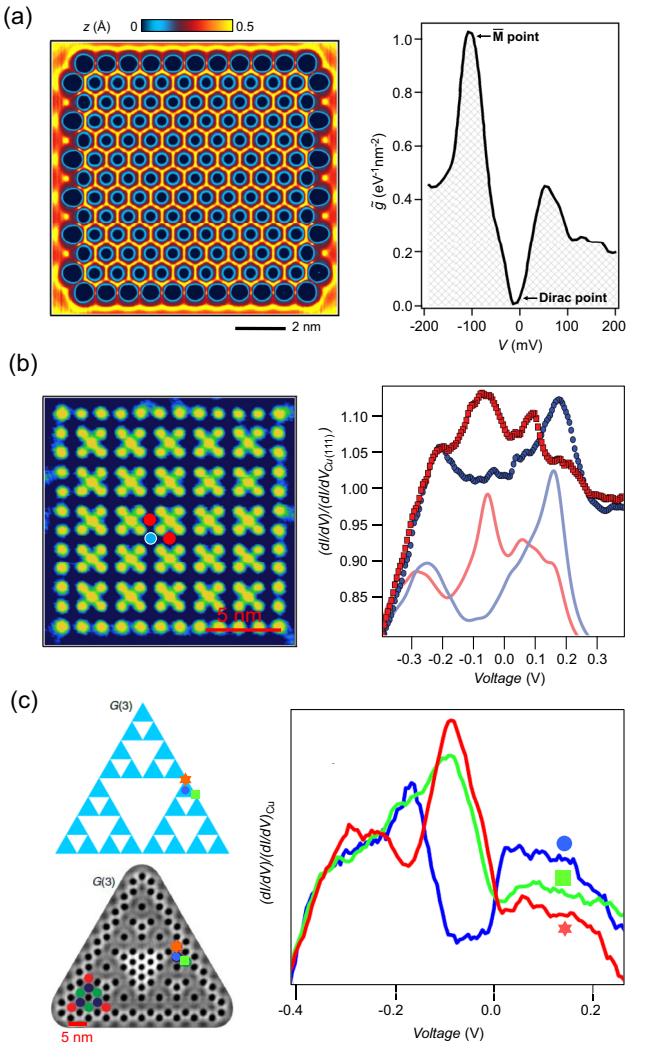

FIG. 9. Two-dimensional lattices created by serial positioning of CO on Cu(111). (a) Artificial graphene lattice generated by manipulation of 149 CO molecules and corresponding spatially averaged STS that features a V-shaped curve characteristic of a Dirac-like band structure. Adapted from Gomes *et al.*, 2012. (b) Left panel: Artificial Lieb lattice (dark regions) imposed on Cu(111) 2DEG [CO molecules appear as green (white) circles]. Right panel: normalized STS curves acquired at the corner [blue (lighter gray) dot] and edge [red (dark gray) dot] sites. Adapted from Slot *et al.*, 2017. (c) Model and constant-current STM image of the $G(3)$ Sierpiński triangles lattice generated by CO molecules on Cu(111). The atomic sites of one $G(1)$ building block (bottom left panel) are indicated. The normalized differential conductance spectra acquired at selected sites of the nanostructure are reproduced with the same color coding in the left panels. Adapted from Kempkes, Slot, Freeney *et al.*, 2019.

the surface-state electrons. The experimentally observed differential conductance spectra are well reproduced when next-nearest-neighbor hopping is included in TB calculations of a finite lattice. This hopping is essential to account for the observed asymmetry in the LDOS of the low- and high-energy bands [blue (black) spectrum, peaks at −0.20 and +0.18 V], as well as for the peak at +0.09 V in the edge-site spectrum [red (dark gray)] (Slot *et al.*, 2017). Note that such Lieb lattices were recently also predicted for the case of a molecular covalent organic framework (COF) (Jiang *et al.*, 2020).

In essence, the desired band structures are generated by manipulating the molecules into the edges that define the traces of artificial 2D lattices. In this way, fractal arrangements such as the one shown in Fig. 9(c) can be created (Kempkes, Slot, Freeney *et al.*, 2019). The realized Sierpiński triangles bestow noninteger or fractional dimensions to the surface electrons that inherit the fractional dimension of the spaces left by the molecules, such that their delocalized wave functions decompose into self-similar parts at higher energies. Figure 9(c) (left panel) shows a third generation Sierpiński triangle $[G(3)]$ consisting of three triangles of second generation $[G(2)]$ sharing the corner sites. In the right panel of Fig. 9(c), the experimental LDOS acquired by STS at selected sites in the $G(1)$ triangle is shown. The different confined state peaks corroborate the 2DEG trapping in this Sierpiński geometry. Thus, it was determined that the electronic wave functions inside the triangular structure inherit the respective scaling properties (Kempkes, Slot, Freeney *et al.*, 2019).

The systematic configuration of artificial lattices can be exploited to study fundamental aspects of intercoupling and topologically protected edge states at the local scale. For instance, triangular lattices constructed following breathing kagome geometries by alternating weak and strong bonds, not only open a band gap between the bottom and middle bands at the K point, but also exhibit topological states at their corners (Kempkes, Slot, van den Broeke *et al.*, 2019); see Fig. 10(a). These corner modes are proposed to feature protection by a generalized chiral symmetry, providing robustness against perturbations. In contrast to conventional topological insulators, this lattice was initially understood as a higher-order topological insulator since the corner modes have two dimensions fewer than the bulk. However, a more recent theoretical analysis indicated that a breathing kagome lattice does not necessarily display higher-order topology. Indeed, corner modes of trivial nature are deduced, showing a certain degree of protection against perturbations while respecting generalized chiral and crystalline symmetries and the lattice connectivity (van Miert and Ortix, 2020; Jung, Yu, and Shvets, 2021; Herrera *et al.*, 2022). Note that not all edge geometries and intercouplings in triangular Kekulé-type lattices [Figs. 10(b) and 10(c)] are able to host topological edge modes (Freeney, van den Broeke *et al.*, 2020).

Generally, in these lattices the resulting artificial-atom sites have *s*-like character in their lowest energy signatures. By extending the studies to higher states, *p*-band engineering becomes accessible, i.e., manipulation of fourfold and threefold rotational symmetry of *p*-orbital bands (Slot *et al.*, 2019; Gardenier *et al.*, 2020). As shown for the Lieb lattice in Fig. 10(d), the degeneracy of p_x- and p_y-like orbitals can be lifted by introducing asymmetries (Slot *et al.*, 2019). Moreover, these higher p orbitals can give rise to distinct electronic structures with flat bands and Dirac cones in a honeycomb lattice configuration; see Fig. 10(e) (Gardenier *et al.*, 2020).

A further matter of interest is the systematic study of coupling effects between quantum corrals. Recently rectangular and triangular structures in dimer and trimer arrangements were fabricated using the base units of CO/Cu(111)

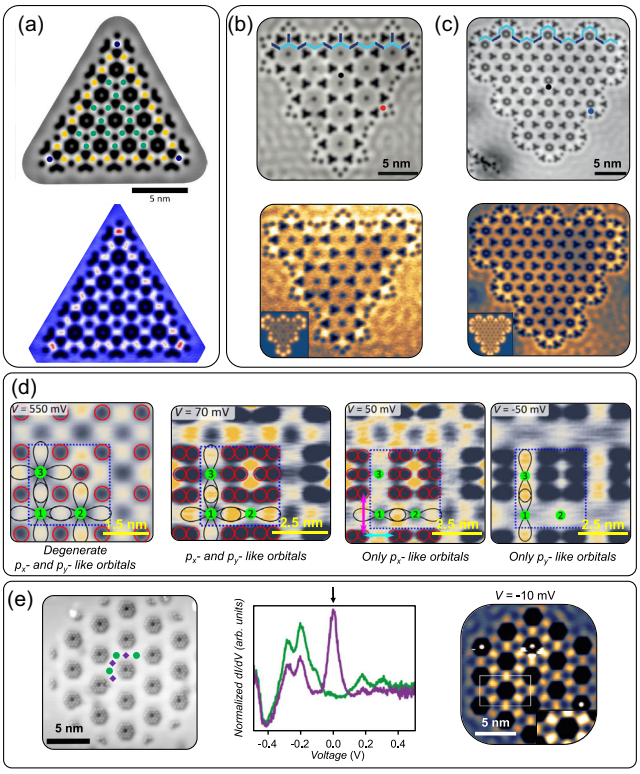

FIG. 10. Design of quantum states using artificial 2D lattices of precisely arranged CO on Cu(111). (a) Robust corner localized zero-energy modes in a seemingly electronic higher-order topological insulator. Adapted from Kempkes, Slot, van den Broeke *et al.*, 2019. (b),(c) Topological edge modes arising at Kekulé lattices with partially bearded and molecular zigzag edge terminations. Adapted from Freeney, van den Broeke *et al.*, 2020. (d) Manipulation of higher-energy p-orbital bands in artificial lattices with fourfold rotational symmetry. By tuning the lattice, the degeneracy of p_x and p_y orbitals can be lifted. Adapted from Slot *et al.*, 2019. (e) Enlarged honeycomb lattice with practically unmixed orbital bands. The double peak at lower energies corresponds to the s Dirac cone, the sharp peak marked with the black arrow relates to a p-orbital flat band (visualized in the conductance map in the right panel), while the highest-energy double peak corresponds to a p-orbital Dirac cone. Adapted from Gardenier *et al.*, 2020.

platforms. These exhibited differences in their QPI with respect to totally closed structures. Their electronic features could be understood using single-particle pictures based on muffin-tin or TB models, the latter of which is often applied to describe the coupling of atoms or molecules (Freeney, Borman *et al.*, 2020).

In addition, such closed nanoarchitectures were also explored for overcoming the single-atom limit for information storage density. Specifically, using the coherence of the 2DEG of Cu(111), quantum holograms composed of individually manipulated CO molecules were fabricated that projected an electron pattern onto a portion of the surface. This innovative idea was further developed theoretically by introducing quantum spin holography, which additionally allowed information to be stored in two spin channels independently (Moon *et al.*, 2009; Brovko and Stepanyuk, 2012). For further reviews on artificial lattices see Khajetoorians *et al.* (2019), Yan and Liljeroth (2019), and Freeney *et al.* (2022).

B. Molecular vacancies and trenches

The second manipulation protocol uses molecules that are weakly bound to the surface and that frequently aggregate into extended periodic islands stabilized by attractive intermolecular interactions (Huang *et al.*, 2011). These molecular films can be locally disrupted by a controlled removal of single units using a STM tip, creating artificial nanoscale vacancies or molecular trenches (Seufert *et al.*, 2013). Within these voids, the pristine surface-state electrons emerge; i.e., 2DEG engineering can be carried out at the local scale by manipulating the geometries that induce the electron confinement.

A good example is provided by the tetraphenyl porphyrin (TPP) monolayer assembled on Ag(111) (Seufert *et al.*, 2013). This film exhibits an interface state with quasi-free-electron-like character (Auwärter *et al.*, 2010; Caplins *et al.*, 2014; Galbraith *et al.*, 2014). Linear structures with variable length in multiples of 1.4 nm can be fabricated (Auwärter *et al.*, 2010), as shown in Fig. 11(a). The molecules defining these trenches act as scattering barriers to the surface electrons that get confined within, as extracted from STS. Increasing the length of these linear structures shows that the first confined resonance shifts toward the Ag(111) reference, in agreement with a particle-in-a-box case. In the longest chain (with four removed molecules) the second confined state peak is visible at ∼200 mV. Note that the confinement signature is present in the unoccupied region ($E > E_F$) (Neuhold and Horn, 1997; Morgenstern, Braun, and Rieder, 2002).

This manipulation method is ideally suited to engineering specific configurations as 1D chains or 2D artificial lattices and also to performing fundamental studies on QD intercoupling phenomena. Figure 11(b) compares a single molecular vacancy, analogous to an isolated QD, with a linear trimeric structure (1D) and a crosslike assembly (2D). The STSs recorded at the central cavities become significantly modified by the number of nearest-neighbor QDs. This is due to the electron intercoupling through the leaky molecular wall. The overlap between neighboring electronic states results in asymmetric and broadened spectra reflecting a wave function delocalization. Periodically repeating these coupled QD structures gives rise to bonding and antibonding continuum states [Figs. 11(c) and 11(d)]. These will generate a defined band structure whose fundamental energy is established by the bonding states, and the overall peak width ($\Delta\epsilon$) (which is proportional to the QD interaction) is determined by the antibonding ones. The probability density for the bonding state is laterally more spread out than the antibonding one, the latter of which extends further into the vacuum (Seufert *et al.*, 2013); see Fig. 11(c). Consequently, the STS technique probes the antibonding state more efficiently than the bonding one (Piquero-Zulaica *et al.*, 2017).

We envision that artificial lattices similar to those discussed previously could also be built with a removal of molecules in square or hexagonal self-assembled monolayers (Seufert *et al.*, 2013; Udhardt *et al.*, 2017), whereby the hopping parameters could be further tuned with the use of

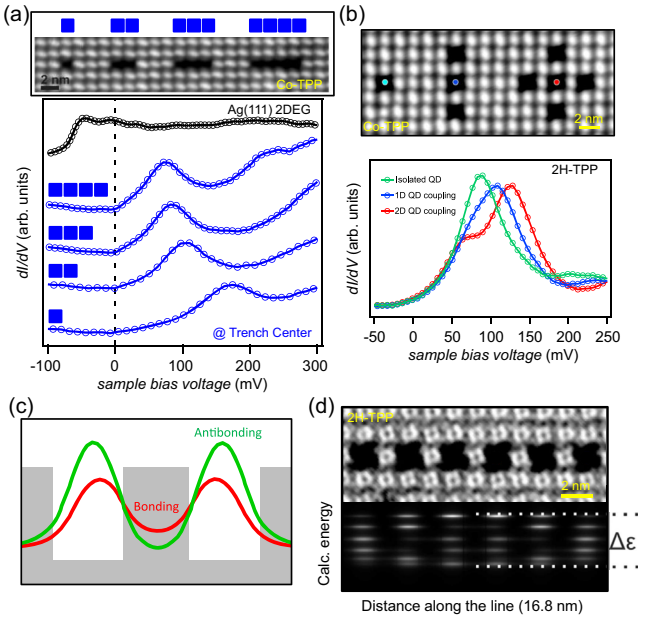

FIG. 11. Examples of molecular trenches created by tip removal of single units in tetraphenyl porphyrin arrays self-assembled on Ag(111). (a) Top image: STM image showing four differing length quantum wells generated by the removal of one to four molecules. The STS spectra below, acquired at the trench centers, display a continuous shift of the first bound resonance, as the trench extends in length, toward the Ag(111) surface-state onset at −65 mV (black curve). (b) STM image presenting three monomer vacancies (single QDs) surrounded by a different number of identical neighbors: none on the left, two in line at the center, and four in a crosslike geometry on the right. Tunneling spectra acquired at the central sites [obtained from the colored (gray scale) dots in the upper STM image] display spectroscopic differences that relate to QD intercoupling effects through the single molecular barriers. (c) Simplified model of two identical and coupled quantum wells with a bonding [red (dark gray)] and antibonding [green (gray)] state. The antibonding probability density protrudes further into the vacuum than its bonding counterpart. (d) EBEM simulation (bottom panel) of six coupled QDs (top panel) that shows an intermediate stage to the formation of continuum states (1D band). The top and bottom energies are defined by the antibonding and bonding states displayed in (c). Adapted from Seufert *et al.*, 2013.

"blends" (mixture of two building blocks) (Wintjes *et al.*, 2010; Stadtmüller *et al.*, 2014; Goiri *et al.*, 2016; Bouju *et al.*, 2017; Girovsky *et al.*, 2017). Following a similar strategy, the vacancy engineering approach was explored using atomic platforms, whereby Cl monolayer islands on the Cu(100) surface proved to be versatile. In this case, the atomic manipulation produces defect arrays with localized electronic vacancy states. In particular, an automated digital atomic-scale memory could be realized (Kalff *et al.*, 2016), along with topological states within Lieb lattices (Drost *et al.*, 2017) as well as trimer and coupled dimer chains (Huda *et al.*, 2020). The significant potential of this method is recognized and was successfully exploited to study emergent band formations in lattices of varying structure, density, and size (Girovsky, Lado *et al.*, 2017).

IV. QUANTUM RESONATORS IN SUPRAMOLECULAR GRIDS

The molecular manipulation experiments confirm that the generated barriers and their geometry can be used for tuning the 2DEG confinement, giving rise to novel physical phenomena. Moreover, the interwell coupling is adjustable using a deliberate choice of molecules and geometries. However, the underlying serial processes imply specific conditions, such as manipulable building units and cryogenic environments typically requiring extensive construction times for the desired nanoarchitectures. Additionally, the overall lateral area of the designed structures is too small to meet the dimensions needed for practical applications. Thus, from the points of view of formation, upscaling, and stability it is advantageous to explore alternative fabrication routes. Supramolecular building protocols are an ideal choice since they rely on self-assembly and self-correction processes that can extend simple structural units repeatedly and produce robust, highly regular, extended homoarchitectures with good control while simultaneously engineering the system's electronic structure at the mesoscopic level.

Indeed, molecular structures in the form of 1D nanogratings and 2D open networks that efficiently scatter and confine surface 2DEGs can currently be realized (Barth, 2007; Dong, Gao, and Lin, 2016; Müller, Enache, and Stöhr, 2016). Thus, engineering the LDOS and the interpore coupling is feasible and results in unprecedented band structures. As demonstrated in Figs. 12 and 13, a careful design and choice of presynthesized molecular building blocks allows for precise control over the size and shape of the nanoarchitectures, providing command over the overall electronic properties. Key examples of self-assembled geometries with demonstrated 2DEG confining capabilities are highlighted next. The following reviews on molecular self-assembly (Barth, 2007; Kudernac *et al.*, 2009; Kühnle, 2009; Han and Weiss, 2012; Klappenberger, 2014; Goronzy *et al.*, 2018) and metallo-supramolecular engineering on surfaces are recommended for further reading (Lin *et al.*, 2008; Barth, 2009; Bartels, 2010; Klyatskaya *et al.*, 2011; Dong, Gao, and Lin, 2016; Écija *et al.*, 2018).

A. One-dimensional organic nanogratings

Straight molecular chains expressing hydrogen-bonded 1D nanogratings were obtained with self-assembly processes using suitable precursors on mildly reactive and smooth metal surfaces (Barth *et al.*, 2000; Weckesser *et al.*, 2001; Pennec *et al.*, 2007). The linear structure formation is driven by the interplay between molecule-molecule and molecule-substrate interactions. For the case of *L*-methionine molecules on Ag(111) [see Figs. 14(a) and 14(b)], ammonium and carboxylate groups interact and form zwitterionic dimer units (Schiffrin *et al.*, 2007). Like inorganic step arrays at vicinal surfaces, the molecular chains scatter the 2DEG, whereupon 1D confinement takes place. Accordingly, the differential conductance scan in Fig. 14(c), acquired along a line perpendicular to the chains [Fig. 14(b)], reproduces the three lowest resonator states (featuring zero, one, and two nodes). The energy of these QWSs follow a quadratic inverse relation

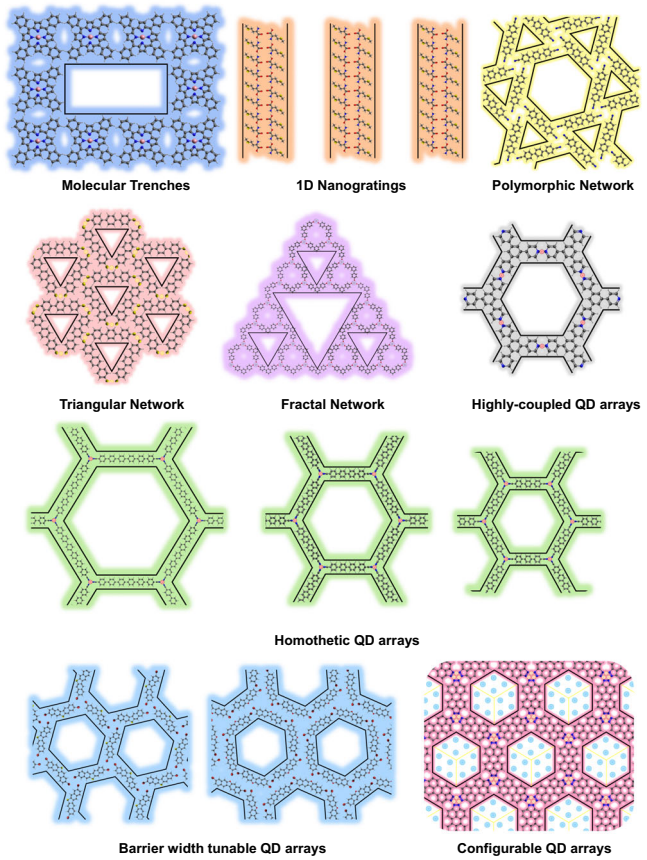

FIG. 12. Schematic representation of exemplary supramolecular motifs discussed throughout this review. This compilation provides an idea of the molecular nanostructure versatility that can be generated on suitable smooth metal surfaces to tune and engineer their 2DEGs.

with the quantum well size [as shown in Fig. 14(d) for the $n = 1$ resonance], which is accurately reproduced using the Fabry-Perot model that describes quantization effects between finite parallel potential barriers (Bürgi *et al.*, 1998).

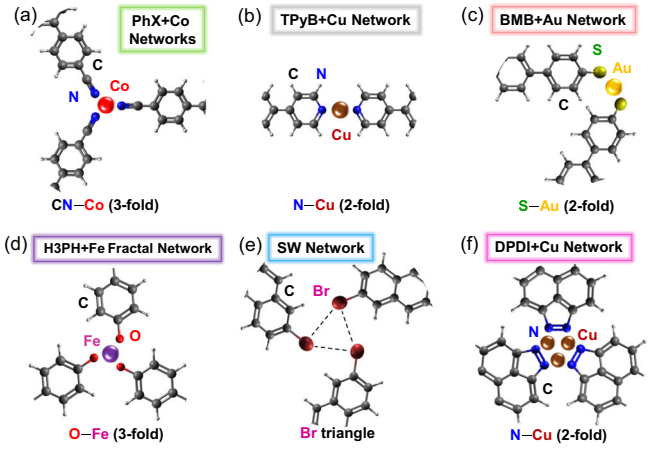

FIG. 13. Schematic representation of exemplary metal-organic and halogen bonds underpinning the formation of extended molecular nanostructures on the smooth fcc(111) metal surfaces delineated in Fig. 12.

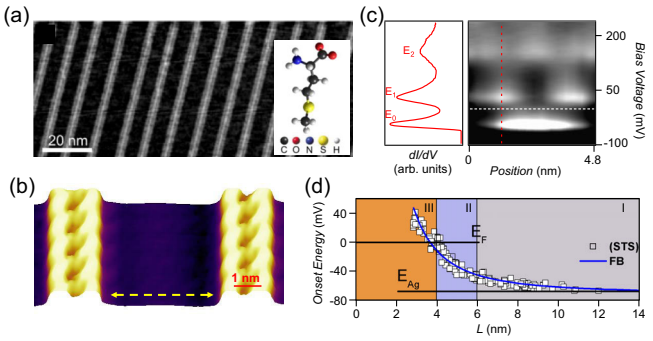

FIG. 14. One-dimensional nanograting created by zwitterionic self-assembly of *L*-methionine on Ag(111). (a) Topography overview of regularly spaced nanogratings. (b) High-resolution 3D perspective of a 4.8 nm wide quantum well. (c) Characteristic STS acquired perpendicular to the cavity that exhibits the first three 1D QWS resonances. (d) The energy of the first QWS resonance varies in an inverse quadratic way with the chain separation, as expected for a particle-in-a-box model. Adapted from Pennec *et al.*, 2007.

The 2DEG scattering can be exerted analogously by the rims of compact molecular islands. In particular, regular tetracyanoquinodimethane (TCNQ) species in periodic arrangement can discretize the electron momentum parallel to the island edge, whose effect is ascribed to the Bragg scattering from the periodic and corrugated 1D edge (Martín-Jiménez *et al.*, 2019).

As a drawback, supramolecular nanogratings (Barth *et al.*, 2000; Weckesser *et al.*, 2001) are difficult to control in terms of extended regularity and periodicity (Pennec *et al.*, 2007; Urgel, Vijayaraghavan *et al.*, 2016). This is due to the weakness of the long-range repulsive interactions mediating the grid formation of the self-assembled molecular twin chain constituents. Although surface reconstruction patterns and the like can be employed to guide such assemblies (Weckesser *et al.*, 2001; Clair *et al.*, 2005), highly regular coupled 1D quantum systems based on molecules require improved assembly procedures.

B. Organic nanoporous networks as QD arrays

Two-dimensional nanoporous networks frequently present well-defined arrays commensurate with the substrate and comprising atomically precise pores. We show here that within these nanocavities the substrate's 2DEG gets confined and follows the same scattering mechanisms as occur at the inorganic quantum corrals and nanoislands described in Fig. 7. In particular, the LDOS observed at the pores of nanoporous networks created using dicyano-poly(*p*-phenylene) molecules is discussed. The structural morphologies displayed by this molecular family depend on the cyano-aryl end group interaction and molecular backbone length. In the case of the dicyano-hexa(*p*-phenylene) (Ph6) molecules, self-assembly on Ag(111) affords several nanoporous structures featuring a common fourfold bonding motif (see Fig. 15) (Klappenberger *et al.*, 2009; Chung *et al.*, 2011; Krenner *et al.*, 2013), which allows for a straightforward comparative assessment. When classified by the pore shape, three networks

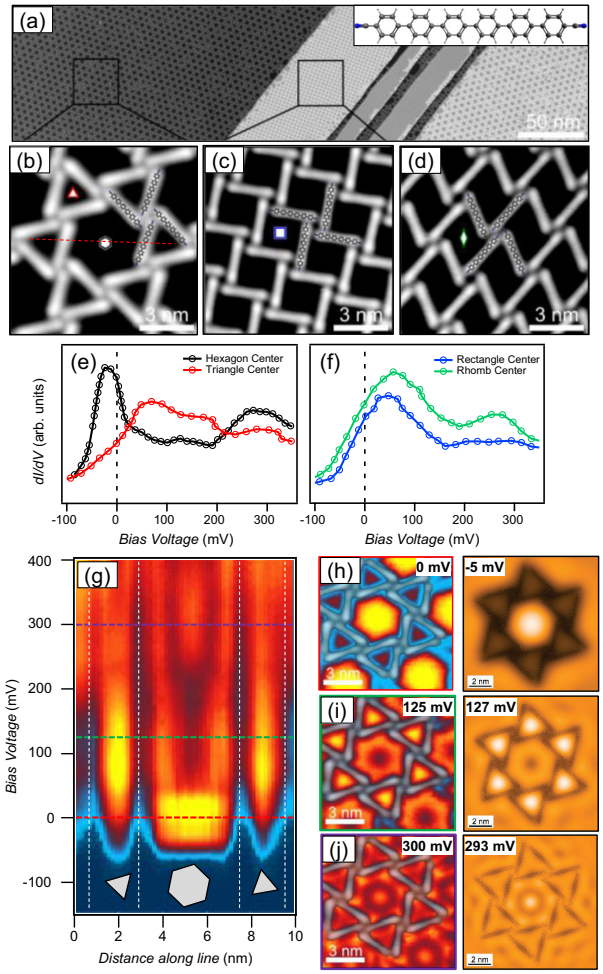

FIG. 15. Example of polymorphic organic nanoporous networks acting as self-assembled interwoven quantum corral structures. (a) STM image overview showing the coexistence of several network geometries generated by dicyano-hexa(*p*-phenylene) (Ph6) molecules after deposition on Ag(111). The pure organic assemblies form (b) kagome, (c) rectangular, and (d) rhombic structures. (e),(f) Differential conductance spectra recorded at the pore centers found in (b)–(d). (g) dI/dV linescan acquired along the dashed line across the pore marked in the STM image shown in (b). Up to three (two) confined states can be distinguished at the quasihexagonal (triangular) pore. (h)–(j) Conductance maps (left images) and EBEM simulated LDOS maps (right images) at the indicated energies showing the spatial distribution of the 2DEG confined states. Adapted from Klappenberger *et al.*, 2009.

are identified: kagome (with triangular and quasihexagonal pores), rectangular, and rhombic [Figs. 15(b)–15(d)]. These polymorphic nanoporous networks are commensurate with the substrate and display two chiral orientations for each structure. The conductance spectra at the center of these pores contain several peaks with maxima at different energies; see Figs. 15(e) and 15(f)]. At first glance, these spectra seem unrelated to the highly featured quantum corral line shapes displayed in Fig. 7. However, an order of magnitude difference exists between the area defined by the hexagonal nanoisland in Fig. 7(c) and the quasihexagon in Fig. 15(b). The severe pore size reduction significantly separates the resonance peaks of these networks when compared to the atom corrals. Consequently, only the lowest resonances can be accessed within the energy window probed (Li *et al.*, 1998). In the STS spectra of Figs. 15(e) and 15(f), the first peak's energy position is, as expected, dominated mainly by the pore size: ~ -20 meV for the quasihexagonal (largest), ~50 meV for the rectangular, ~60 meV for the rhombic, and ~80 meV for the triangular (smallest) pores. To study the impact that molecular nanopore size and shape have on the quantum confinement, a series of conductance spectra and maps were acquired for the kagome lattice. The linescan in Fig. 15(g) and the conductance maps in Figs. 15(h)–15(j) show the energy and spatial variations of the LDOS associated with the different pore shapes (Klappenberger *et al.*, 2009; Krenner *et al.*, 2013). For the quasihexagon, the lowest confined state ($n = 1$) exhibits a dome shape (without nodes) [Fig. 15(h)], while the second confined state ($n = 2$) features one node with roughly toroidal shape [Fig. 15(i)]. Note that at that energy the triangular pores now exhibit their first confined state. As expected, the third state ($n = 3$) of the quasihexagons displays a sombrero-shaped structure with two nodes [Fig. 15(j)] (Klappenberger *et al.*, 2009; Krenner *et al.*, 2013). The geometric chirality signatures of the pores are recognized in the confined state LDOS distribution. At the highest energy a threefold symmetry in the triangular nanocavities can be found, which is indicative of energy proximate to their $n = 2$ confined state (Schouteden and Van Haesendonck, 2012).

A modeling using EBEM is helpful for a deeper understanding of the 2DEG confinement resonances. EBEM can accurately reproduce the electron confinement effects in molecular nanostructures by parametrizing the 2DEG (Klappenberger *et al.*, 2009, 2011) and generally considers the molecules as repulsive barriers. The performed simulations reproduce the experimental confinement features [Figs. 15(h)–15(j)] using a molecular potential of $V_{\mathrm{mol}} = 500$ meV; see Table II. The fact that these peaks bear an intrinsic broadening allows a certain energy range for the visualization of the confined states in the conductance maps and also leads to a mixing of eigenstates (Klappenberger *et al.*, 2011; Wang *et al.*, 2018). Contrary to the polymorphic structure of Ph6, the self-assembly of dicyano-penta(*p*-phenylene) (Ph5) or other shorter species (ter- or quater-phenylene) on Ag(111) provides long-range ordered chiral kagome lattices (Schlickum *et al.*, 2008) or other homogeneous structures (Klyatskaya *et al.*, 2011). In a similar fashion, the on-surface synthesis and assembly of circumcoronene on Cu(111) has recently been used to create an extended chiral electronic kagome-honeycomb lattice where the 2DEG is confined into two emergent electronic flat bands (Telychko *et al.*, 2021). Moreover, other organic-based corrals, in the form of molecular nanohoops, honeycombene oligophenylene macrocycles, molecular quantum corrals, and porous COFs, show similar 2DEG confinement capabilities (Wang *et al.*, 2013; Taber *et al.*, 2016; Chen *et al.*, 2017; Hao *et al.*, 2019; Peng *et al.*, 2021). Associated with this, on-surface synthesized organic nanowires and rings can display intramolecular electronic confinement (different from the 2DEG), such that the nanorings act as whispering

TABLE II. Summary of the scattering potentials and surface-state renormalization used in literature for the EBEM or EPWE simulations of different organic (O) and metal-organic (MO) networks discussed here.

Network type (O or MO)	Substrate	V_{molecule} (meV)	V_{adatom} (meV)	E_0 (eV)	m^*/m_e	Technique	Reference
2H-TPP trenches (O)	Ag(111)	300	⋯	−0.065	0.42	STS	Seufert *et al.* (2013)
Ph6 kagome (O)	Ag(111)	500	⋯	−0.065	0.42	STS	Klappenberger *et al.* (2009)
Ph4+Co/Ph6+Co (MO)	Ag(111)	500	−50	−0.065	0.42	STS	Klappenberger *et al.* (2011)
SW or DW (O)	Ag(111)	140	⋯	−0.065	0.49/0.54	STS or ARPES	Piquero-Zulaica *et al.* (2017)
Multiporous network (O)	Ag(111)	255	⋯	−0.070	0.39	STS	Kawai *et al.* (2021)
Tessellated networks (MO)	Ag(111)	800	800	−0.070	0.455	STS	Hu *et al.* (2022)
Ph3 + Co/Ph6 + Co (MO)	Au(111)	250	50	−0.52/ − 0.56	0.22/0.21	STS or ARPES	Piquero-Zulaica *et al.* (2019b)
BMB + Au (MO)	Au(111)	600	600	−0.48	0.26	STS	Colazzo *et al.* (2019)
3deh-DPDI + Cu (MO)	Cu(111)	390	390	−0.44	0.49	STS or ARPES	Piquero-Zulaica *et al.* (2019a)
TPyB + Cu (MO)	Cu(111)	250	50	−0.53	0.41	STS or ARPES	Piquero-Zulaica *et al.* (2019c)

gallery mode resonators for the oligomeric states (Reecht *et al.*, 2013).

C. Metal-organic QD arrays

A metal-directed assembly provides an additional control knob on nanoarchitectures (Schlickum *et al.*, 2007; Kühne *et al.*, 2009; Pacchioni, Pivetta, and Brune, 2015) while simultaneously enabling the formation of robust metal-organic networks. In particular, when Co atoms are codeposited with dicyano-poly(*p*-phenylene) molecules on Ag(111), the formation of crystal quality, monodomain, hexagonal nanoporous networks occurs (Schlickum *et al.*, 2007; Kühne *et al.*, 2009). As shown in Figs. 16(a)–16(c), these metal-organic coordination networks (MOCNs) require a 3:2 stoichiometry of dicyano-poly(*p*-phenylene) molecules with Co atoms (Klappenberger *et al.*, 2011). Isostructural CN–Co coordination nodes at specific substrate positions prevail for both dicyano-tetra(*p*-phenylene) (Ph4) and Ph6 (Schlickum *et al.*, 2007); see Fig. 13(a). Thus, homothetic (i.e., scalable) geometries are available, serving as ideal systems for studying the nanopore size dependence on the 2DEG confinement.

As the pores are regular in shape and size, the overall 2DEG confinement prevails throughout the surface. This is confirmed by the conductance maps for Ph6 + Co and Ph4 + Co, shown in Figs. 16(d)–16(g), and their corresponding STS acquired at the hexagonal pore centers [Fig. 16(h)]. The dI/dV spectra display the first confined states ($n = 1$) at ~ -6 and ∼15 meV for the Ph6 + Co and Ph4 + Co networks, respectively. As expected, these are visualized as domes when conductance maps are acquired close to these energies. The second confined state ($n = 2$), visualized as a torus in the conductance maps, cannot be clearly distinguished in STS in the center, since it coincides with a node at the pore center. One must reach the third ($n = 4$) resonance to observe a conspicuous peak again at the pore center.

Overall, the conductance maps of Figs. 16(d)–16(g) exhibit the same spatial LDOS distribution throughout these two networks, except for the energy shift (and a slight broadening) dictated by the different pore size. Indeed, the energy positions of these resonances become identical when scaled using a reduction factor $R = 1.74$ for the Ph4 + Co, which is close to the nanopore area ratio ($R^* = 1.83$) (Klappenberger *et al.*, 2011).

These networks scatter the Ag(111) 2DEG through the finite hexagonal barriers that have been simulated using EBEM (Klappenberger *et al.*, 2011). The calculations suggested a heterogeneous scattering potential landscape whereby molecules and adatoms scatter electrons differently; see Table II. A successful ansatz implies that the metal centers behave as slightly attractive regions ($V_{\text{Co}} = -50$ meV), whereas the molecules are strongly repulsive ($V_{\text{mol}} = 500$ meV) for the substrate 2DEG. However, the assignment for the coordination nodes is debatable since an attractive potential should host bound states (Madhavan *et al.*, 2001; Olsson *et al.*, 2004; Silly *et al.*, 2004; Limot *et al.*, 2005; Liu *et al.*, 2006), which thus far have been elusive in nanoporous networks (Klappenberger *et al.*, 2011; Piquero-Zulaica *et al.*, 2019b). By contrast, chemisorbed close-packed arrays of Au-TCNQ and Mn-TCNQ can display such states at lower energies than the surface-state onsets (Faraggi *et al.*, 2012), although the absence of open pores prevents any expression of confined states. The scattering potential of the coordination nodes requires in-depth scrutiny, as further discussed in Sec. V.C.

Other pore shapes are also feasible by metal-directed assembly protocols. A prominent example is the formation of a 2D triangular MOCN stabilized by Au-thiolate bonds; see Fig. 13(c). It could be obtained simply via the deposition of 1,4-bis(4-mercaptophenyl)benzene (BMB) on the Au(111) surface, providing intrinsic adatoms that engage in the formation of the coordination superlattice (Colazzo *et al.*, 2019). The Au_3BMB_3 units forming this array consist of embedded triangular nanopores that strongly confine the Au(111) surface state [Fig. 17(a)]. The significant peak shift of ∼700 mV is well reproduced by EBEM, although for this system it required one of the largest repulsive potentials reported for nanoporous networks using this semiempirical method ($V_{\text{mol}} = 600$ meV); see Table II.

Combined triangular units can be even more interesting when Sierpiński lattices are generated using self-assembly

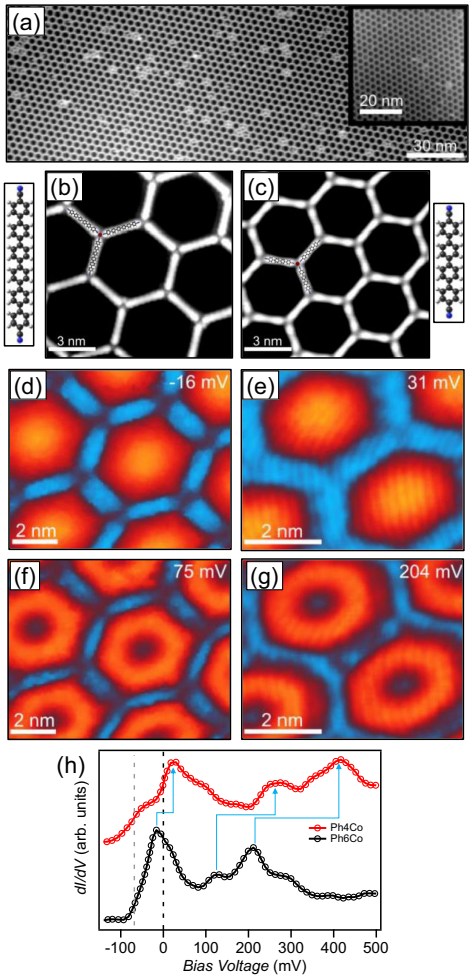

FIG. 16. Tunable 2DEG confinement by metal-organic coordination of dicyano-poly(*p*-phenylene) molecules. (a) Image overview of a metal-organic Ph6 + Co hexagonal network obtained on Ag(111). Inset: homothetic scalable network using shorter molecules (Ph4 + Co) that is also grown on Ag(111). (b), (c) High-resolution topographs of these networks that include their corresponding molecular structures. (d),(f) Conductance maps of the first ($n = 1$) and second ($n = 2$) confined states in the Ph6 + Co network. (e),(g) The same information for the Ph4 + Co array. (h) Conductance spectra at the center of both hexagonal pores, which exhibit a larger energy shift as the pore size is reduced. Adapted from Klappenberger *et al.*, 2011.

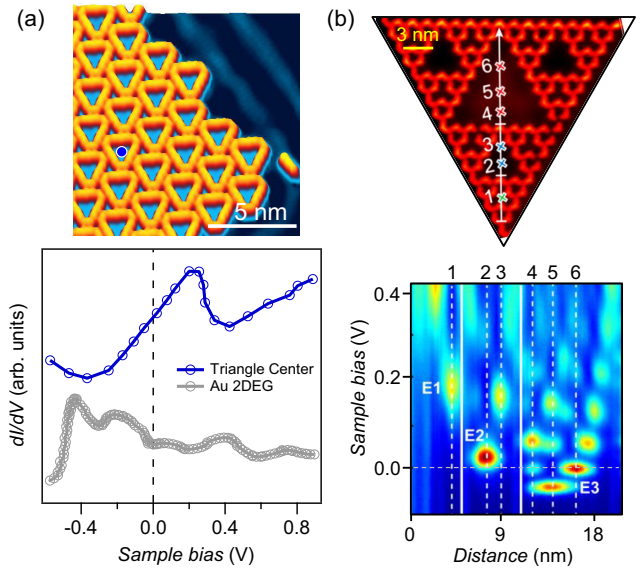

FIG. 17. Confinement properties of a triangular lattice and Sierpiński triangle fractals generated by metal-directed assembly. (a) STM topograph of an array of condensed triangular Au_3BMB_3 complexes. STS data acquired at the triangular nanopore center (marked by a dot) show a resonance strongly shifted with respect to the pristine Au 2DEG. Adapted from Colazzo *et al.*, 2019. (b) STM image of self-assembled H3PH-Fe Sierpiński triangles and the corresponding spatially resolved STS map acquired along the vertical arrow. Adapted from Wang *et al.*, 2018.

methods. In particular, the codeposition of 4, 4″-dihydroxy-1, 1′, 3′, 1″-terphenyl (H3PH) and Fe atoms on Ag(111) followed by a mild annealing to 380 K affords the fractal structures shown in Fig. 17(b) (Wang *et al.*, 2018, 2019); see the bonding motif in Fig. 13(d). Contrary to the previously discussed CO manipulated counterpart that is depicted in Fig. 9(c), here the Ag surface state is confined at the scalable triangular nanopores, which presents an inverse energy shift dependency with respect to the enclosed area. Other interesting network geometries in the form of demiregular lattices, Kepler tilings, and quasicrystals giving rise to related complex confinement capabilities have been recently achieved (Écija *et al.*, 2013; Urgel, Écija *et al.*, 2016; Yan *et al.*, 2017; Piquero-Zulaica *et al.*, 2019c; Hu *et al.*, 2022).

V. QD ARRAYS INDUCING WELL-DEFINED BAND STRUCTURES

Since molecular superlattices with leaky barriers and well-defined nanopores can homogeneously carpet the surface with minute defect concentrations, a coherent electronic signal stemming from coupled QDs can be measured using space-averaging techniques such as ARPES. In the following we visit a series of studies highlighting the formation of genuine band structures that can be engineered by the choice of the employed molecular building blocks.

A. Emergence of dispersive bands

The first band structure from a QD array was measured for the Cu(111) surface state confined by the 4,9-diaminoperylene quinone-3,10-diimine (DPDI) + Cu extended network (Lobo-Checa *et al.*, 2009). This hexagonal metal-organic nanoporous network is formed after thermal dehydrogenation of DPDI molecules on the metal surface. The threefold symmetric array is characterized by a unit cell composed of three molecules and six Cu adatoms [see Fig. 13(f)] with a periodicity of 2.55 nm (Matena *et al.*, 2014; Shchyrba *et al.*, 2014; Piquero-Zulaica, Nowakowska *et al.*, 2017; Piquero-Zulaica *et al.*, 2019a) [see Figs. 18(a) and 18(c)], which was also used to host guest species (such as octaethylporphyrins and C_{60}) within the voids (Stöhr *et al.*, 2007).

As shown by the conductance map and STS curves in Figs. 18(b) and 18(d), this molecular network confines the

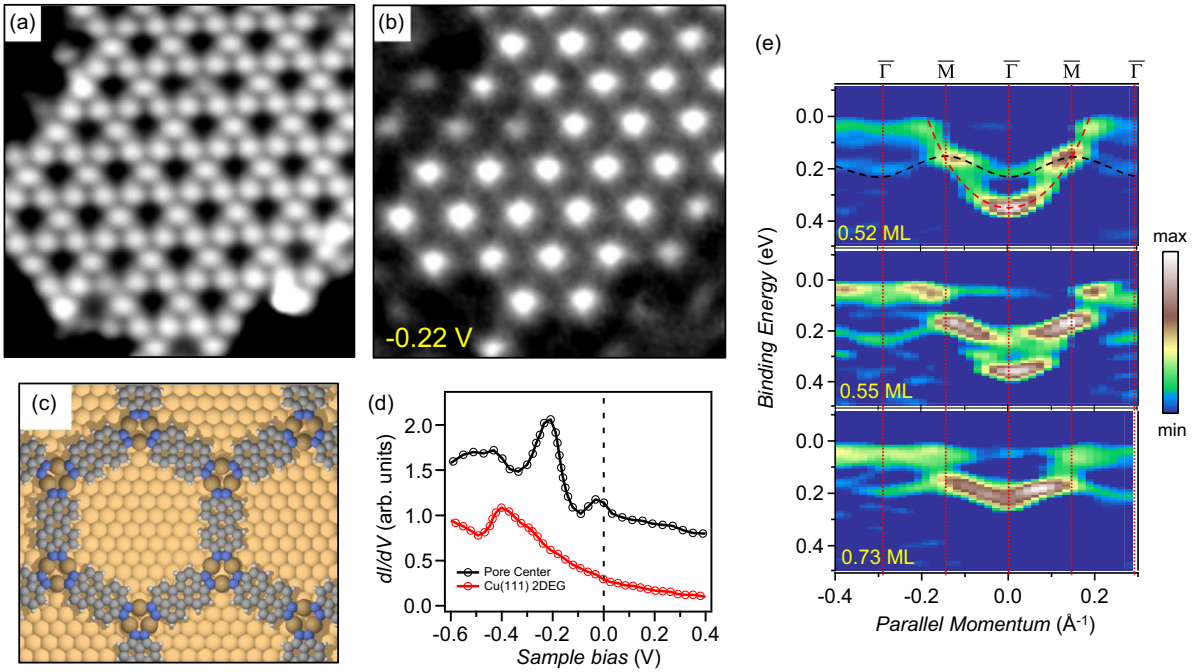

FIG. 18. Zero-dimensional electron confinement and emergence of a 2D band structure by the 3deh-DPDI-based metal-organic coordination network on Cu(111). (a),(b) STM image (13.6×13.6 nm^2) of the hexagonal network and a simultaneously acquired conductance map at −0.22 V. At this energy the electrons are confined ($n = 1$ resonance) within the pores. (c) Structural model of the tri-metal-coordinated perilene-based nanoporous network. (d) STS spectra measured at the center of a hexagonal pore (black line) and pristine Cu [red (gray) line]. (e) Band structure of the extended nanoporous network as the surface is progressively covered (from top to bottom) with the molecular array. The cosine-shaped black dashed line around 0.2 eV in the top panel (lowest coverage) marks the first network confined band, whereas the parabolic red (light gray) dashed line marks the pristine surface state stemming from the network-free regions. As the coverage increases, the emission from the pristine surface state gradually disappears while the band originating from the coupled QDs gains intensity, until only the shallow dispersive network band remains (bottom panel). Note that the energy of this band matches (after normalization of the measurement temperature) the dominant STS peak position in (d), which is related to the $n = 1$ confined state displayed in (b). Adapted from Lobo-Checa *et al.*, 2009, and Matena *et al.*, 2014.

Cu(111) surface-state electrons within its pores. The first confined state ($n = 1$) is found at ~ -0.22 V and the second ($n = 2$) at ~ -0.08 V. The conductance map at $n = 1$ shows the characteristic domelike shape centered at the network pores, such that each pore acts as a single QD. However, the width of the STS peak suggests the possibility of coupling between neighboring pores, fulfilling the previously described extended scenario depicted in Fig. 11(d).

To check for the existence of a band, ARPES measurements were performed close to the Fermi energy with the network covering a significant part of the surface [Fig. 18(e)]. This metallo-supramolecular array is ideal because it is monodomain, commensurate with the substrate (10×10), affords large domains (laterally exceeding 50 nm), and homogeneously covers the surface with a relatively small amount of defects. Consequently, the DPDI + Cu network can be conceived as a periodic superlattice of QDs, where the Cu(111) surface state (the 2DEG) is confined by the building units (molecules and Cu adatoms) that strongly modify the initial surface potential landscape. The ARPES signal is displayed in Fig. 18(e) and exhibits the progressive extinction of the 2DEG parabolic band related to the pristine surface state, which is replaced by a cosine-shaped band centered at ~ -0.2 eV as the network fills the surface (note that the nanoporous network covers the surface completely at ~0.73 ML). Therefore, the 2DEG is engineered by the network into new electronic bands whose dispersion relates to the QD coupling strength and pore size. The fundamental energy and bandwidth match the STS peak observed in Fig. 18(d) and has been proven to originate from the pristine substrate's Shockley state (Piquero-Zulaica, Nowakowska *et al.*, 2017).

This extraordinary band structure is the natural extension of the artificial 2D lattices and quantum corrals without the requirement of molecular manipulation. The modeling of the potential landscape generated by this DPDI + Cu network (Kepčija *et al.*, 2015; Piquero-Zulaica *et al.*, 2019a) was realized using the semiempirical EPWE method, which uses linear combinations of plane waves (the 2DEG) that are scattered by the potential barriers in an infinite periodic lattice (mimicking the metal-organic network). It is most accurate whenever the simulation starts with a realistic scattering geometry and different scattering potentials are assigned to molecules and adatoms to account for the 2DEG electron barriers (Piquero-Zulaica *et al.*, 2019a, 2019b). The combination of experimental datasets (STS and ARPES) as input for these semiempirical simulations allows one to capture the intricacies of the scattering potential landscape generated by these networks and to establish systematic modeling procedures; see Sec. V.D for more details.

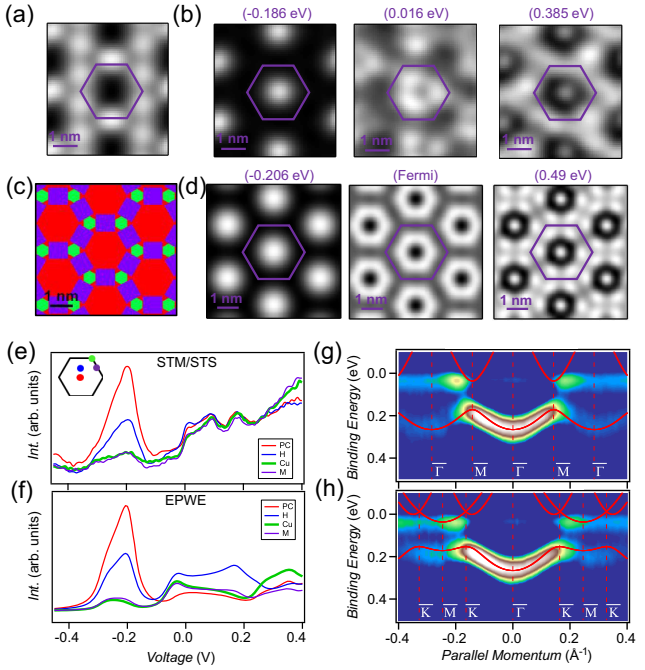

FIG. 19. Comparison between experimental datasets (LDOS and electronic band structures) with the EPWE semiempirical simulations of the DPDI + Cu network. (a) STM image and (b) three constant height conductance maps at selected energies close to the first, second, and fourth confinement resonances. (c) Potential landscape constructed for the EPWE simulations. It consists of three different regions: Cu substrate [red (gray) hexagons], molecules [purple (dark gray) rectangles], and metal centers [green (light gray) hexagons]. The potential values given to molecules and adatoms are provided in Table II. (d) Calculated LDOS at the indicated energies with the scattering geometry in (c) showing similar spatial distributions as the upper experimental cases. (e) dI/dV spectra acquired at different unit cell positions (see inset) and (f) the corresponding EPWE simulated LDOSs. (g),(h) Color (gray scale) plots of the experimental band structure (second derivative of the ARPES intensity) for the two high-symmetry directions (g) $\overline{\Gamma M}$ and (h) $\overline{\Gamma K}$ and simulated EPWE bands superimposed as solid thin lines. The high quality of the network allows one to observe faint replica bands in adjoining Brillouin zones that are matched by the calculations. Adapted from Piquero-Zulaica *et al.*, 2019a.

A comparison between modeling and experiments for the DPDI + Cu network is shown in Fig. 19. The agreement between STM or STS and ARPES datasets with the EPWE simulations (LDOS and band structure) is noteworthy. The potential landscape [Fig. 19(c)] was constructed using the structural model of the network (Matena *et al.*, 2014) that emulates the experimental STM [Fig. 19(a)] and NCAFM images (Kawai *et al.*, 2016). It was found that the scattering at the molecular backbones is homogeneous and similar to the coordination nodes ($V_{\mathrm{DPDI}} = V_{\mathrm{Cu}} = 390$ meV) (Piquero-Zulaica *et al.*, 2019a). The scattering character of the metal centers is repulsive in the DPDI + Cu network, which agrees with other atom-based 2DEG confining entities, such as step edges or dislocation networks (Mugarza *et al.*, 2006; Malterre *et al.*, 2011). To match the experimental datasets, the pristine surface state must be renormalized. In other words, the network's presence modifies the 2DEG parabolic dispersion, affecting both the effective mass (m^*) and the reference energy (E_0, also referred to as the onset energy). The potential values and 2DEG renormalization used for the simulations are collected in Table II. This renormalization process of 2DEGs becomes evident for most nanoporous MOCNs studied thus far with photoemission (Piquero-Zulaica *et al.*, 2017, 2019a, 2019b, 2019c), and its underlying physics are explained in more detail in Secs. V.B–V.D.

B. Regulating QD crosstalk through the barrier width

The network barriers condition the degree to which individual QDs couple with each other and ultimately define the energy position and shape of the electronic bands. Hence, the control over the potential barriers between neighboring QDs turns out to be essential to engineering the 2DEGs, as they alter the crosstalk (interaction) between their confining units.

Experimentally it is now possible to tune the confinement and intercoupling properties of individual QDs by engineering the network barrier widths without affecting the pore size (Piquero-Zulaica *et al.*, 2017). This was achieved in molecular networks using the halogen bond versatility (Kawai *et al.*, 2015; Shang *et al.*, 2015; Han *et al.*, 2017; Mukherjee *et al.*, 2019) without the need of metal coordination. In particular, two haloaromatic compounds, 3,9-dibromodinaphtho[2,3-b:2′, 3′-d]thiophene (Br-DNT) and 3,9-dibromodinaphtho [2,3-b:2′, 3′-d]furan (Br-DNF), that differ in just a single atom at their center (S versus O) generate the two supramolecular networks shown in Fig. 20 on Ag(111) and on thin Ag MLs grown on Au(111). The extended organic arrays enclose identical pore areas separated by either one [single-wall (SW)] or two [double-wall (DW)] molecules. The condensation of Br-DNT into a nanoporous network happens solely through trigonal halogen bonding [see Fig. 13(e)], whereas in Br-DNF the furan group electronegativity introduces O–Br bonds, increasing the interaction complexity and leading to the double-rim formation (Piquero-Zulaica *et al.*, 2017).

The LDOS at the pore centers [Fig. 20(c)] produces evidence of the quantum confinement line shape. However, when the peak locations are inspected, the first resonances ($n = 1$) unexpectedly seem energy inverted when simply assuming stronger confinement for the wider barrier case (DW). The energy shift, in particular, is visibly larger for the SW case than the DW one; note the inverted arrow positions marking the peak maxima. To understand this behavior and resolve the QD arrays' band structure, ARPES measurements were performed on both networks. Figures 20(e) and 20(f) display weakly dispersive cosine-shaped bands typical of QD arrays. As expected for confined 2DEG electrons, their fundamental energy (onset of the band) shifts to higher energy and deviates from the initial parabolic dispersion; see Figs. 20(d)–20(f). In addition, evidencing a stronger confinement, the DW onset is farther from the 2DEG reference than the SW array.

EPWE model calculations of these two arrays were carried out to gain further insight. Simultaneously matching the STS and band structure was possible using an effective potential

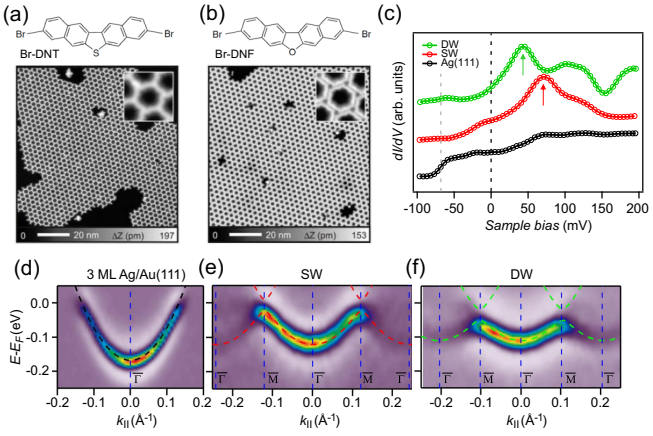

FIG. 20. QD band engineering by tunable barrier widths: self-assembled single-wall (SW) and double-wall (DW) QD arrays showing different interpore couplings of confined quantum states. (a) Large-scale STM topographies for the SW network generated with Br-DNT and (b) the DW network with Br-DNF. Insets: enlarged arrangement for each network. (c) STS at the pore center of the SW and DW networks compared to the Ag substrate's typical stepwise DOS increase. (d)–(f) QD band structure of the $n = 1$ confined state induced by the SW and DW networks on Ag (3 ML)/Au(111) along $\overline{\Gamma M}$. The match with the EPWE calculated electronic bands overlaid as dashed lines is excellent. From these experiments it was concluded that an analysis of STS and confinement trends should not be limited to an inspection of peak shifts. Adapted from Piquero-Zulaica *et al.*, 2017.

$V_{\mathrm{mol}} = 140$ meV; see Table II. This provided evidence that both experimental techniques must be probing the same electronic states, but in a different way. The origin of this discrepancy can be understood with the knowledge gained in the previously described molecular trenches (Fig. 11): STM is more sensitive to the antibonding states that transform into the top of the coupled QD band. Indeed, the STS peak maxima coincide with the energy of the $\bar{M}$ points in the ARPES datasets. Contrarily, the band onset (fundamental energy) found by ARPES shows up as a weak shoulder in the STS at the pore center. This renders the LDOS peak line shapes asymmetric with maxima displaced toward the top of the band in periodic QD arrays.

In essence, the 2DEG confinement strength of DW exceeds that of SW networks, showing a reduced bandwidth in ARPES and peak width in STS compared to the SW. This decrease in the bandwidth with identical potential scattering barriers ($V_{\mathrm{mol}} = 140$ meV) relates to a lower interpore coupling imposed by a wider set of barriers (Seufert *et al.*, 2013; Piquero-Zulaica *et al.*, 2017), which translates into a reduction of the electron wave function overlap with QD separation. To properly understand the electron confinement phenomena in these QD arrays, complementary STM or STS and ARPES experimental datasets are needed. The EPWE simulations can then determine effective scattering potential barriers that the surface electrons experience. This allows the nature of the intercoupling processes to be captured and the 2DEG renormalization occurring through the presence of the network on the surface induced by overlayer-substrate interactions to be quantified (Piquero-Zulaica *et al.*, 2019a).

C. Role of coordination nodes in 2DEG renormalization and electron transmission

The next logical step is to engineer the coupled QD band structures by modifying the pore size while maintaining fixed potential barriers. Ideal candidates for such studies are the MOCNs generated using dicyano-poly(*p*-phenylene) molecules (Schlickum *et al.*, 2007; Kühne *et al.*, 2009; Klappenberger *et al.*, 2011), as previously discussed and shown in Fig. 16. These homothetic Co-coordinated networks cannot be properly studied with ARPES if they are grown on Ag(111), since the 2DEG onset is too close to the Fermi energy; see Fig. 2. For that matter these MOCNs were generated on the Au(111) surface, where arrangements isostructural to those reported on Ag(111) evolve (Piquero-Zulaica *et al.*, 2019b).

Figures 21(a) and 21(b) show the Ph3 + Co and Ph6 + Co formed honeycomb networks on Au(111) that feature pore areas of 8 and 24 nm^2, respectively; see the bonding motif in Fig. 13(a). The measured band structures show weak umklapps (replicas) of the main signal with modulated gaps [Figs. 21(c) and 21(d)]. The STS and conductance maps [Figs. 21(j)–21(l)] confirm 2DEG confinement at the pores, agreeing with the networks generated on Ag(111); see Fig. 16. Moreover, there is clear evidence of a gradual downshift of the band bottom as the pore size is reduced [$\Delta E_{\mathrm{Ph6+Co}} = -40$ meV and $\Delta E_{\mathrm{Ph3+Co}} = -100$ meV with respect to the Au 2DEG; see Fig. 21(i)]. This is at variance with the expected upward shift found for all other coupled QD bands and inorganic scatterers shown before (Lobo-Checa *et al.*, 2009; Piquero-Zulaica *et al.*, 2017, 2019a).

EPWE simulations were employed once again to unravel the potential landscapes generated by the molecular networks (Piquero-Zulaica *et al.*, 2019b). The STS and ARPES datasets were matched while assuming strong repulsive scattering potentials at the molecular sites ($V_{\mathrm{mol}} = 250$ meV) and weaker ones for the adatoms ($V_{\mathrm{Co}} = 50$ meV). A severe 2DEG renormalization was required to account for the downshifts of the band bottom ($E_0^{\mathrm{Ph3+Co}} = -0.52$ eV and $E_0^{\mathrm{Ph6+Co}} = -0.56$ eV compared to the Au 2DEG $E_0^{\mathrm{Au}} = -0.48$ eV; see Table II).

To understand such strong 2DEG modification, *ab initio* DFT calculations were carried out. In these calculations the interaction between a Co lattice (defined by the MOCN) and the Au(111) substrate was investigated, whereby the magnitude of the 2DEG downshift can be directly related to the concentration of isolated Co adatoms existing on the surface. However, the molecular network presence interferes since it ultimately defines the interaction strength of the adatom array with the substrate (Co-Au hybridization) (Schlickum *et al.*, 2007; Piquero-Zulaica *et al.*, 2019b). This applies to single-atom-coordinated MOCNs since the adsorption height of the adatoms increases due to the coordination with the molecules, which effectively reduces their interaction with the substrate. As shown next, downward energy renormalization effects occur systematically in other single-atom-coordinated MOCNs and substrates but were not previously fully recognized, since no complementary photoemission data for determining the 2DEG onset were available (Piquero-Zulaica *et al.*, 2019b).

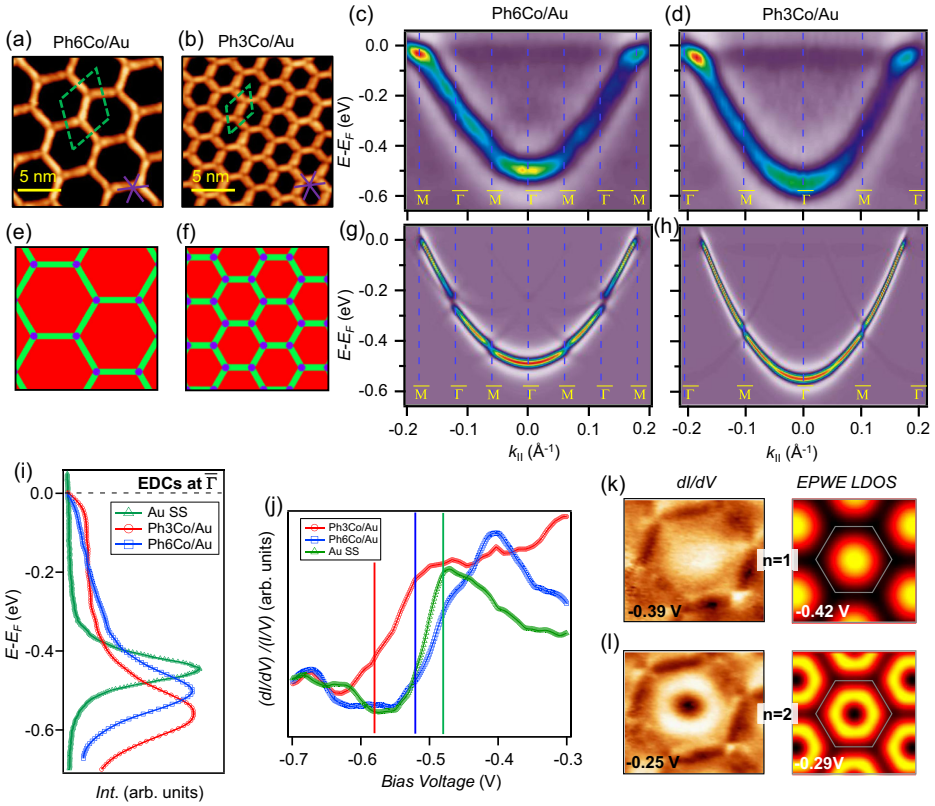

FIG. 21. Band structure engineering with tunable pore sizes: 2DEG confinement bands of dicyano-poly(*p*-phenylene) metal-organic coordination networks grown on Au(111). STM topographies of single-domain Co-coordinated QD arrays using (a) Ph6 and (b) dicyano terphenyl (Ph3). ARPES spectral density (second derivative) of (c) Ph6 + Co and (d) Ph3 + Co networks. (e), (f) Corresponding 2D potential geometries used for the EPWE modelization [molecules depicted as long green (light gray) rectangles, Co atoms as interconnecting purple (dark gray) dots and large red (gray) hexagons for cavity regions]. (g),(h) Simulated ARPES bands obtained by EPWE. Note that the band structure exhibits downward shifts of the band bottom and gap openings at the superstructure symmetry points compared to the pristine Au(111) surface state. Matching the experimental data requires a significant modification of the 2DEG energy reference. (i) Normal emission EDCs display the gradual downshift of the fundamental energy as the pore size is reduced, which is also observed in (j) as an enlargement of the conductance spectra close to the pristine gold surface state (Au SS) onset. (k),(l) Experimental (left images) and EPWE simulated (right images) conductance maps of the $n = 1$ and 2 confined resonances. Adapted from Piquero-Zulaica *et al.*, 2019b.

The confining strength of the metal centers in dicyano-poly(*p*-phenylene)–based MOCNs turns out to be significantly weaker than that of the molecules. This property can be further used to engineer the coupled QD band structure by increasing the crosstalk between neighboring pores. To this end, the electronic structure of the Cu-coordinated network [1,3,5-tri(4-pyridyl)-benzene (TPyB) + Cu] was investigated (Piquero-Zulaica *et al.*, 2019c); see Fig. 22. This extended, monodomain honeycomb network is generated from TPyB molecules deposited on Cu(111), where the substrate provides native Cu centers bridging the TPyB pyridyl groups through a twofold coordination (Wang *et al.*, 2013); see Fig. 13(b).

The band structure from the TPyB + Cu MOCN displays a downshift of −70 meV at the $\bar{\Gamma}$ point with respect to the pristine Cu 2DEG [Figs. 22(b)–22(e)]. The same scenario applies here as for the previously discussed Ph3 + Co and Ph6 + Co networks (Piquero-Zulaica *et al.*, 2019b) and for 2,4,6-tri(4-pyridyl)-1,3,5-triazine (T4PT) + Cu MOCN (Zhou *et al.*, 2020), in relation to a single adatom array interacting with the 2DEG. Note, however, that such a downshift is not a specific property of hexagonal networks, since it is also observed in demiregular networks (Piquero-Zulaica *et al.*, 2019c). The replica bands (umklapps) and small energy gaps observed in ARPES indicate weak 2DEG scattering from the network barriers; therefore, the electron confinement (visible when probing with STS) should be relatively weak within the pores. Thus, the electronic structure corresponds to strongly coupled QDs. Even though interesting robust half metallicity properties were also predicted in freestanding TPyB + Cu MOCNs (Zhang and Zhao, 2015), no such features appear for this and similar networks on Cu(111) (Piquero-Zulaica *et al.*, 2019c; Zhou *et al.*, 2020).

EPWE simulations based on the ARPES and STS datasets of the TPyB + Cu network again show a significant 2DEG renormalization to account for the 2DEG downshift and the existence of molecular potential barriers exceeding that of Cu atoms ($V_{\mathrm{TPyB}} = 250$ meV, $V_{\mathrm{Cu}} = 50$ meV; see Table II). These heterogeneous scattering potentials were corroborated by electrostatic potential (ESP) maps obtained from DFT calculations at the largest probability density of the Cu(111)

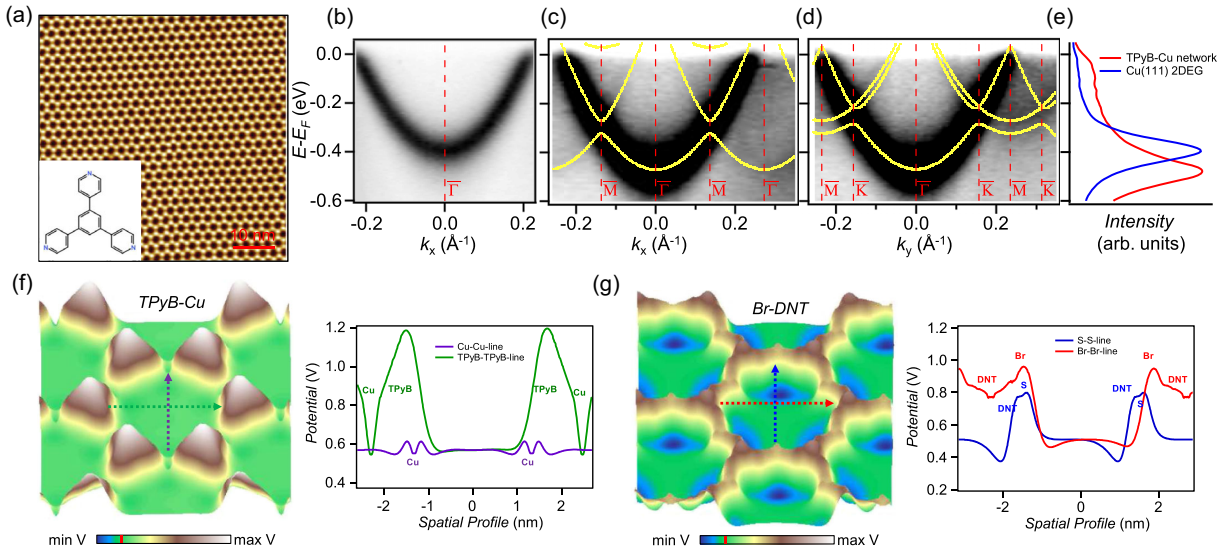

FIG. 22. Opening of electron transmission channels at confining QD arrays by the embedded metal centers. (a) STM image of the extended single-domain TPyB + Cu hexagonal QD array grown on Cu(111). Inset: Precursor molecule. (b) ARPES band structure of the pristine 2DEG and the QD array band of the TPyB + Cu network along the two high-symmetry directions: (c) $\overline{\Gamma M}$ and (d) $\overline{\Gamma K}$. (e) EDCs at normal emission ($\bar{\Gamma}$ point) that exhibit a −70 meV downshift of the confined state with respect to the pristine Cu 2DEG. (f),(g) Left images: 3D perspectives of the electrostatic potential map calculations for TPyB + Cu and Br-DNT networks. Right panels: their corresponding perpendicular potential line profiles. A significant potential difference is encountered between the adatoms with respect to the molecules. Adapted from Wang *et al.*, 2013, and Piquero-Zulaica *et al.*, 2019c.

surface-state region (Echenique *et al.*, 2004); see Fig. 22(f). The potential line profiles extracted from these calculations show that at the Cu coordination nodes the outer rim is weakly repulsive but quickly reverses its character toward its center. Since these Cu adatoms are located at network sides, they represent transmission channels between adjacent pores, yielding significant interdot coupling. This scenario does not occur in purely organic networks where the ESP maps typically display a rather homogeneous repulsive potential barrier landscape; see the Br-DNT and SW cases in Fig. 22(g). Accordingly, the QD intercoupling is hindered and larger energy gaps and band flattening occur in this SW network; see Fig. 20. Note that no downshift of the fundamental energy was found for purely supramolecular halogen-bonded nanoporous networks, thus substantiating an origin related to metal-organic coordination nodes.

D. Systematics of electron confinement and QD array bands using semiempirical simulations

As we have repeatedly seen, semiempirical models are regularly used to assess the complex scattering potential landscapes arising from these QD arrays. The analyzed organic and metal-organic systems require the use of the EBEM for finite structures (LDOS) and/or the EPWE for periodic arrays (Bloch-wave states) (García de Abajo *et al.*, 2010; Klappenberger *et al.*, 2011; Abd El-Fattah *et al.*, 2019). Note that EPWE developed as a predictive tool not only for single layer molecular networks on surfaces but also for atomic 2D materials (such as graphene and *h*-BN), GNRs, polymers, and single molecules (Piquero-Zulaica *et al.*, 2018; Abd El-Fattah *et al.*, 2019; Kher-Elden *et al.*, 2020; Ali *et al.*, 2021).

As semiempirical methods, EPWE and EBEM require several starting assumptions regarding the potential barrier strength, the repulsive-attractive condition, and the geometry. Initially, the modeling suffered from limitations and invoked sometimes unrealistically thin molecular backbones (resulting in excessively high potentials), attractive scattering potential regions at the metal sites, or enlarged effective masses compared to the pristine 2DEG. However, the methodology considerably improves when results from complementary experimental techniques are at hand (i.e., STM or STS, NCAFM, and ARPES). In such favorable cases the simulations can accurately reproduce the LDOS (local 2DEG confinement), the QD band structure (interpore coupling), and the 2DEG energy and mass renormalization. Several simulations based on the previously presented extended experimental datasets are summarized in Table II.

The simulation procedure follows an iterative fitting of different parameters that should systematically lead to a unique, physically meaningful solution. Figure 23 displays the recursive process to obtain the scattering potential landscapes based on experimental datasets of electron confining structures.

(1) *Setting of the scattering geometry.*—A model of the network (i.e., lattice constant and symmetry), as well as the molecular barrier size (L, w), is accurately extracted from STM and NCAFM images and refined by chemical structure modeling derived from DFT.
(2) *Definition of the 2DEG.*—Once the geometry is fixed, parameters from the pristine case are initially used based on their fundamental energy (E_0) and effective mass (m^*/m_e); see Table I.
(3) *Adjusting repulsive scattering barriers.*—These potential barriers are initially repulsive and are limited to

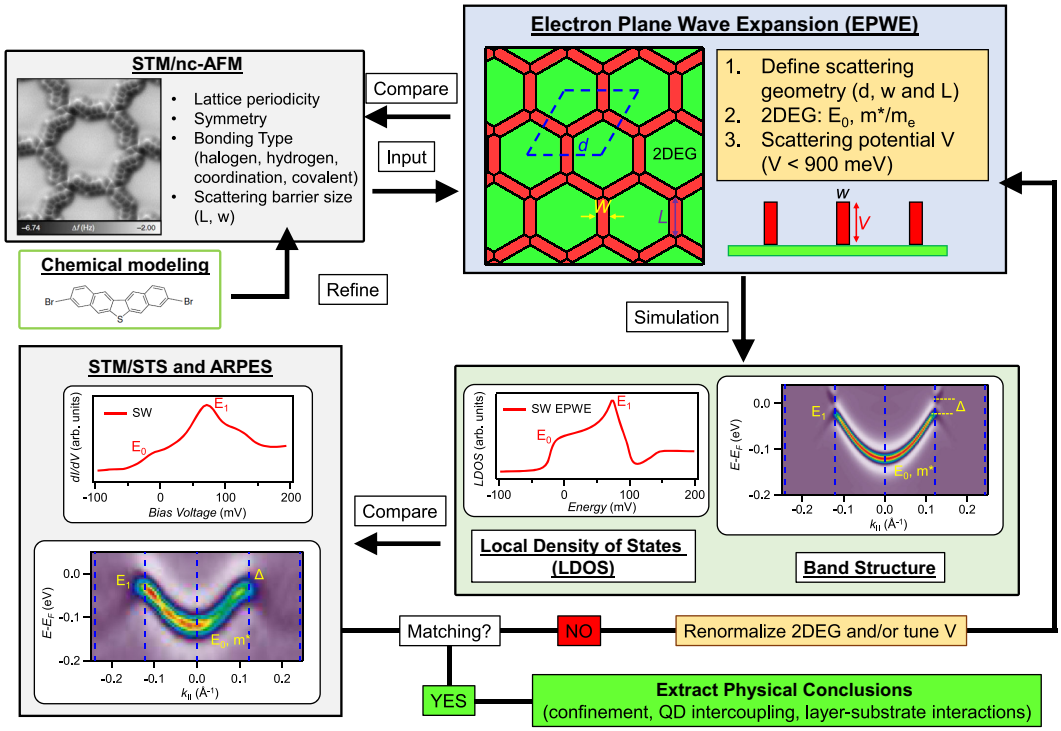

FIG. 23. Proposed iterative fitting procedure for semiempirical EPWE simulations based on surface sensitive experimental techniques (i.e., STM and STS, NCAFM, and ARPES). This systematic simulation process should lead to physically meaningful conclusions from any molecular confining structure grown on a substrate featuring a pristine surface 2DEG. Adapted from Piquero-Zulaica *et al.*, 2017.

$V_{\mathrm{mol}} < 900$ meV for carbon-based molecules. Note that this value depends on the molecular backbone size (related to step 1). Whenever metal adatoms are present in the network, a similar potential is assigned that will likely need reduction in following iterations. Note that V_{adatom} will be positive (i.e., presenting a repulsive scatterer) unless bound states are experimentally detected, which has never been the case in porous MOCNs.

(4) *Simulate the experimental LDOS and band structure*.—This is the algorithm core: Vary V_{mol}, V_{adatom}, and the 2DEG renormalization (E_0 and m^*/m_e) to match the fundamental energy (E_0) of the QD band, the top of the $n = 1$ LDOS peak, the ARPES band (E_1), and the gap size between the $n = 1$ and $n = 2$ confined states (Δ). Once the 2DEG has been renormalized to a proper value, E_0 and the gap size (Δ) values depend on V_{mol} and V_{adatom}, whereas the STS peak width and ARPES bandwidth (i.e., $E_1 - E_0$) also depend on m^*/m_e. Hence, a refinement of V_{mol} and 2DEG renormalization (E_0 and m^*/m_e) should be carried out iteratively until a satisfactory match with ARPES and STS is reached. A more accurate fitting can be obtained whenever higher confined states are introduced by the experiments (Piquero-Zulaica *et al.*, 2019a).

(5) *Extract the parameters once the iteration process does not further improve the simulations*.—These parameters reflect physically meaningful information on confinement strength, QD intercoupling, and energy and mass renormalization effects from the studied network.

Alternatively, it is tempting to envision the inversion of this iterative processes and start by proposing a set of desired electronic features to be realized: in other words, the conception of programming algorithms that work inversely by yielding experimentally feasible geometries prone to hosting specific electronic structures. In particular, methodologies were proposed for finding atomic configurations that produce a prescribed electronic structure (Franceschetti and Zunger, 1999). In this context, descriptors containing the demonstrated electronic scattering and coupling introduced by artificial lattices (Gomes *et al.*, 2012; Collins *et al.*, 2017; Slot *et al.*, 2017; Kempkes, Slot, Freeney *et al.*, 2019; Kempkes, Slot, van den Broeke *et al.*, 2019; Freeney, van den Broeke *et al.*, 2020) and/or quantum corrals (Freeney, Borman *et al.*, 2020; Li, Cao, and Ding, 2020) could be conceived to develop simplified geometries and engineer nanoarchitectures that target specific electronic effects. Indeed, machine-learning procedures are currently developing rapidly toward steering material research through data-driven codes that rely on supervised training of the algorithms (Hörmann *et al.*, 2019; Ourmazd, 2020). These methods have been recently applied to scanning probe microscopy-based experiments in order to decide on the data quality and system morphology (Alldritt *et al.*, 2020), having in mind the ultimate goal of autonomous operation (Krull *et al.*, 2020).

In short, machine-learning algorithms are anticipated that could be implemented into the EBEM or EPWE simulations to train and develop new protocols capable of providing the desired 2DEG confinement or band structures from physically meaningful scattering potential landscapes, i.e., feasible molecular superlattices. This could be combined with

recently developed first-principles machine-learning algorithms capable of predicting the crystal structure of certain organic molecules on metal surfaces (Hörmann *et al.*, 2019). When such geometries are defined, synthetic chemists could design the proposed molecular building blocks and conceive fabrication protocols to be tested experimentally.

VI. MUTUAL RESPONSE OF GUEST SPECIES AND CONFINED QUANTUM STATES

We have demonstrated that surface 2DEGs can be confined and tailored by molecular nanostructures following a proper selection of constituent materials and the development of interfacial assembly protocols. These nanoporous networks are highly versatile and provide independent tunability of all confining parameters: pore size, interpore separation, and scattering potential barriers. The addition of coordinating metal centers induces prominent effects on the 2DEG confinement, to the extent that they can strongly modify (renormalize) the pristine surface state and open interaction channels enhancing the QD coupling. Moreover, whenever the confining structure is already set, there is an additional route to tune these electronic states: the deliberate positioning of adsorbed guest species within the confining structures, which can be in the form of organic molecules, single atoms, or atom clusters (Theobald *et al.*, 2003; Negulyaev *et al.*, 2008; Blunt *et al.*, 2010; Cheng *et al.*, 2010; Pivetta *et al.*, 2013; Nowakowska *et al.*, 2015). Further information on guest species on molecular networks was provided by Bartels (2010) and Teyssandier, Feyter, and Mali (2016).

In the following, exemplary cases are described that reveal how adsorbed species are influenced by the confined LDOS, and in turn the confined states respond to the presence of adsorbed guest molecules and atoms, similar to single atoms placed in quantum corrals, discussed in the Introduction (Kliewer, Berndt, and Crampin, 2000; Stepanyuk *et al.*, 2005; Li, Cao, and Ding, 2020; Stilp *et al.*, 2021). The interplay between the organization and electronic response affecting transition metal atoms, simple molecules or noble gases, and the confined 2DEGs of 1D nanogratings and QD arrays is also addressed.

A. Self-alignment of adspecies in molecular nanogratings

The deposition of 3*d* metals (Co and Fe) into the 1D organic nanogratings described previously (cf. Fig. 14) was investigated at low temperatures to follow the electronic structure modifications and the dynamics of the system (Schiffrin *et al.*, 2008). Deposition at 8 K of Fe or Co atoms continued by a subtle annealing to 18 K modifies the randomly distributed guest atom positions, which then self-align as atomic 1D chains at the center of the furrows in the molecular nanogratings; see Fig. 24(a). Accordingly, this two-stage assembly scenario merges supramolecular organization principles with spontaneous adatom positioning steered by indirect interactions. At sufficiently high local coverage, a preferred distance between individual atoms of 23 and 25 Å results for Fe and Co atoms, respectively. This separation reveals a long-range (row-adatom or adatom-adatom) interaction mediated via the QWS, as with 2D hexagonal atomic

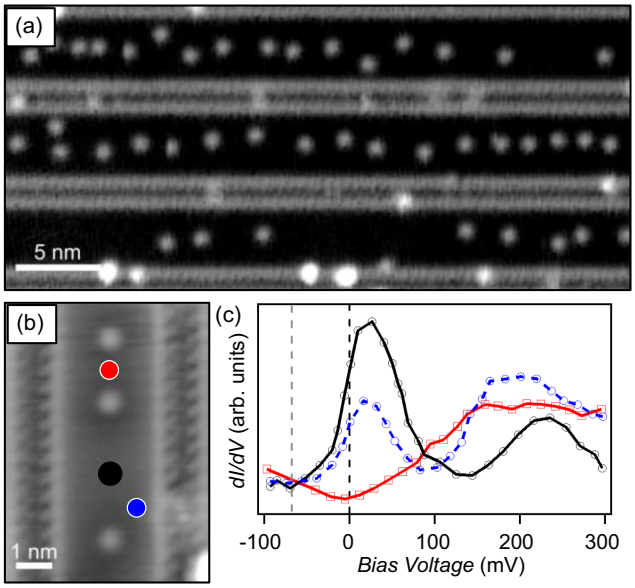

FIG. 24. Transition metal adatoms self-aligning within *L*-methionine 1D nanogratings and modification of the electronic structure (from 1D QWSs to 0D QDs). (a) Atomic chains of Co preferentially following the central axis of *L*-methionine trenches after deposition at 8 K and subsequent annealing to 18 K. (b) Tip manipulation of Fe atoms into selected interatomic distances within the 1D nanogratings. (c) The STSs at the indicated position in (b) reveal that the atoms act as scattering barriers for the 1D confined surface state and yield 0D confinement [black and blue (dark gray) circles and dashed line spectra] or quenching of the confined state [red (light gray) squares and continuous line spectrum]. Adapted from Schiffrin *et al.*, 2008.

lattices existing on pristine substrates (Repp *et al.*, 2000; Knorr *et al.*, 2002; Silly *et al.*, 2004; Negulyaev *et al.*, 2009).

Notably, 0D confinement is found for this system since the guest adatoms act as repulsive scattering barriers to the 1D confined surface-state electrons (the driving force of the atom self-alignment). This is evidenced at the LDOS when further tip manipulation procedures are applied to systematically vary the interatomic spacings at the center of a trench, which allows for the fabrication of the smallest QDs [Fig. 24(b)] (Pennec *et al.*, 2007). The STS line shapes in Fig. 24(c) display the familiar QD signatures of Fig. 15(e) instead of the QWSs of Figs. 11 and 14. Minima in the interaction energy between the atoms and the resonator boundaries are theoretically expected and observed for both metals when located at the center of the 1D trenches (Schiffrin *et al.*, 2008; Han and Weiss, 2012). In essence, by employing self-aligning atomic strings, the dimensionality and onsets of the confined states can be modified. This methodology can generally be employed for nanoscale control of matter and for the positioning of single atomic or molecular species in surface-supported supramolecular architectures. In this regard, the positioning and mobility of tetracene molecules in such methionine nanogratings has been studied (Urgel, Écija *et al.*, 2016). In addition, it was demonstrated that the spin polarization of surface electrons caused by magnetic adatoms can be projected to a remote location by quantum states of corrals (Stepanyuk *et al.*, 2005). In particular, the exchange

interaction between magnetic atoms is operative at appreciable distances and a similar behavior is expected for magnetic atoms organized in such 1D nanogratings or QD arrays (Pennec *et al.*, 2007; Pivetta *et al.*, 2013); see Figs. 24(a) and 25(c).

B. Guided adsorption of adatoms and simple molecules in QD arrays

The presence of a 2DEG can strongly influence the self-assembly processes of the adsorbed species (Wang *et al.*, 2009). This is also the case whenever the surface state is confined. As a first example, the adsorption of CO molecules at the pores of the chiral anthraquinone (AQ) network grown on Cu(111) (Cheng *et al.*, 2010) is discussed; see Figs. 25(a) and 25(b). This AQ network presents one of the largest regular pore areas since the self-assembly is mediated by C-H-O interactions that involve 18 molecules (Pawin *et al.*, 2006; Cheng *et al.*, 2010; Wyrick *et al.*, 2011). At 40 K, the diffusion of the CO molecules is restricted to a single pore and dynamic processes confirm their repulsive character (Cheng *et al.*, 2010). Indeed, a hierarchy of preferred adsorption sites prevails, depending on the number of CO molecules captured within a pore. For a single CO molecule, the center of the network cavity is favored and maintained whenever a second CO molecule is added, which then sits on a site midway between the pore center and the edge. Further captured COs will preferentially occupy any available halfway adsorption site. Simulations for this system concluded that the first and second confined states (in that order) drive the CO adsorption positions (Cheng *et al.*, 2010), whereby CO molecules seize adsorption sites with high LDOSs. Therefore, the diffusion is limited not only by the physical barriers (molecules) but also by the modified LDOS generated by the QD array (Einstein, Bartels, and Morales-Cifuentes, 2018).

Similarly, the arrangement of Fe atoms follows a related scheme when filling the pores of dicyano-poly(*p*-phenylene) based MOCNs (Pivetta *et al.*, 2013). In particular, the adsorption of Fe atoms within a Ph5 + Cu MOCN assembled on Cu(111) preferentially follows electron-mediated interactions between the adatoms, which are reinforced by the cavity confined surface electrons [Fig. 25(c)]. Thus, a certain control over the guest species arrangement is exerted by a proper selection of the network used as the confining template. Like the previously described atomic chains in supramolecular nanogrids, this process requires thermal activation, and upon overcoming the aggregation energy barrier discrete Fe clusters in the pores are obtained.

Finally, the last example addresses the adsorption of Xe noble gas atoms into the well characterized DPDI + Cu network (Nowakowska *et al.*, 2015, 2016; Ahsan *et al.*, 2019a, 2019b). The atom-by-atom condensation leads to a maximum occupation of 12 Xe guest atoms that do not follow a single set of hierarchic filling rules, but instead adapt their structures to their neighbors (Nowakowska *et al.*, 2015, 2016); see Fig. 25(d). This pore saturation exhibits tetramer grouping with Xe atoms adsorbed at on-top sites of the Cu(111) atomic lattice, resulting in a $(\sqrt{3}\times\sqrt{3})R30°$ overlayer structure that coincides with the ordering of Xe on pristine Cu(111) (Seyller *et al.*, 1998). This tetramer grouping matches the threefold symmetry of the DPDI network with respect to the substrate (Piquero-Zulaica *et al.*, 2019a). In other words, the $n = 2$ confined state (closest to the Fermi energy) appears to guide the Xe condensation. Alternatively, these Xe atoms could simply be marking the three equivalent metal coordination sites that exhibit the lowest surface potential of the network (Dil *et al.*, 2008; Piquero-Zulaica *et al.*, 2019a).

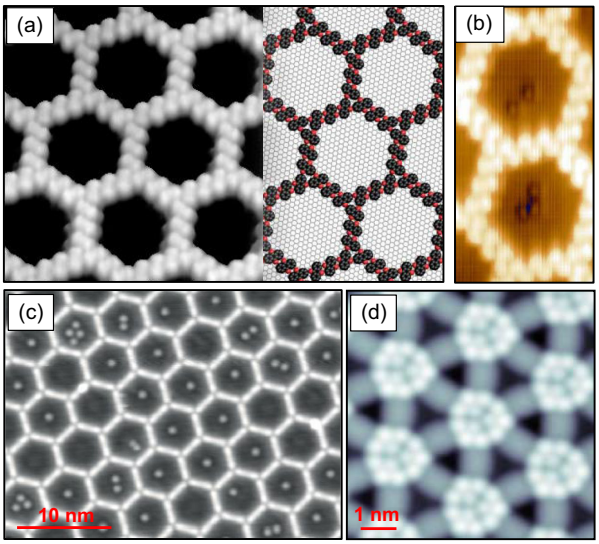

FIG. 25. Adsorbed species guided by the confined LDOS in QD arrrays. (a) Overview topograph (26×15 nm^2) of the chiral anthraquinone network generated on Cu(111). Adapted from Pawin *et al.*, 2006. (b) Adsorption of CO molecules within the network pores (dark protrusions) where their diffusion becomes defined by the confined LDOS. The image size corresponds to 6×10 nm^2. Adapted from Cheng *et al.*, 2010. (c) Fe single atoms packing on Ph5 + Cu MOCN on Cu(111). Adapted from Pivetta *et al.*, 2013. (d) Xe adsorption on the 3deh-DPDI network showing a maximum packing of 12 atoms in threefold bunches. Adapted from Nowakowska *et al.*, 2015.

In this context, note that any mobility of hosted species entails a temporally fluctuating confinement geometry. Thus, monomers or trimeric units caged in nanoporous honeycomb MOCNs are expected to present dynamic confinement patterns, which can vary rapidly and account for complex electronic configurations (Kühne *et al.*, 2010; Palma *et al.*, 2014, 2015).

C. Configuring QD states through manipulation of guest adsorbates

Xe occupation and its effect on QD electronic properties were investigated with respect to its adjacent neighbors on the DPDI + Cu network (Nowakowska *et al.*, 2016). This system was chosen because Xe is physisorbed within these pores and can be atomically manipulated using a STM tip. In this way, artificial intermediate situations can be created between empty and saturated pores, simulating an electronic breadboard; see Figs. 26(a)–26(d). The empty pore case was addressed electronically in Figs. 18 and 19 and exhibits a broad $n = 1$ confined peak with a maximum around ~ -0.2 V that relates to the first QD array band; see Fig. 26(a). Upon Xe saturation, this confined state peak shifts by ~60 mV toward

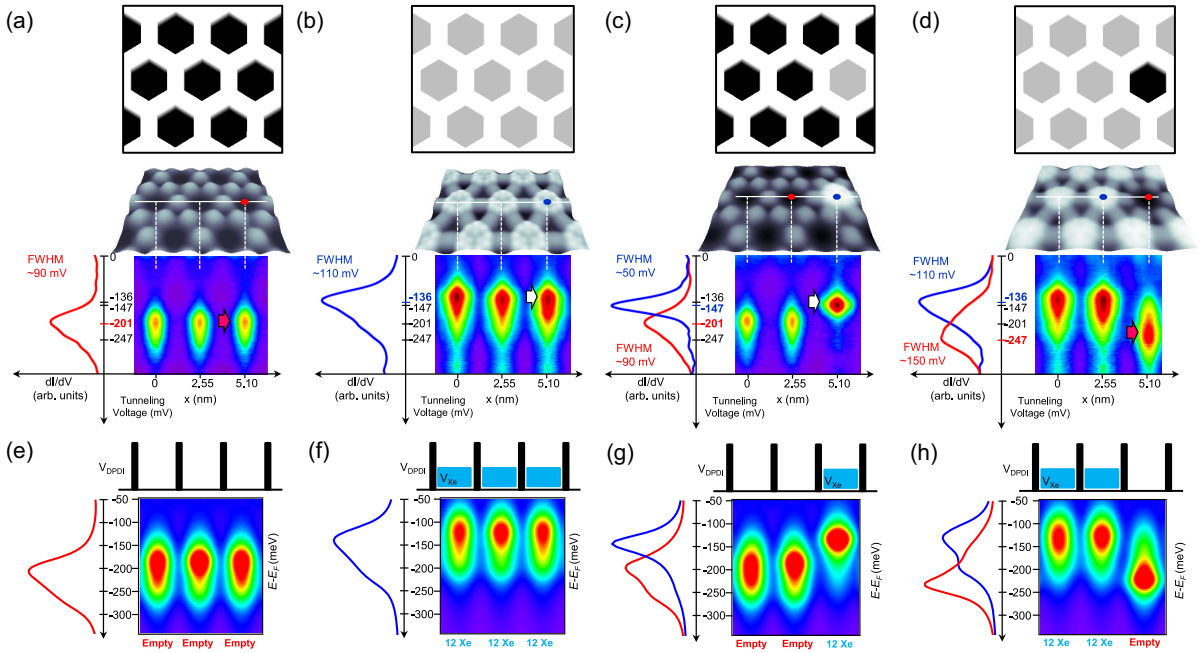

FIG. 26. QD electronic structure alteration by pore occupation in the 3deh-DPDI network. Depending on the Xe occupation of the pores, four different configurations are shown: (a) empty network, (b) saturated network, (c) single filled pore, and (d) single empty pore. These panels contain the experimental information where the STM images are displayed at the top, a dI/dV linescan passing through the center of three neighboring pores can be found below, and position-dependent STSs are displayed on the left. (e)–(h) EPWE simulated LDOSs (linescans and STSs) for the upper cases. A significant modification of the LDOS is evident upon Xe occupation and depends on the state of the neighboring pores, evoking an electronic breadboard. Adapted from Nowakowska *et al.*, 2016.

the Fermi level. This up-shift effect is attributed to Pauli repulsion between the rare gases and the confined states (Park *et al.*, 2000; Hövel, Grimm, and Reihl, 2001; Forster, Hüfner, and Reinert, 2004). Note that the broad peak width remains since the Xe physisorption at the pores does not significantly affect the interpore coupling, as evidenced by ARPES measurements (Nowakowska *et al.*, 2016).

Intermediate cases achieved through atomic manipulation are a single filled pore within an otherwise empty network [Fig. 26(c)] and an empty pore embedded in a Xe saturated network [Fig. 26(d)]. Different occupation-dependent electronic states (QD states) are observed that display shifted energy maxima. In practice, the isolated filled pore shows a sharp (noncoupled) confined state peaking close to the Xe filled network energy [Fig. 26(b)], whereas the empty one displays a broad peak close to the fundamental energy of the pristine network [Fig. 26(a)]. Note that the neighboring pores appear to be electronically unaffected by these local perturbations; hence, for the overall system they can be considered isolated defects.

EPWE was used to simulate the Xe-induced effect in these four cases and gain insight into the confinement strength and QD coupling. The simulated LDOS depicted in the bottom row of Fig. 26 uses scattering potentials of $V_{\mathrm{mol}} = V_{\mathrm{adatoms}} = 390$ meV (from Table II) and $V_{\mathrm{Xe}} = 80$ meV at the occupied pores to account for the Pauli repulsion effect induced by the Xe adatoms. Not only the energy shifts but also the confined state peak widths and shapes are accurately matched. From these simulations we conclude that the presence of Xe at the pores generates an energy up-shift of the confined states that maintains extended Bloch waves because the interpore coupling is not affected. The fact that the peak energies are markedly different between Xe filled and empty pores indicates that this system can be used as an electronic breadboard to store information with a bit areal density of 2×10^{13} bits/cm^2 by far exceeding current hard disk storage densities. A similar density of 7.7×10^{13} bits/cm^2 was achieved by manipulating Cl vacancies on Cu(100) (Kalff *et al.*, 2016).

VII. CONCLUSIONS AND OUTLOOK

Throughout this review, we comprehensively illustrated the wide range of opportunities that molecular nanoarchitectures provide for confining and engineering surface 2D electron gases. The capability to fabricate intricate arrangements with atomic precision combined with the chemical versatility of tailored molecular building blocks provides a multitude of opportunities to realize molecular nanosystems at different levels of complexity, featuring the desired scattering potential barriers that control surface electrons and shape the interfacial electronic landscape. Ultimately, the described quantum state engineering strategy relies on the spatial positioning and physicochemical nature of the embedded compounds. Although focus was placed on the fcc(111) surfaces of copper, silver, and gold, the elaborated principles are applicable to many other systems exhibiting quasifree electrons on their surface, such as 3D topological insulators (Sessi *et al.*, 2014), semiconductors (Pham, Kanisawa, and Fölsch, 2019), surface alloys (Jolie *et al.*, 2022), 2D materials, or thin film superconductors

(Yan *et al.*, 2021). To date a variety of molecular nanostructures have been realized on such templates (Kumar, Banerjee, and Liljeroth, 2017; Auwärter, 2019), although the respective electron confinement and quantum engineering prospects remain to be fully explored.

Suitable molecular nanostructures can be readily obtained by STM tip manipulation, molecular self-assembly protocols, or both. Such construction schemes have substantially expanded the available methodology initially pioneered with atomic quantum corrals and vicinal surfaces. The molecular structures are highly versatile, whereby all the confining parameters and the QD intercoupling degree among repeating units could be addressed. This bears the prospect of efficient fabrication of confining structures at the technological level, as well as miniaturization for device integration. However, major obstacles must be overcome in this regard. In particular, the serial STM manipulation of adsorbates employed for creating artificial lattices demand specific conditions such as movable building units, cryogenic environments, and extensive construction times. This turns into a critical challenge when mesoscale structures that are essential for practical applications are targeted. Building extended regular systems could be feasible using automated STM manipulation with suitable algorithms. Nonetheless, such artificial lattices play an important role in 2DEG engineering involving non-noble-metal substrates, such as surface alloys (Jolie *et al.*, 2022), topological insulators (Sessi *et al.*, 2014), semiconductors (Pham, Kanisawa, and Fölsch, 2019), and superconductors. Here different scatterers beyond the commonly used CO and coronene are of interest, such as halogens like Br, heavy elements like Bi and Pb, or combinations of these and others. In addition, the control of the scattering barrier reflectivity poses challenges, although the use of buffer layers or thin films might be advantageous for limiting the 2DEG coupling with bulk states.

Unlike artificial lattices, mesoscopic structures of self-assembled organic and metal-organic open networks are readily available and highly versatile. Although currently limited to smooth fcc(111) metal surfaces, promising explorative studies were performed using 2D-material substrates (Urgel *et al.*, 2015; Kumar, Banerjee, and Liljeroth, 2017; Kumar *et al.*, 2018; Li *et al.*, 2019). Further alternatives might come in the form of appropriate transfer protocols (Moreno *et al.*, 2018; Ohtomo *et al.*, 2018), Si intercalation (Deniz *et al.*, 2017; Sun and Kawai, 2021), and noble metal etching techniques (Mutlu, Llinas *et al.*, 2021) affording electronic decoupling of molecular nanostructures and interfacing with device relevant substrates.

The experimental and theoretical cases described reveal further insights into the scattering potential configurations that molecular nanoarchitectures and networks represent to surface electrons. While molecules typically exhibit strong repulsive potential barriers for 2DEG electrons, metal centers of metal-organic networks are less predictable and generally weaker in their scattering strength. Moreover, metal centers present the notable property of significantly renormalizing the pristine surface-state onset whereby the coordination spheres can provide distinct leakage channels to enhance the QD intercoupling. In essence, open molecule-based networks modulate 2DEGs through the potential barriers they produce and frequently generate distinct band structures that can easily be engineered through self-assembly protocols.

In addition, positioning of guest species at nanogrids or network pores provides an extra route to alter the confined electronic states. Furthermore, systems with significant energy differences between occupied and empty states represent breadboards to engineer artificial lattices. These electronic breadboards are envisioned as operating COFs or nanoporous graphenes (NPGs) and are considered stable and addressable at room temperature.

The semiempirical methods used to rationalize quantum state engineering and band structure formation have significantly improved over the years and successfully model the scattering potential landscape underlying 2DEG confinement. We can now envision the use of machine learning to propose molecular geometries that induce the electronic properties that we ultimately desire. Such machine-learning processes could exploit the inverse EPWE methodology or other approaches and guide the design of novel artificial molecular lattices beyond those already explored.

The current scope of achievements suggests that the field is reaching maturity, ultimately preparing for the establishment of a rationale. We now have the ability, ingredients, and methodology to generate well-defined molecular (and atomic) nanoarchitectures, thus opening up a multitude of opportunities for surface electronic structure and functionality design.

Within this vast playground we can relate established optical effects to low-dimensional quantum systems using the ability to directly image the QPI patterns generated by these nanostructures, with the benefit of a 1000-fold reduction in wavelength and structural parameters (García de Abajo *et al.*, 2010). Indeed, exotic refraction anomalies leading to few nanometer electron focusing (collimation) or negative refraction and beam splitting have been predicted for triangular superlattices (García de Abajo *et al.*, 2010; Abd El-Fattah *et al.*, 2017); see Figs. 27(a) and 27(b). In addition, Snell's law for electronic propagation was validated by lateral electron wave refraction in simpler 2D systems (Repp, Meyer, and Rieder, 2004); see Fig. 27(c). Likewise, diffraction and interference patterns analogous to photons in coupled waveguides (the Talbot effect) have been predicted in NPGs due to the presence of Dirac cones in the band structure (Moreno *et al.*, 2018; Calogero *et al.*, 2019); see Fig. 27(d). Accordingly, the existence of these topological signatures in artificial lattices and networks should promote similar optical-like properties in selected 2DEG scattering nanostructures. A further relevant prospect is the replication of the quantum holography concept by means of artificial lattices that can overcome the single-atom limit for information storage density (Moon *et al.*, 2009). Indeed, the introduction of magnetism into the system could double the information density compared to volumetric quantum holographic encoding while being experimentally accessible using a spin-polarized STM (Brovko and Stepanyuk, 2012).

Novel quantum properties are also envisioned upon the advancement of design principles of engineered 2DEGs. In particular, electronic scattering and confinement effects should be transferable to image potential states that are

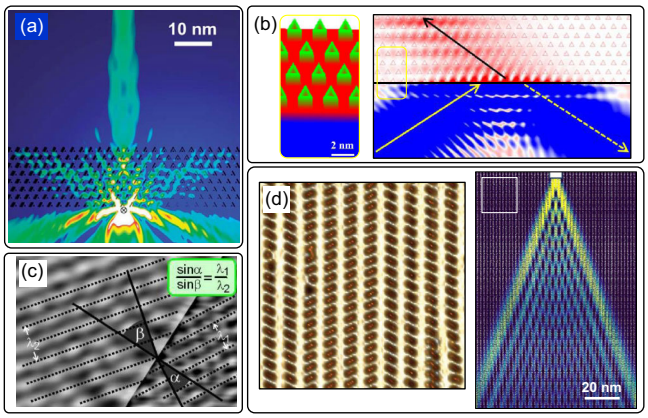

FIG. 27. Optical effects mimicked with electrons using organic and inorganic nanostructures. (a),(b) Simulations of electron collimation and negative refraction at Cu(111) and 1 ML Ag/Cu(111) lateral interfaces. Adapted from García de Abajo *et al.*, 2010, and Abd El-Fattah *et al.*, 2017. (c) Experimental verification of Snell's law at a Cu(111) and 2 ML NaCl/Cu(111) interface. The refraction of electronic wave fronts (black dotted lines) is visible in the real-space atomic resolution STM image. Adapted from Repp, Meyer, and Rieder, 2004. (d) Left picture: STM image of the 7-13-AGNR fused NPG array on Au(111). Right image: diffractive Talbot effect propagation simulation performed for such extended NPG arrays. The left STM image corresponds to a region of 18×18 nm^2 that fits into the white square at the top of this image. Adapted from Moreno *et al.*, 2018, and Calogero *et al.*, 2019.

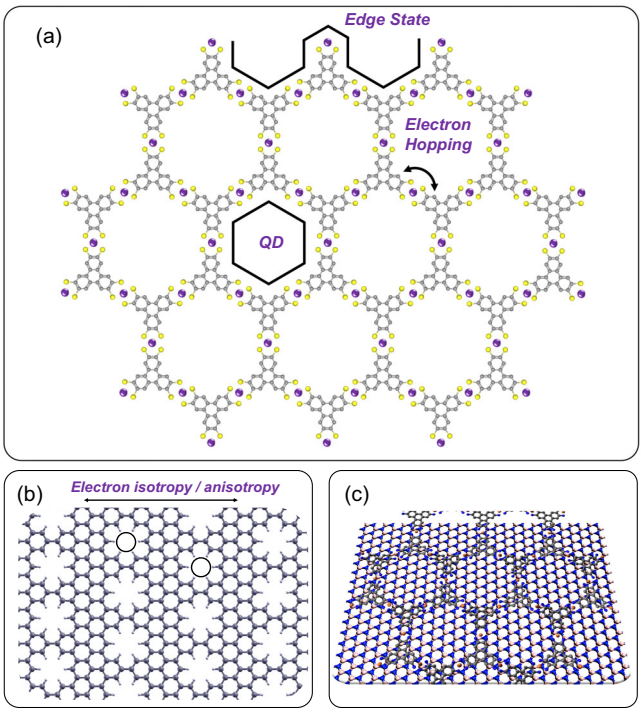

FIG. 28. Perspectives on open metal-organic nanostructures going beyond 2DEG scattering. (a) According to theoretical predictions, certain MOCNs exhibit topological edge states and collective magnetic properties (superconductors or ferromagnets). (b) Two-dimensional COFs with nanopores are expected to evolve from appropriate 2D MOCN precursors. The geometry of the pores can introduce electronic anisotropy into the system, and the pores can bestow extra functionalities on devices. (c) Applying these nanostructures to selected nonmetallic substrates, such as topological insulators, transition metal dichalcogenides, and 2D materials, is promising for the emergence of novel quantum states of matter.

accessible via STS or 2PPE techniques (Echenique *et al.*, 2004; Schouteden and Van Haesendonck, 2012; Niesner and Fauster, 2014; Rejali *et al.*, 2022). Additionally, network modified 2DEGs have recently been proposed to play a key role in the stabilization and the significant energy down-shifting of superatom molecular orbitals (Kawai *et al.*, 2021). These states of molecular origin feature a localized and simultaneously high DOS at small pores (~0.5 nm wide) that could be useful in future applications (Zhang, Björk *et al.*, 2016; Hieulle *et al.*, 2018; Moreno *et al.*, 2018; Kawai *et al.*, 2021).

From a fundamental perspective, further insights are required beyond the 2DEG scattering and confinement properties in molecule-based networks. These include the experimental validation of theoretically predicted MOCN characteristics associated with organic topological insulators, superconductors, quantum spin liquid systems, or ferromagnets (Wang, Liu, and Liu, 2013; Dong *et al.*, 2016; Zhang, Wang *et al.*, 2016; Zhang *et al.*, 2017; Kumar *et al.*, 2018; Sun *et al.*, 2018; Gao *et al.*, 2019, 2020; R. Zhang *et al.*, 2020; Hernández-López *et al.*, 2021); see Fig. 28(a). Likewise, the on-surface synthesis of atomically precise, periodic, and extended nanoporous 2D COFs is tackled experimentally (Bieri *et al.*, 2009; Galeotti *et al.*, 2020). The formation of such topological arrays is envisioned from a particular, prearranged, well-defined, and extended nanoporous network (Grossmann *et al.*, 2021). The expected technological relevance of such 2D COFs and NPGs is significant since they can be transferred to other relevant supports and used in field-effect transistors (Moreno *et al.*, 2018; Mutlu, Jacobse *et al.*, 2021). In addition, as illustrated in Fig. 28(b), the nanopores could introduce anisotropy of electronic transport (as for NPG structures) or provide additional functionality for selective gas uptake and heterogeneous catalysis (Moreno *et al.*, 2018; Jacobse *et al.*, 2020).

From a practical point of view, these emerging quantum states of matter should be extended to nonmetal substrates such as 2D layered materials, topological insulators, semiconductors, superconducting substrates, or hybrid structures, which are considered to underpin future device architectures (Gobbi, Orgiu, and Samorì, 2018); see Fig. 28(c). Steps to make this a reality are currently under way. For example, molecular networks have been used to alter the properties of graphene by inducing an extended and atomically well-defined covalent interlayer coupling (Yu *et al.*, 2020). Molecule-based (metal-)organic nanoporous networks and artificial lattices offer interesting prospects and inspiration for the quantum era ahead.

ACKNOWLEDGMENTS

We are grateful to all graduate students, cooperation partners, and colleagues co-authoring original work. We appreciate the constructive feedback of all reviewers, including Ingmar

Swart. I. P.-Z., J. L.-C., and J. E. O. acknowledge financial support from the Spanish Ministry of Science and Innovation (MICINN) and the Agencia Estatal de Investigación (AEI) (Grants No. PID2019-107338RB-C6-3 and No. PID2019-107338RB-C6-4/AEI/10.13039/501100011033), from the regional Government of Aragon (Grant No. E12-20R) and the Basque Government (Grant No. IT-1255-19), and from the European Regional Development Fund (ERDF) under the program Interreg V-A España-Francia-Andorra (Contract No. EFA 194/16 TNSI). W. A. acknowledges funding from the German Research Foundation (DFG; Heisenberg professorship) and the ERC Consolidator Grant NanoSurfs, and J. V. B. acknowledges support from DFG (BA 3395/2-1), ERC (Advanced Grant MolArt), and the DFG Excellence Cluster Munich Center of Quantum Science and Technology (MCQST).

REFERENCES

Abd El-Fattah, Z. M., M. A. Kher-Elden, I. Piquero-Zulaica, F. J. G. de Abajo, and J. E. Ortega, 2019, Phys. Rev. B **99**, 115443.
Abd El-Fattah, Z. M., M. A. Kher-Elden, O. Yassin, M. M. El-Okr, J. E. Ortega, and F. J. García de Abajo, 2017, J. Appl. Phys. **122**, 195306.
Abdurakhmanova, N., T.-C. Tseng, A. Langner, C. S. Kley, V. Sessi, S. Stepanow, and K. Kern, 2013, Phys. Rev. Lett. **110**, 027202.
Ahsan, A., S. F. Mousavi, T. Nijs, S. Nowakowska, O. Popova, A. Wäckerlin, J. Björk, L. H. Gade, and T. A. Jung, 2019a, Nanoscale **11**, 4895.
Ahsan, A., S. F. Mousavi, T. Nijs, S. Nowakowska, O. Popova, A. Wäckerlin, J. Björk, L. H. Gade, and T. A. Jung, 2019b, Small **15**, 1803169.
Ali, K., *et al.*, 2021, Adv. Sci. Lett. **8**, 2101455.
Alldritt, B., P. Hapala, N. Oinonen, F. Urtev, O. Krejci, F. Federici Canova, J. Kannala, F. Schulz, P. Liljeroth, and A. S. Foster, 2020, Sci. Adv. **6**, eaay6913.
Amano, H., N. Sawaki, I. Akasaki, and Y. Toyoda, 1986, Appl. Phys. Lett. **48**, 353.
Andrei, E. Y., and A. H. MacDonald, 2020, Nat. Mater. **19**, 1265.
Ashcroft, N. W., and N. D. Mermin, 1976, *Solid State Physics* (Holt, Rinehart and Winston, New York).
Auwärter, W., 2019, Surf. Sci. Rep. **74**, 1.
Auwärter, W., *et al.*, 2010, Phys. Rev. B **81**, 245403.
Avouris, P., and I.-W. Lyo, 1994, Science **264**, 942.
Avraham, N., *et al.*, 2020, Nat. Mater. **19**, 610.
Bartels, L., 2010, Nat. Chem. **2**, 87.
Barth, J. V., 2007, Annu. Rev. Phys. Chem. **58**, 375.
Barth, J. V., 2009, Surf. Sci. **603**, 1533.
Barth, J. V., G. Costantini, and K. Kern, 2005, Nature (London) **437**, 671.
Barth, J. V., J. Weckesser, C. Cai, P. Günter, L. Bürgi, O. Jeandupeux, and K. Kern, 2000, Angew. Chem., Int. Ed. Engl. **39**, 1230.
Baumberger, F., T. Greber, B. Delley, and J. Osterwalder, 2002, Phys. Rev. Lett. **88**, 237601.
Baumberger, F., M. Hengsberger, M. Muntwiler, M. Shi, J. Krempasky, L. Patthey, J. Osterwalder, and T. Greber, 2004, Phys. Rev. Lett. **92**, 196805.
Bertel, E., and N. Memmel, 1996, Appl. Phys. A **63**, 523.
Bieri, M., *et al.*, 2009, Chem. Commun. (Cambridge, England), 6919.
Binasch, G., P. Grünberg, F. Saurenbach, and W. Zinn, 1989, Phys. Rev. B **39**, 4828.
Binnig, G., and H. Rohrer, 1987, Rev. Mod. Phys. **59**, 615.
Bloch, I., J. Dalibard, and W. Zwerger, 2008, Rev. Mod. Phys. **80**, 885.
Blunt, M. O., J. C. Russell, N. R. Champness, and P. H. Beton, 2010, Chem. Commun. (Cambridge, England) **46**, 7157.
Bouju, X., C. Mattioli, G. Franc, A. Pujol, and A. Gourdon, 2017, Chem. Rev. **117**, 1407.
Braun, K.-F., and K.-H. Rieder, 2002, Phys. Rev. Lett. **88**, 096801.
Brennan, K. F., 1999, *The Physics of Semiconductors: With Applications to Optoelectronic Devices*, 1st ed. (Cambridge University Press, Cambridge, England).
Broome, M. A., *et al.*, 2018, Nat. Commun. **9**, 980.
Brovko, O. O., and V. S. Stepanyuk, 2012, Appl. Phys. Lett. **100**, 163112.
Bürgi, L., O. Jeandupeux, A. Hirstein, H. Brune, and K. Kern, 1998, Phys. Rev. Lett. **81**, 5370.
Calogero, G., N. R. Papior, B. Kretz, A. Garcia-Lekue, T. Frederiksen, and M. Brandbyge, 2019, Nano Lett. **19**, 576.
Cao, Y., V. Fatemi, S. Fang, K. Watanabe, T. Taniguchi, E. Kaxiras, and P. Jarillo-Herrero, 2018, Nature (London) **556**, 43.
Cao, Y., *et al.*, 2018, Nature (London) **556**, 80.
Caplins, B. W., D. E. Suich, A. J. Shearer, and C. B. Harris, 2014, J. Phys. Chem. Lett. **5**, 1679.
Čechal, J., C. S. Kley, R. Pétuya, F. Schramm, M. Ruben, S. Stepanow, A. Arnau, and K. Kern 2016, J. Phys. Chem. C **120**, 18622.
Celotta, R. J., S. B. Balakirsky, A. P. Fein, F. M. Hess, G. M. Rutter, and J. A. Stroscio, 2014, Rev. Sci. Instrum. **85**, 121301.
Chen, M., J. Shang, Y. Wang, K. Wu, J. Kuttner, G. Hilt, W. Hieringer, and J. M. Gottfried, 2017, ACS Nano **11**, 134.
Chen, M., *et al.*, 2019, Sci. Adv. **5**, eaaw3988.
Chen, W., V. Madhavan, T. Jamneala, and M. F. Crommie, 1998, Phys. Rev. Lett. **80**, 1469.
Cheng, Z., J. Wyrick, M. Luo, D. Sun, D. Kim, Y. Zhu, W. Lu, K. Kim, T. L. Einstein, and L. Bartels, 2010, Phys. Rev. Lett. **105**, 066104.
Choi, D.-J., N. Lorente, J. Wiebe, K. von Bergmann, A. F. Otte, and A. J. Heinrich, 2019, Rev. Mod. Phys. **91**, 041001.
Chung, K.-H., J. Park, K. Y. Kim, J. K. Yoon, H. Kim, S. Han, and S.-J. Kahng, 2011, Chem. Commun. (Cambridge, England) **47**, 11492.
Clair, S., S. Pons, H. Brune, K. Kern, and J. V. Barth, 2005, Angew. Chem., Int. Ed. **44**, 7294.
Colazzo, L., M. S. G. Mohammed, A. Gallardo, Z. M. Abd El-Fattah, J. A. Pomposo, P. Jelínek, and D. G. de Oteyza, 2019, Nanoscale **11**, 15567.
Collins, L. C., T. G. Witte, R. Silverman, D. B. Green, and K. K. Gomes, 2017, Nat. Commun. **8**, 15961.
Crampin, S., and O. R. Bryant, 1996, Phys. Rev. B **54**, R17367.
Crampin, S., H. Jensen, J. Kröger, L. Limot, and R. Berndt, 2005, Phys. Rev. B **72**, 035443.
Crommie, M. F., C. P. Lutz, and D. M. Eigler, 1993a, Science **262**, 218.
Crommie, M. F., C. P. Lutz, and D. M. Eigler, 1993b, Nature (London) **363**, 524.
Crommie, M. F., C. P. Lutz, D. M. Eigler, and E. J. Heller, 1995a, Physica (Amsterdam) **83D**, 98.
Crommie, M. F., C. P. Lutz, D. M. Eigler, and E. J. Heller, 1995b, Surf. Rev. Lett. **02**, 127.
Damascelli, A., Z. Hussain, and Z.-X. Shen, 2003, Rev. Mod. Phys. **75**, 473.
Davis, K. B., M. O. Mewes, M. R. Andrews, N. J. van Druten, D. S. Durfee, D. M. Kurn, and W. Ketterle, 1995, Phys. Rev. Lett. **75**, 3969.

Deniz, O., C. Sánchez-Sánchez, T. Dumslaff, X. Feng, A. Narita, K. Müllen, N. Kharche, V. Meunier, R. Fasel, and P. Ruffieux, 2017, Nano Lett. **17**, 2197.

Díaz-Tendero, S., F. E. Olsson, A. G. Borisov, and J.-P. Gauyacq, 2008, Phys. Rev. B **77**, 205403.

Dil, H., J. Lobo-Checa, R. Laskowski, P. Blaha, S. Berner, J. Osterwalder, and T. Greber, 2008, Science **319**, 1824.

Ding, H. F., V. S. Stepanyuk, P. A. Ignatiev, N. N. Negulyaev, L. Niebergall, M. Wasniowska, C. L. Gao, P. Bruno, and J. Kirschner, 2007, Phys. Rev. B **76**, 033409.

Dong, L., Z. Gao, and N. Lin, 2016, Prog. Surf. Sci. **91**, 101.

Dong, L., Y. Kim, D. Er, A. M. Rappe, and V. B. Shenoy, 2016, Phys. Rev. Lett. **116**, 096601.

Drost, R., T. Ojanen, A. Harju, and P. Liljeroth, 2017, Nat. Phys. **13**, 668.

Duke, C. B., 2003, Proc. Natl. Acad. Sci. U.S.A. **100**, 3858.

Echenique, P., R. Berndt, E. Chulkov, T. Fauster, A. Goldmann, and U. Höfer, 2004, Surf. Sci. Rep. **52**, 219.

Écija, D., *et al.*, 2013, Proc. Natl. Acad. Sci. U.S.A. **110**, 6678.

Écija, D., J. I. Urgel, A. P. Seitsonen, W. Auwärter, and J. V. Barth, 2018, Acc. Chem. Res. **51**, 365.

Eigler, D. M., and E. K. Schweizer, 1990, Nature (London) **344**, 524.

Einstein, T. L., L. Bartels, and J. R. Morales-Cifuentes, 2018, e-J. Surf. Sci. Nanotechnol. **16**, 201.

Faraggi, M. N., N. Jiang, N. Gonzalez-Lakunza, A. Langner, S. Stepanow, K. Kern, and A. Arnau, 2012, J. Phys. Chem. C **116**, 24558.

Feenstra, R. M., 1994, Surf. Sci. **299–300**, 965.

Fernández, J., M. Moro-Lagares, D. Serrate, and A. A. Aligia, 2016, Phys. Rev. B **94**, 075408.

Fiete, G. A., and E. J. Heller, 2003, Rev. Mod. Phys. **75**, 933.

Figgins, J., L. S. Mattos, W. Mar, Y.-T. Chen, H. C. Manoharan, and D. K. Morr, 2019, Nat. Commun. **10**, 5588.

Forster, F., S. Hüfner, and F. Reinert, 2004, J. Phys. Chem. B **108**, 14692.

Franceschetti, A., and A. Zunger, 1999, Nature (London) **402**, 60.

Freeney, S., S. Borman, J. Harteveld, and I. Swart, 2020, SciPost Phys. **9**, 85.

Freeney, S. E., M. R. Slot, T. S. Gardenier, I. Swart, and D. Vanmaekelbergh, 2022, ACS Nanosci. Au **2**, 198.

Freeney, S. E., J. J. van den Broeke, A. J. J. Harsveld van der Veen, I. Swart, and C. Morais Smith, 2020, Phys. Rev. Lett. **124**, 236404.

Friedel, J., 1958, Nuovo Cimento **7**, 287.

Galbraith, M. C. E., M. Marks, R. Tonner, and U. Höfer, 2014, J. Phys. Chem. Lett. **5**, 50.

Galeotti, G., *et al.*, 2020, Nat. Mater. **19**, 874.

Gambardella, P., *et al.*, 2003, Science **300**, 1130.

Gao, Z., Y. Gao, M. Hua, J. Liu, L. Huang, and N. Lin, 2020, J. Phys. Chem. C **124**, 27017.

Gao, Z., *et al.*, 2019, Nanoscale **11**, 878.

García de Abajo, F. J., J. Cordón, M. Corso, F. Schiller, and J. E. Ortega, 2010, Nanoscale **2**, 717.

Gardenier, T. S., J. J. van den Broeke, J. R. Moes, I. Swart, C. Delerue, M. R. Slot, C. M. Smith, and D. Vanmaekelbergh, 2020, ACS Nano **14**, 13638.

Girovsky, J., J. L. Lado, F. E. Kalff, E. Fahrenfort, L. J. J. M. Peters, J. Fernández-Rossier, and A. F. Otte, 2017, SciPost Phys. **2**, 020.

Girovsky, J., *et al.*, 2017, Nat. Commun. **8**, 15388.

Gobbi, M., E. Orgiu, and P. Samorì, 2018, Adv. Mater. **30**, 1706103.

Goiri, E., P. Borghetti, A. El-Sayed, J. E. Ortega, and D. G. de Oteyza, 2016, Adv. Mater. **28**, 1340.

Gomes, K. K., W. Mar, W. Ko, F. Guinea, and H. C. Manoharan, 2012, Nature (London) **483**, 306.

Gong, C., *et al.*, 2017, Nature (London) **546**, 265.

Goronzy, D. P., *et al.*, 2018, ACS Nano **12**, 7445.

Greiner, M., O. Mandel, T. Esslinger, T. W. Hänsch, and I. Bloch, 2002, Nature (London) **415**, 39.

Gross, L., F. Moresco, L. Savio, A. Gourdon, C. Joachim, and K.-H. Rieder, 2004, Phys. Rev. Lett. **93**, 056103.

Grossmann, L., B. T. King, S. Reichlmaier, N. Hartmann, J. Rosen, W. M. Heckl, J. Björk, and M. Lackinger, 2021, Nat. Chem. **13**, 730.

Grothe, S., S. Johnston, S. Chi, P. Dosanjh, S. A. Burke, and Y. Pennec, 2013, Phys. Rev. Lett. **111**, 246804.

Gutzler, R., S. Stepanow, D. Grumelli, M. Lingenfelder, and K. Kern, 2015, Acc. Chem. Res. **48**, 2132.

Han, P., and P. S. Weiss, 2012, Surf. Sci. Rep. **67**, 19.

Han, Z., G. Czap, C.-l. Chiang, C. Xu, P. J. Wagner, X. Wei, Y. Zhang, R. Wu, and W. Ho, 2017, Science **358**, 206.

Hanson, R., L. P. Kouwenhoven, J. R. Petta, S. Tarucha, and L. M. K. Vandersypen, 2007, Rev. Mod. Phys. **79**, 1217.

Hao, Z., L. Song, C. Yan, H. Zhang, Z. Ruan, S. Sun, J. Lu, and J. Cai, 2019, Chem. Commun. (Cambridge, England) **55**, 10800.

Harbury, H. K., and W. Porod, 1996, Phys. Rev. B **53**, 15455.

Harrison, P., 2005, *Quantum Wells, Wires and Dots: Theoretical and Computational Physics of Semiconductor Nanostructures* (John Wiley & Sons, Chichester, England).

Hasegawa, Y., and P. Avouris, 1993, Phys. Rev. Lett. **71**, 1071.

Heeger, A. J., S. Kivelson, J. R. Schrieffer, and W. P. Su, 1988, Rev. Mod. Phys. **60**, 781.

Heller, E. J., M. F. Crommie, C. P. Lutz, and D. M. Eigler, 1994, Nature (London) **369**, 464.

Hernández-López, L., I. Piquero-Zulaica, C. A. Downing, M. Piantek, J. Fujii, D. Serrate, J. E. Ortega, F. Bartolomé, and J. Lobo-Checa, 2021, Nanoscale **13**, 5216.

Herrera, M. A. J., S. N. Kempkes, M. B. de Paz, A. García-Etxarri, I. Swart, C. M. Smith, and D. Bercioux, 2022, Phys. Rev. B **105**, 085411.

Hieulle, J., E. Carbonell-Sanromà, M. Vilas-Varela, A. Garcia-Lekue, E. Guitián, D. Peña, and J. I. Pascual, 2018, Nano Lett. **18**, 418.

Hörmann, L., A. Jeindl, A. T. Egger, M. Scherbela, and O. T. Hofmann, 2019, Comput. Phys. Commun. **244**, 143.

Hötger, D., M. Etzkorn, C. Morchutt, B. Wurster, J. Dreiser, S. Stepanow, D. Grumelli, R. Gutzler, and K. Kern, 2019, Phys. Chem. Chem. Phys. **21**, 2587.

Hövel, H., B. Grimm, and B. Reihl, 2001, Surf. Sci. **477**, 43.

Hu, W., M. A. Kher-Elden, H. Zhang, P. Cheng, L. Chen, I. Piquero-Zulaica, Z. M. Abd El-Fattah, J. V. Barth, K. Wu, and Y.-Q. Zhang, 2022, Nanoscale **14**, 7039.

Huang, B., *et al.*, 2017, Nature (London) **546**, 270.

Huang, H., S. L. Wong, W. Chen, and A. T. S. Wee, 2011, J. Phys. D **44**, 464005.

Huda, M. N., S. Kezilebieke, T. Ojanen, R. Drost, and P. Liljeroth, 2020, npj Quantum Mater. **5**, 17.

Jäck, B., F. Zinser, E. J. König, S. N. P. Wissing, A. B. Schmidt, M. Donath, K. Kern, and C. R. Ast, 2021, Phys. Rev. Res. **3**, 013022.

Jacobse, P. H., R. D. McCurdy, J. Jiang, D. J. Rizzo, G. Veber, P. Butler, R. Zuzak, S. G. Louie, F. R. Fischer, and M. F. Crommie, 2020, J. Am. Chem. Soc. **142**, 13507.

Jensen, H., J. Kröger, R. Berndt, and S. Crampin, 2005, Phys. Rev. B **71**, 155417.

Jiang, W., X. Ni, and F. Liu, 2021, Acc. Chem. Res. **54**, 416.

Jiang, W., S. Zhang, Z. Wang, F. Liu, and T. Low, 2020, Nano Lett. **20**, 1959.
Jolie, W., T.-C. Hung, L. Niggli, B. Verlhac, N. Hauptmann, D. Wegner, and A. A. Khajetoorians, 2022, ACS Nano **16**, 4876.
Jung, M., Y. Yu, and G. Shvets, 2021, Phys. Rev. B **104**, 195437.
Kagan, C. R., E. Lifshitz, E. H. Sargent, and D. V. Talapin, 2016, Science **353**, aac5523.
Kagan, C. R., and C. B. Murray, 2015, Nat. Nanotechnol. **10**, 1013.
Kalff, F. E., M. P. Rebergen, E. Fahrenfort, J. Girovsky, R. Toskovic, J. L. Lado, J. Fernández-Rossier, and A. F. Otte, 2016, Nat. Nanotechnol. **11**, 926.
Kane, C. L., and E. J. Mele, 2005, Phys. Rev. Lett. **95**, 146802.
Kanisawa, K., M. J. Butcher, H. Yamaguchi, and Y. Hirayama, 2001, Phys. Rev. Lett. **86**, 3384.
Kawai, S., A. S. Foster, T. Björkman, S. Nowakowska, J. Björk, F. F. Canova, L. H. Gade, T. A. Jung, and E. Meyer, 2016, Nat. Commun. **7**, 11559.
Kawai, S., M. A. Kher-Elden, A. Sadeghi, Z. M. Abd El-Fattah, K. Sun, S. Izumi, S. Minakata, Y. Takeda, and J. Lobo-Checa, 2021, Nano Lett. **21**, 6456.
Kawai, S., A. Sadeghi, F. Xu, L. Peng, A. Orita, J. Otera, S. Goedecker, and E. Meyer, 2015, ACS Nano **9**, 2574.
Keimer, B., and J. E. Moore, 2017, Nat. Phys. **13**, 1045.
Kempkes, S. N., M. R. Slot, S. E. Freeney, S. J. M. Zevenhuizen, D. Vanmaekelbergh, I. Swart, and C. M. Smith, 2019, Nat. Phys. **15**, 127.
Kempkes, S. N., M. R. Slot, J. J. van den Broeke, P. Capiod, W. A. Benalcazar, D. Vanmaekelbergh, D. Bercioux, I. Swart, and C. Morais Smith, 2019, Nat. Mater. **18**, 1292.
Kepčija, N., T.-J. Huang, F. Klappenberger, and J. V. Barth2015, J. Chem. Phys. **142**, 101931.
Ketterle, W., 2002, Rev. Mod. Phys. **74**, 1131.
Kevan, S. D., and R. H. Gaylord, 1987, Phys. Rev. B **36**, 5809.
Kezilebieke, S., M. N. Huda, V. Vaňo, M. Aapro, S. C. Ganguli, O. J. Silveira, S. Głodzik, A. S. Foster, T. Ojanen, and P. Liljeroth, 2020, Nature (London) **588**, 424.
Khajetoorians, A. A., D. Wegner, A. F. Otte, and I. Swart, 2019, Nat. Rev. Phys. **1**, 703.
Kher-Elden, M., Z. A. El-Fattah, O. Yassin, and M. El-Okr, 2017, Physica (Amsterdam) **524B**, 127.
Kher-Elden, M. A., I. Piquero-Zulaica, K. M. Abd El-Aziz, J. E. Ortega, and Z. M. Abd El-Fattah, 2020, RSC Adv. **10**, 33844.
Klappenberger, F., 2014, Prog. Surf. Sci. **89**, 1.
Klappenberger, F., D. Kühne, W. Krenner, I. Silanes, A. Arnau, F. J. García de Abajo, S. Klyatskaya, M. Ruben, and J. V. Barth, 2009, Nano Lett. **9**, 3509.
Klappenberger, F., D. Kühne, W. Krenner, I. Silanes, A. Arnau, F. J. García de Abajo, S. Klyatskaya, M. Ruben, and J. V. Barth, 2011, Phys. Rev. Lett. **106**, 026802.
Kliewer, J., R. Berndt, and S. Crampin, 2000, Phys. Rev. Lett. **85**, 4936.
Kliewer, J., R. Berndt, and S. Crampin, 2001, New J. Phys. **3**, 22.
Klitzing, K. v., G. Dorda, and M. Pepper, 1980, Phys. Rev. Lett. **45**, 494.
Klyatskaya, S., *et al.*, 2011, Adv. Funct. Mater. **21**, 1230.
Knipp, P. A., and T. L. Reinecke, 1996, Phys. Rev. B **54**, 1880.
Knorr, N., H. Brune, M. Epple, A. Hirstein, M. A. Schneider, and K. Kern, 2002, Phys. Rev. B **65**, 115420.
Kocić, N., D. Blank, P. Abufager, N. Lorente, S. Decurtins, S.-X. Liu, and J. Repp, 2019, Nano Lett. **19**, 2750.
Krenner, W., D. Kühne, F. Klappenberger, and J. V. Barth, 2013, Sci. Rep. **3**, 1454.
Krull, A., P. Hirsch, C. Rother, A. Schiffrin, and C. Krull, 2020, Commun. Phys. **3**, 54.
Kudernac, T., S. Lei, J. A. A. W. Elemans, and S. De Feyter, 2009, Chem. Soc. Rev. **38**, 402.
Kügel, J., M. Leisegang, M. Böhme, A. Krönlein, A. Sixta, and M. Bode, 2017, Nano Lett. **17**, 5106.
Kühne, D., F. Klappenberger, R. Decker, U. Schlickum, H. Brune, S. Klyatskaya, M. Ruben, and J. V. Barth, 2009, J. Am. Chem. Soc. **131**, 3881.
Kühne, D., F. Klappenberger, W. Krenner, S. Klyatskaya, M. Ruben, and J. V. Barth, 2010, Proc. Natl. Acad. Sci. U.S.A. **107**, 21332.
Kühnle, A., 2009, Curr. Opin. Colloid Interface Sci. **14**, 157.
Kulawik, M., H.-P. Rust, M. Heyde, N. Nilius, B. A. Mantooth, P. S. Weiss, and H.-J. Freund, 2005, Surf. Sci. **590**, L253.
Kumagai, T., and A. Tamura, 2008, J. Phys. Soc. Jpn. **77**, 014601.
Kumagai, T., and A. Tamura, 2009, J. Phys. Condens. Matter **21**, 225004.
Kumar, A., K. Banerjee, A. S. Foster, and P. Liljeroth, 2018, Nano Lett. **18**, 5596.
Kumar, A., K. Banerjee, and P. Liljeroth, 2017, Nanotechnology **28**, 082001.
Kumar, D., J. Hellerstedt, B. Field, B. Lowe, Y. Yin, N. V. Medhekar, and A. Schiffrin, 2021, Adv. Funct. Mater. **31**, 2106474.
Lagoute, J., X. Liu, and S. Fölsch, 2005, Phys. Rev. Lett. **95**, 136801.
LaShell, S., B. A. McDougall, and E. Jensen, 1996, Phys. Rev. Lett. **77**, 3419.
Leon, R. C. C., *et al.*, 2020, Nat. Commun. **11**, 797.
Leykam, D., A. Andreanov, and S. Flach, 2018, Adv. Phys. X **3**, 1473052.
Li, H., *et al.*, 2021, Nat. Mater. **20**, 945.
Li, J., W.-D. Schneider, R. Berndt, and S. Crampin, 1998, Phys. Rev. Lett. **80**, 3332.
Li, J., W.-D. Schneider, S. Crampin, and R. Berndt, 1999, Surf. Sci. **422**, 95.
Li, J., *et al.*, 2019, J. Phys. Chem. C **123**, 12730.
Li, Q., R. Cao, and H. Ding, 2020, Appl. Phys. Lett. **117**, 060501.
Li, Q., X. Li, B. Miao, L. Sun, G. Chen, P. Han, and H. Ding, 2020, Nat. Commun. **11**, 1400.
Li, Y., J. Xiao, T. E. Shubina, M. Chen, Z. Shi, M. Schmid, H.-P. Steinrück, J. M. Gottfried, and N. Lin, 2012, J. Am. Chem. Soc. **134**, 6401.
Limot, L., T. Maroutian, P. Johansson, and R. Berndt, 2003, Phys. Rev. Lett. **91**, 196801.
Limot, L., E. Pehlke, J. Kröger, and R. Berndt, 2005, Phys. Rev. Lett. **94**, 036805.
Lin, N., S. Stepanow, M. Ruben, and J. V. Barth, 2008, in *Templates in Chemistry III*, Topics in Current Chemistry Vol. 287, edited by P. Broekmann, K.-H. Dötz, and C. A. Schalley (Springer, Berlin), pp. 1–44, 10.1007/128_2008_150.
Liu, C., I. Matsuda, R. Hobara, and S. Hasegawa, 2006, Phys. Rev. Lett. **96**, 036803.
Lobo-Checa, J., M. Matena, K. Müller, J. H. Dil, F. Meier, L. H. Gade, T. A. Jung, and M. Stöhr, 2009, Science **325**, 300.
Madhavan, V., W. Chen, T. Jamneala, M. F. Crommie, and N. S. Wingreen, 2001, Phys. Rev. B **64**, 165412.
Malterre, D., B. Kierren, Y. Fagot-Revurat, C. Didiot, F. J. García de Abajo, F. Schiller, J. Cordón, and J. E. Ortega, 2011, New J. Phys. **13**, 013026.
Malterre, D., B. Kierren, Y. Fagot-Revurat, S. Pons, A. Tejeda, C. Didiot, H. Cercellier, and A. Bendounan, 2007, New J. Phys. **9**, 391.

Manna, S., P. Wei, Y. Xie, K. T. Law, P. A. Lee, and J. S. Moodera, 2020, Proc. Natl. Acad. Sci. U.S.A. **117**, 8775.
Manoharan, H. C., C. P. Lutz, and D. M. Eigler, 2000, Nature (London) **403**, 512.
Martín-Jiménez, A., J. M. Gallego, R. Miranda, and R. Otero, 2019, Phys. Rev. Lett. **122**, 176801.
Matena, M., J. Björk, M. Wahl, T.-L. Lee, J. Zegenhagen, L. H. Gade, T. A. Jung, M. Persson, and M. Stöhr, 2014, Phys. Rev. B **90**, 125408.
Mitsuoka, S., and A. Tamura, 2011, J. Phys. Condens. Matter **23**, 045008.
Moon, C. R., L. S. Mattos, B. K. Foster, G. Zeltzer, W. Ko, and H. C. Manoharan, 2008, Science **319**, 782.
Moon, C. R., L. S. Mattos, B. K. Foster, G. Zeltzer, and H. C. Manoharan, 2009, Nat. Nanotechnol. **4**, 167.
Moreno, C., *et al.*, 2018, Science **360**, 199.
Morgenstern, K., K.-F. Braun, and K.-H. Rieder, 2002, Phys. Rev. Lett. **89**, 226801.
Mugarza, A., and J. E. Ortega, 2003, J. Phys. Condens. Matter **15**, S3281.
Mugarza, A., F. Schiller, J. Kuntze, J. Cordón, M. Ruiz-Osés, and J. E. Ortega, 2006, J. Phys. Condens. Matter **18**, S27.
Mühlbauer, S., B. Binz, F. Jonietz, C. Pfleiderer, A. Rosch, A. Neubauer, R. Georgii, and P. Böni, 2009, Science **323**, 915.
Mukherjee, A., A. Sanz-Matias, G. Velpula, D. Waghray, O. Ivasenko, N. Bilbao, J. N. Harvey, K. S. Mali, and S. De Feyter, 2019, Chem. Sci. **10**, 3881.
Müller, E. W., 1965, Science **149**, 591.
Müller, K., M. Enache, and M. Stöhr, 2016, J. Phys. Condens. Matter **28**, 153003.
Mutlu, Z., P. H. Jacobse, R. D. McCurdy, J. P. Llinas, Y. Lin, G. C. Veber, F. R. Fischer, M. F. Crommie, and J. Bokor, 2021, Adv. Funct. Mater. **31**, 2103798.
Mutlu, Z., J. P. Llinas, P. H. Jacobse, I. Piskun, R. Blackwell, M. F. Crommie, F. R. Fischer, and J. Bokor, 2021, ACS Nano **15**, 2635.
Nayak, C., S. H. Simon, A. Stern, M. Freedman, and S. Das Sarma, 2008, Rev. Mod. Phys. **80**, 1083.
Negulyaev, N. N., V. S. Stepanyuk, L. Niebergall, P. Bruno, W. Auwärter, Y. Pennec, G. Jahnz, and J. V. Barth, 2009, Phys. Rev. B **79**, 195411.
Negulyaev, N. N., V. S. Stepanyuk, L. Niebergall, P. Bruno, W. Hergert, J. Repp, K.-H. Rieder, and G. Meyer, 2008, Phys. Rev. Lett. **101**, 226601.
Neuhold, G., and K. Horn, 1997, Phys. Rev. Lett. **78**, 1327.
Niebergall, L., G. Rodary, H. F. Ding, D. Sander, V. S. Stepanyuk, P. Bruno, and J. Kirschner, 2006, Phys. Rev. B **74**, 195436.
Niesner, D., and T. Fauster, 2014, J. Phys. Condens. Matter **26**, 393001.
Nowakowska, S., *et al.*, 2015, Nat. Commun. **6**, 6071.
Nowakowska, S., *et al.*, 2016, Small **12**, 3759.
Ohnishi, H., Y. Kondo, and K. Takayanagi, 1998, Nature (London) **395**, 780.
Ohtomo, M., Y. Sekine, H. Hibino, and H. Yamamoto, 2018, Appl. Phys. Lett. **112**, 021602.
Oka, H., O. O. Brovko, M. Corbetta, V. S. Stepanyuk, D. Sander, and J. Kirschner, 2014, Rev. Mod. Phys. **86**, 1127.
Oka, H., P. A. Ignatiev, S. Wedekind, G. Rodary, L. Niebergall, V. S. Stepanyuk, D. Sander, and J. Kirschner, 2010, Science **327**, 843.
Olsson, F. E., M. Persson, A. G. Borisov, J.-P. Gauyacq, J. Lagoute, and S. Fölsch, 2004, Phys. Rev. Lett. **93**, 206803.
Ortega, J. E., M. Corso, Z. M. Abd-el Fattah, E. A. Goiri, and F. Schiller, 2011, Phys. Rev. B **83**, 085411.
Ortega, J. E., J. Lobo-Checa, G. Peschel, S. Schirone, Z. M. Abd El-Fattah, M. Matena, F. Schiller, P. Borghetti, P. Gambardella, and A. Mugarza, 2013, Phys. Rev. B **87**, 115425.
Ortega, J. E., A. Mugarza, F. Schiller, J. Lobo-Checa, and M. Corso, 2020, in *Springer Handbook of Surface Science*, edited by M. Rocca, T. S. Rahman, and L. Vattuone (Springer International Publishing, Cham, Switzerland), pp. 351–385.
Ortega, J. E., G. Vasseur, I. Piquero-Zulaica, S. Matencio, M. A. Valbuena, J. E. Rault, F. Schiller, M. Corso, A. Mugarza, and J. Lobo-Checa, 2018, New J. Phys. **20**, 073010.
Ourmazd, A., 2020, Nat. Rev. Phys. **2**, 342.
Pacchioni, G. E., M. Pivetta, and H. Brune, 2015, J. Phys. Chem. C **119**, 25442.
Palma, C.-A., J. Björk, F. Klappenberger, E. Arras, D. Kühne, S. Stafström, and J. V. Barth, 2015, Nat. Commun. **6**, 6210.
Palma, C.-A., J. Björk, F. Rao, D. Kühne, F. Klappenberger, and J. V. Barth, 2014, Nano Lett. **14**, 4461.
Paniago, R., R. Matzdorf, G. Meister, and A. Goldmann, 1995a, Surf. Sci. **331–333**, 1233.
Paniago, R., R. Matzdorf, G. Meister, and A. Goldmann, 1995b, Surf. Sci. **336**, 113.
Park, C.-H., and S. G. Louie, 2009, Nano Lett. **9**, 1793.
Park, J.-Y., U. D. Ham, S.-J. Kahng, Y. Kuk, K. Miyake, K. Hata, and H. Shigekawa, 2000, Phys. Rev. B **62**, R16341.
Pascual, J. I., *et al.*, 2004, Phys. Rev. Lett. **93**, 196802.
Pawin, G., K. L. Wong, K.-Y. Kwon, and L. Bartels, 2006, Science **313**, 961.
Pekola, J. P., O.-P. Saira, V. F. Maisi, A. Kemppinen, M. Möttönen, Y. A. Pashkin, and D. V. Averin, 2013, Rev. Mod. Phys. **85**, 1421.
Peng, X., *et al.*, 2021, Nat. Commun. **12**, 5895.
Pennec, Y., W. Auwärter, A. Schiffrin, A. Weber-Bargioni, A. Riemann, and J. V. Barth, 2007, Nat. Nanotechnol. **2**, 99.
Pham, V. D., K. Kanisawa, and S. Fölsch, 2019, Phys. Rev. Lett. **123**, 066801.
Pietzsch, O., S. Okatov, A. Kubetzka, M. Bode, S. Heinze, A. Lichtenstein, and R. Wiesendanger, 2006, Phys. Rev. Lett. **96**, 237203.
Piquero-Zulaica, I., A. Garcia-Lekue, L. Colazzo, C. K. Krug, M. S. G. Mohammed, Z. M. Abd El-Fattah, J. M. Gottfried, D. G. de Oteyza, J. E. Ortega, and J. Lobo-Checa, 2018, ACS Nano **12**, 10537.
Piquero-Zulaica, I., S. Nowakowska, J. E. Ortega, M. Stöhr, L. H. Gade, T. A. Jung, and J. Lobo-Checa, 2017, Appl. Surf. Sci. **391**, 39.
Piquero-Zulaica, I., *et al.*, 2017, Nat. Commun. **8**, 787.
Piquero-Zulaica, I., *et al.*, 2019a, New J. Phys. **21**, 053004.
Piquero-Zulaica, I., *et al.*, 2019b, Nanoscale **11**, 23132.
Piquero-Zulaica, I., *et al.*, 2019c, Phys. Rev. Lett. **123**, 266805.
Pivetta, M., G. E. Pacchioni, U. Schlickum, J. V. Barth, and H. Brune, 2013, Phys. Rev. Lett. **110**, 086102.
Polini, M., F. Guinea, M. Lewenstein, H. C. Manoharan, and V. Pellegrini, 2013, Nat. Nanotechnol. **8**, 625.
Potter, A. C., and P. A. Lee, 2012, Phys. Rev. B **85**, 094516.
Rahachou, A. I., and I. V. Zozoulenko, 2004, Phys. Rev. B **70**, 233409.
Ram-Mohan, L. R., 2002, *Finite Element and Boundary Element Applications in Quantum Mechanics*, Oxford Texts in Applied and Engineering Mathematics Vol. 5 (Oxford University Press, Oxford).
Reecht, G., H. Bulou, F. Scheurer, V. Speisser, B. Carrière, F. Mathevet, and G. Schull, 2013, Phys. Rev. Lett. **110**, 056802.
Reinert, F., and S. Hüfner, 2005, New J. Phys. **7**, 97.

Reinert, F., G. Nicolay, S. Schmidt, D. Ehm, and S. Hüfner, 2001, Phys. Rev. B **63**, 115415.
Rejali, R., L. Farinacci, D. Coffey, R. Broekhoven, J. Gobeil, Y. M. Blanter, and S. Otte, 2022, ACS Nano **16**, 11251.
Repp, J., G. Meyer, and K.-H. Rieder, 2004, Phys. Rev. Lett. **92**, 036803.
Repp, J., F. Moresco, G. Meyer, K.-H. Rieder, P. Hyldgaard, and M. Persson, 2000, Phys. Rev. Lett. **85**, 2981.
Rodary, G., D. Sander, H. Liu, H. Zhao, L. Niebergall, V. S. Stepanyuk, P. Bruno, and J. Kirschner, 2007, Phys. Rev. B **75**, 233412.
Rossi, E., and D. K. Morr, 2006, Phys. Rev. Lett. **97**, 236602.
Sato, M., and Y. Ando, 2017, Rep. Prog. Phys. **80**, 076501.
Schiffrin, A., J. Reichert, W. Auwärter, G. Jahnz, Y. Pennec, A. Weber-Bargioni, V. S. Stepanyuk, L. Niebergall, P. Bruno, and J. V. Barth, 2008, Phys. Rev. B **78**, 035424.
Schiffrin, A., A. Riemann, W. Auwärter, Y. Pennec, A. Weber-Bargioni, D. Cvetko, A. Cossaro, A. Morgante, and J. V. Barth, 2007, Proc. Natl. Acad. Sci. U.S.A. **104**, 5279.
Schlickum, U., *et al.*, 2007, Nano Lett. **7**, 3813.
Schlickum, U., *et al.*, 2008, J. Am. Chem. Soc. **130**, 11778.
Schouteden, K., and C. Van Haesendonck, 2012, Phys. Rev. Lett. **108**, 076806.
Seo, J., P. Roushan, H. Beidenkopf, Y. S. Hor, R. J. Cava, and A. Yazdani, 2010, Nature (London) **466**, 343.
Sessi, P., T. Bathon, K. A. Kokh, O. E. Tereshchenko, and M. Bode, 2014, Nano Lett. **14**, 5092.
Sessi, P., *et al.*, 2016, Science **354**, 1269.
Seufert, K., W. Auwärter, F. J. García de Abajo, D. Ecija, S. Vijayaraghavan, S. Joshi, and J. V. Barth, 2013, Nano Lett. **13**, 6130.
Seyller, T., M. Caragiu, R. Diehl, P. Kaukasoina, and M. Lindroos, 1998, Chem. Phys. Lett. **291**, 567.
Shang, J., Y. Wang, M. Chen, J. Dai, X. Zhou, J. Kuttner, G. Hilt, X. Shao, J. M. Gottfried, and K. Wu, 2015, Nat. Chem. **7**, 389.
Shchyrba, A., S. C. Martens, C. Wäckerlin, M. Matena, T. Ivas, H. Wadepohl, M. Stöhr, T. A. Jung, and L. H. Gade, 2014, Chem. Commun. (Cambridge, England) **50**, 7628.
Shchyrba, A., *et al.*, 2014, J. Am. Chem. Soc. **136**, 9355.
Shechtman, D., I. Blech, D. Gratias, and J. W. Cahn, 1984, Phys. Rev. Lett. **53**, 1951.
Shiraki, S., H. Fujisawa, M. Nantoh, and M. Kawai, 2004, Phys. Rev. Lett. **92**, 096102.
Shockley, W., 1939, Phys. Rev. **56**, 317.
Silly, F., M. Pivetta, M. Ternes, F. Patthey, J. P. Pelz, and W.-D. Schneider, 2004, Phys. Rev. Lett. **92**, 016101.
Singha, A., *et al.*, 2011, Science **332**, 1176.
Slot, M. R., T. S. Gardenier, P. H. Jacobse, G. C. P. van Miert, S. N. Kempkes, S. J. M. Zevenhuizen, C. M. Smith, D. Vanmaekelbergh, and I. Swart, 2017, Nat. Phys. **13**, 672.
Slot, M. R., S. N. Kempkes, E. J. Knol, W. M. J. van Weerdenburg, J. J. van den Broeke, D. Wegner, D. Vanmaekelbergh, A. A. Khajetoorians, C. Morais Smith, and I. Swart, 2019, Phys. Rev. X **9**, 011009.
Sobota, J. A., Y. He, and Z.-X. Shen, 2021, Rev. Mod. Phys. **93**, 025006.
Sprunger, P. T., L. Petersen, E. W. Plummer, E. Lægsgaard, and F. Besenbacher, 1997, Science **275**, 1764.
Stadtmüller, B., *et al.*, 2014, Nat. Commun. **5**, 3685.
Stepanow, S., M. Lingenfelder, A. Dmitriev, H. Spillmann, E. Delvigne, N. Lin, X. Deng, C. Cai, J. V. Barth, and K. Kern, 2004, Nat. Mater. **3**, 229.
Stepanyuk, V. S., L. Niebergall, W. Hergert, and P. Bruno, 2005, Phys. Rev. Lett. **94**, 187201.
Stilp, F., A. Bereczuk, J. Berwanger, N. Mundigl, K. Richter, and F. J. Giessibl, 2021, Science **372**, 1196.
Stöhr, M., M. Wahl, H. Spillmann, L. Gade, and T. Jung, 2007, Small **3**, 1336.
Stroscio, J. A., and D. M. Eigler, 1991, Science **254**, 1319.
Sun, H., S. Tan, M. Feng, J. Zhao, and H. Petek, 2018, J. Phys. Chem. C **122**, 18659.
Sun, K., and S. Kawai, 2021, Phys. Chem. Chem. Phys. **23**, 5455.
Taber, B. N., C. F. Gervasi, J. M. Mills, D. A. Kislitsyn, E. R. Darzi, W. G. Crowley, R. Jasti, and G. V. Nazin, 2016, J. Phys. Chem. Lett. **7**, 3073.
Tamai, A., W. Meevasana, P. D. C. King, C. W. Nicholson, A. de la Torre, E. Rozbicki, and F. Baumberger, 2013, Phys. Rev. B **87**, 075113.
Tarucha, S., D. G. Austing, T. Honda, R. J. van der Hage, and L. P. Kouwenhoven, 1996, Phys. Rev. Lett. **77**, 3613.
Tatsumi, Y., S. Mitsuoka, and A. Tamura, 2018, Surf. Rev. Lett. **25**, 1850091.
Telychko, M., *et al.*, 2021, Sci. Adv. **7**, eabf0269.
Ternes, M., M. Pivetta, F. Patthey, and W.-D. Schneider, 2010, Prog. Surf. Sci. **85**, 1.
Ternes, M., C. Weber, M. Pivetta, F. Patthey, J. P. Pelz, T. Giamarchi, F. Mila, and W.-D. Schneider, 2004, Phys. Rev. Lett. **93**, 146805.
Tersoff, J., and D. R. Hamann, 1985, Phys. Rev. B **31**, 805.
Teyssandier, J., S. D. Feyter, and K. S. Mali, 2016, Chem. Commun. (Cambridge, England) **52**, 11465.
Theobald, J. A., N. S. Oxtoby, M. A. Phillips, N. R. Champness, and P. H. Beton, 2003, Nature (London) **424**, 1029.
Tokura, Y., M. Kawasaki, and N. Nagaosa, 2017, Nat. Phys. **13**, 1056.
Trainer, D. J., S. Srinivasan, B. L. Fisher, Y. Zhang, C. R. Pfeiffer, S.-W. Hla, P. Darancet, and N. P. Guisinger, 2022, ACS Nano **16**, 16085.
Udhardt, C., *et al.*, 2017, J. Phys. Chem. C **121**, 12285.
Umbach, T. R., M. Bernien, C. F. Hermanns, A. Krüger, V. Sessi, I. Fernandez-Torrente, P. Stoll, J. I. Pascual, K. J. Franke, and W. Kuch, 2012, Phys. Rev. Lett. **109**, 267207.
Urgel, J. I., D. Écija, G. Lyu, R. Zhang, C.-A. Palma, W. Auwärter, N. Lin, and J. V. Barth, 2016, Nat. Chem. **8**, 657.
Urgel, J. I., M. Schwarz, M. Garnica, D. Stassen, D. Bonifazi, D. Ecija, J. V. Barth, and W. Auwärter, 2015, J. Am. Chem. Soc. **137**, 2420.
Urgel, J. I., S. Vijayaraghavan, D. Ecija, W. Auwärter, and J. Barth, 2016, Surf. Sci. **643**, 87.
van der Wiel, W. G., S. De Franceschi, J. M. Elzerman, T. Fujisawa, S. Tarucha, and L. P. Kouwenhoven, 2002, Rev. Mod. Phys. **75**, 1.
van Miert, G., and C. Ortix, 2020, npj Quantum Mater. **5**, 63.
van Wees, B. J., H. van Houten, C. W. J. Beenakker, J. G. Williamson, L. P. Kouwenhoven, D. van der Marel, and C. T. Foxon, 1988, Phys. Rev. Lett. **60**, 848.
Walkup, D., F. Ghahari, C. Gutiérrez, K. Watanabe, T. Taniguchi, N. B. Zhitenev, and J. A. Stroscio, 2020, Phys. Rev. B **101**, 035428.
Wang, H., X. Zhang, Z. Jiang, Y. Wang, and S. Hou, 2018, Phys. Rev. B **97**, 115451.
Wang, S., L. Z. Tan, W. Wang, S. G. Louie, and N. Lin, 2014, Phys. Rev. Lett. **113**, 196803.

Wang, S., W. Wang, L. Z. Tan, X. G. Li, Z. Shi, G. Kuang, P. N. Liu, S. G. Louie, and N. Lin, 2013, Phys. Rev. B **88**, 245430.
Wang, Y., X. Ge, C. Manzano, J. Kröger, R. Berndt, W. A. Hofer, H. Tang, and J. Cerda, 2009, J. Am. Chem. Soc. **131**, 10400.
Wang, Y., N. Xue, R. Li, T. Wu, N. Li, S. Hou, and Y. Wang, 2019, ChemPhysChem **20**, 2262.
Wang, Z. F., Z. Liu, and F. Liu, 2013, Nat. Commun. **4**, 1471.
Weckesser, J., A. De Vita, J. V. Barth, C. Cai, and K. Kern, 2001, Phys. Rev. Lett. **87**, 096101.
Wei, P., S. Manna, M. Eich, P. Lee, and J. Moodera, 2019, Phys. Rev. Lett. **122**, 247002.
Wharam, D. A., T. J. Thornton, R. Newbury, M. Pepper, H. Ahmed, J. E. F. Frost, D. G. Hasko, D. C. Peacock, D. A. Ritchie, and G. A. C. Jones, 1988, J. Phys. C **21**, L209.
Wintjes, N., J. Lobo-Checa, J. Hornung, T. Samuely, F. Diederich, and T. A. Jung, 2010, J. Am. Chem. Soc. **132**, 7306.
Wyrick, J., *et al.*, 2011, Nano Lett. **11**, 2944.
Xing, L., Z. Peng, W. Li, and K. Wu, 2019, Acc. Chem. Res. **52**, 1048.
Yan, B., B. Stadtmüller, N. Haag, S. Jakobs, J. Seidel, D. Jungkenn, S. Mathias, M. Cinchetti, M. Aeschlimann, and C. Felser, 2015, Nat. Commun. **6**, 10167.
Yan, L., M. Hua, Q. Zhang, T. U. Ngai, Z. Guo, T. C. Wu, T. Wang, and N. Lin, 2019, New J. Phys. **21**, 083005.
Yan, L., G. Kuang, Q. Zhang, X. Shang, P. N. Liu, and N. Lin, 2017, Faraday Discuss. **204**, 111.
Yan, L., and P. Liljeroth, 2019, Adv. Phys. X **4**, 1651672.
Yan, L., O. J. Silveira, B. Alldritt, S. Kezilebieke, A. S. Foster, and P. Liljeroth, 2021, ACS Nano **15**, 17813.
Yin, J.-X., S. H. Pan, and M. Zahid Hasan, 2021, Nat. Rev. Phys. **3**, 249.
Yoffe, A. D., 2001, Adv. Phys. **50**, 1.
Yokoyama, T., S. Yokoyama, T. Kamikado, Y. Okuno, and S. Mashiko, 2001, Nature (London) **413**, 619.
Yu, M., *et al.*, 2020, Nat. Chem. **12**, 1035.
Yue, S., *et al.*, 2020, Phys. Rev. B **102**, 201401.
Zapf, V., M. Jaime, and C. D. Batista, 2014, Rev. Mod. Phys. **86**, 563.
Zhang, C., Y. Li, D. Pei, Z. Liu, and Y. Chen, 2020, Annu. Rev. Mater. Res. **50**, 131.
Zhang, L. Z., Z. F. Wang, B. Huang, B. Cui, Z. Wang, S. X. Du, H.-J. Gao, and F. Liu, 2016, Nano Lett. **16**, 2072.
Zhang, R., G. Lyu, C. Chen, T. Lin, J. Liu, P. N. Liu, and N. Lin, 2015, ACS Nano **9**, 8547.
Zhang, R., *et al.*, 2020, Angew. Chem., Int. Ed. **59**, 2669.
Zhang, T., *et al.*, 2009, Phys. Rev. Lett. **103**, 266803.
Zhang, X., and M. Zhao, 2015, Sci. Rep. **5**, 14098.
Zhang, X., Y. Zhou, B. Cui, M. Zhao, and F. Liu, 2017, Nano Lett. **17**, 6166.
Zhang, Y.-Q., J. Björk, J. V. Barth, and F. Klappenberger, 2016, Nano Lett. **16**, 4274.
Zhang, Y.-Q., *et al.*, 2018, Nat. Chem. **10**, 296.
Zhou, C.-S., X.-R. Liu, Y. Feng, X. Shao, M. Zeng, K. Wang, M. Feng, and C. Liu, 2020, Appl. Phys. Lett. **117**, 191601.
Zwanenburg, F. A., A. S. Dzurak, A. Morello, M. Y. Simmons, L. C. L. Hollenberg, G. Klimeck, S. Rogge, S. N. Coppersmith, and M. A. Eriksson, 2013, Rev. Mod. Phys. **85**, 961.